



GEOFORSCHUNGSZENTRUM POTSDAM
STIFTUNG DES ÖFFENTLICHEN RECHTS

Scientific Technical Report

ISSN 1610-0956

Core Surface Flow Models from Decadal and Subdecadal Secular Variation of the Main Geomagnetic Field

**Dissertation
zur Erlangung des Doktorgrades
des Fachbereiches Geowissenschaften
der Freien Universität Berlin
2004**

vorgelegt von

Ingo Wardinski

Gutachter

1 2

Prof. Dr. Volker Haak

Institut für Geophysik

Freie Universität Berlin

Dr. Richard Holme

Dept of Earth and Ocean Sciences

University of Liverpool, UK

eingereicht im Winter 2004
Disputation am 4. Februar 2005

Summary

The main objective of this thesis is an investigation and description of the secular variation of the Earth's magnetic field between 1980 and 2000. In particular, in the first part of this study the phenomenon of geomagnetic jerks are investigated by means of a deterministic model, which basically gives a description of the secular variation as a parameterization of typical periodicities of the external field. I argue that the conclusion drawn from this approach is not valid for explaining jerks as caused by external events and not valid to describe the global secular variation.

In the second part a time-dependent model of the secular variation between 1980 and 2000 is developed. The endpoints of the time interval were chosen, because of the availability of high quality field models from satellite data for these epochs. The Gauss coefficients are expanded in time as function of cubic B-splines. This model is forced to fit field models from high quality vector measurements from MAGSAT in 1980 and ØRSTED in 2000. The methodology is new.

The model is a valuable extension of the hitherto existing time-dependent description of the secular variation, the *GUFM* which was valid until 1990. Unlike *GUFM* the model is based on observatory monthly means, and the knot spacing of the cubic B-Splines tighter than *GUFM*. Therefore it reveals a short term secular variation on subdecadal time scale, which was not as yet resolved. The model is also valuable to test the frozen flux hypothesis and to link some of the morphology of the radial field at the core-mantle boundary to the geodynamo.

The third part of this thesis deals with the inversion of the time-dependent field and secular variation model for different kinds of core surface flow. These flows allow prediction of the decadal change of the length of the day, an observable which is independent to geomagnetic data. The prediction of some of the flows have the right tendency, but differ in slope from the observed change of the length of the day.

Zusammenfassung

In dieser Studie ist ein besonderes Augenmerk auf die Beschreibung des Erdmagnetfeldes und seiner Säkularvariation im Zeitraum von 1980 und 2000 gelegt worden. Dabei wurden die beiden Endpunkte des Zeitintervalls so gewählt, dass sie mit den Satellitenmissionen MAGSAT 1980 und CHAMP, ØRSTED in 2000 zusammenfallen. Diese Satellitenmissionen erlaubten es, räumlich hochaufgelöste Modelle des Erdmagnetfeldes zu erstellen.

Im ersten Teil dieser Studie befasse ich mich mit der Säkularvariation, beobachtet über 70 Jahre an drei verschiedenen Stationen: Eskdalemuir (Schottland), Hermanus (Südafrika) und Kakioka (Japan). Hier versuche ich die Säkularvariation mittels eines einfachen deterministischen Modells zu beschreiben, d. h. eine Beschreibung der Säkularvariation als (gewichtete) Überlagerung von Periodizitäten hervorgerufen durch Prozesse ausserhalb der Erdatmosphäre, z. B. 11-Jahres-Zyklus der Sonne, Sonnenrotation, etc. Dabei vermag dieser einfache Ansatz die Säkularvariation der einzelnen Stationen wiederzugeben, aber jedes Modell ist eben nur für eine bestimmte Station gültig, also ist somit die Aussagekraft dieser Modelle lokal beschränkt. Mehr noch; die Schlussfolgerung, dass die Säkularvariation und insbesondere, dass Geomagnetische Jerks durch externe Prozesse verursacht werden, ist nicht zutreffend.

Im zweiten Teil meiner Arbeit entwerfe ich ein Modell der Säkularvariation zwischen 1980 und 2000 basierend auf zeitlich variablen Gauss-Koeffizienten. Hier werden die bereits angesprochenen Hauptfeldmodelle der Satellitenmissionen verwendet, um das Modell der Säkularvariation in den Endpunkten festzulegen.

Anhand dieses Modells ist es mir möglich Eigenschaften, wie z. B. räumliche Ausbreitung, der drei bekannten Geomagnetischen Jerks dieses Zeitraumes (1983, 1991 und 1999) zu untersuchen. Weiterhin ermöglicht das Modell den Nachweis von magnetischer Diffusion an der Kern-Mantel-Grenze und stellt eine Weiterentwicklung des Modells für den Zeitraum 1590 – 1990 von Jackson et al. (2000) dar.

Last but not least, erlaubt das Modell Rückschlüsse auf die räumliche Konfiguration des Geodynamos; es weist auf die Existenz von Konvektionsrollen hin.

Im dritten Teil meiner Arbeit entwickle ich mögliche Modelle für die Fluidbewegung an der Kern-Mantel-Grenze zwischen 1980 – 2000 unter Verwendung meines Modells für das Hauptfeld und seiner Säkularvariation. Die allgemeine Vorstellung ist, dass die Säkular-

variation an der Kern–Mantel–Grenze durch Advektion und Diffusion erzeugt wird. Das wird genau durch die Induktionsgleichung beschrieben. Wichtig hierbei ist die Rolle der Diffusion, ich gehe darauf in den abschließenden Bemerkungen ein.

Aber die Fluidbewegung beschreibt nicht nur die Säkularvariation sondern auch eine davon unabhängige Observable, nämlich die Variation der Tageslänge.

Acknowledgements

For the last four years I spent to research for and prepare this thesis I have been greatly assisted by many. First I would like to thank Professor Volker Haak, who motivated me and has shown consistent interest in this project.

A special thank you to Richard Holme, not only initiating this work and introducing me to this interesting area of research, also for his constructive criticism and permanent inspiration.

Susan Macmillan, who kindly provided the data and shed light on the mysteries of them. I would also like to thank Monika Korte, Mioara Manda, Aude Chambodut, Judith Schwarte, Ludwig Ballani, Hans Greiner-Mai and Martin Rother. In particular, many thanks to Chris Finlay for many discussions on any topic and for being a good companion during my stay in Paris.

Finally, but not less importantly, thanx to Mum and Kerstin who kept me going.

This study was funded by the DFG-Schwerpunktprojekt 1097.

Table of Contents

Summary	i
Zusammenfassung	iii
Acknowledgements	v
Table of Contents	vii
List of Figures	ix
List of Tables	xiii
List of Abbreviations	xv
1 Earth's magnetic field	1
1.1 Observation of the geomagnetic field	1
1.2 Origin and temporal variation	2
1.3 Outline of this thesis	6
2 A deterministic model of the temporal variation of the geomagnetic field	9
2.1 Analysis of the external field variation	10
2.1.1 The multi-taper method	12
2.1.2 Statistical confidence	12
2.1.3 Results	12
2.2 Modelling of disturbance fields	14
2.2.1 Method	14
2.2.2 Results and Discussion	18
2.3 Arguments against the external field variations cause of jerks	19
2.4 Conclusions	27
3 Time-dependent modelling of the geomagnetic field	29
3.1 Data	29
3.1.1 Geomagnetic observatory data	30
3.1.2 Repeat station data	30

3.2	Data processing	33
3.2.1	Secular variation estimates	34
3.3	Some fundamental concepts of Inverse Problems	34
3.3.1	Statement of the forward problem and inverse problem	34
3.4	Method	36
3.4.1	The least-squares estimator	36
3.4.2	Regularization of ill-posed inverse problem	37
3.4.3	Application to geomagnetic data	39
3.4.4	Extension of the Bloxham-Jackson formalism	43
3.4.5	Modelling and selection of damping parameter	45
3.5	Results	48
3.5.1	Morphology of the magnetic field at the core-mantle boundary	48
3.5.2	The secular variation and geomagnetic jerks during this period	53
3.5.3	Analysis of the residuals	58
3.5.4	Covariance and Resolution Analysis	60
3.5.5	Conclusion	61
4	Qualitative analysis of the core-surface fluid motions	63
4.1	Inversion for core-surface flows	63
4.1.1	Scheme of the flow computation	65
4.1.2	Steady motion theorem	66
4.1.3	Steady flow in a azimuthally drifting reference frame	66
4.1.4	Geostrophic flow	68
4.1.5	Torsional oscillation	71
4.2	Maps of core-surface flows	75
4.2.1	Steady flows	75
4.2.2	Steady flows in an azimuthally drifting reference frame	77
4.2.3	Tangetially geostrophic flows and torsional oscillation	80
4.2.4	Prediction of secular variation from flows	88
4.2.5	Prediction of the decadal change of length of day	91
4.3	Discussion and Conclusion	92
5	Conclusion and Prospects	95
	Bibliography	97
A	List of the used observatories and repeat stations	107
B	List of base line jumps	123
C	Flow Coefficients of the drifting flow	127

List of Figures

1.1	Global chart of the Declination (D) derived from <i>GUFM</i> [Jackson et al., 2000] for 5 epochs 1590, 1690, 1790, 1890 and 1990 from top to bottom. The red line is the zero Declination line (agonic line). Units are degrees.	3
1.1	Concluded.	4
1.2	Westward drift for different latitudes during the period 1980 – 2000. After [Langel, 1987, p. 445, method 2].	5
2.1	The secular variation of the east magnetic component (dY/dt) for Eskdalemuir (Scotland) from 1932 to 2002 (red dots). The black solid line is a moving average of the red dots. The geomagnetic jerks, around 1969 and 1991 are both present in the series. The jerk around 1999 is less clear.	10
2.2	Smoothed and monthly averaged sun spot numbers, from 1932 to 2002.	11
2.3	Spectral power density of the daily sun spot numbers from 1932 – 2001. The black curve is the smoothed spectrum, and the red line indicate the 90% significance level.	14
2.4	Spectral power density of the daily means of the EUV-Index from 1947 – 2001. The black curve is the smoothed spectrum, and the red line indicate the 90% significance level.	15
2.5	Spectral power density of the daily means of the Ap-Index from 1932 – 2001. The black curve is the smoothed spectrum, and the red line indicate the 90% significance level.	16
2.6	Spectral power density of the daily means of the D_{ST} -Index from 1957 – 2001. The black curve is the smoothed spectrum, and the red line indicate the 90% significance level.	17
2.7	The left figures are the direct comparison of the prediction of deterministic model (red curve) valid for the period 1932 – 2001 and secular variation estimates for the X, Y and Z component in Eskdalemuir (from top to bottom, black curves). All curves are smoothed by a moving average of 20 days. The right column pictures are the remaining signal, the residuals, which cannot be explained by the deterministic model (red curve). The black curve represents the smoothed residuals.	20
2.8	The fit to the secular variation estimates for the X, Y and Z component in Kakioka. Curves are assembled and smoothed in same way as in Fig.(2.7).	21

2.9	Shown here the fit for the secular variation estimates for the X, Y and Z component in Hermanus for the period 1941 – 2001. Curves are assembled and smoothed in same way as in Fig.(2.7).	22
2.10	Spectra of the principal components coefficients for X, Y and Z of the analysis of the three sites Eskdalemuir (ESK), Kakioka (KAK) and Hermanus (HER).	23
2.11	The left figures are the direct comparison of the prediction of deterministic model considering only short periods (red curve) valid for the period 1932 – 2001 and secular variation estimates for the X, Y and Z component in Eskdalemuir (from top to bottom, black curves). All curves are smoothed by a moving average of 20 days. The right column pictures are the remaining signal, the residuals, which cannot be explained by the short periods of the deterministic model (red curve). The black curve represents the smoothed residuals.	24
2.12	Shown here the fit for the secular variation estimates for the X, Y and Z component in Kakioka for short periods only. Curves are assembled and smoothed in same way as in Fig.(2.11).	25
2.13	Shown here the fit for the secular variation estimates for the X, Y and Z component in Hermanus for short periods only. Curves are assembled and smoothed in same way as in Fig.(2.11).	26
3.1	Global chart of permanent observatories, red circles shows places for which monthly means are available, black dots for sites where only annual means are available.	31
3.2	Global chart of repeat station, green triangles sites provided one secular variation estimate (SVE), red dots indicate sites of multiple visits, but less than 5 SVE, blue dots indicating sites with more than 4 SVE.	33
3.3	The number of available annual secular variation estimates shown as red crosses and the number of monthly secular variation estimates (either based on observatory or repeat station measurements) shown as solid black curve.	35
3.4	Trade-off curves of the temporal norm vs. misfit for different spatial damping weak: $\lambda_{\Gamma} = 4.0 \cdot 10^1$, medium: $\lambda_{\Gamma} = 4.0 \cdot 10^3$ and strong: $\lambda_{\Gamma} = 4.0 \cdot 10^6$	46
3.5	Spectra of main field of a time-dependent model for three different times 1980, 1991 and 2000 in comparison with the satellite main field models from MAGSAT and ØRSTED. The departure damping is chosen to be weak ($\lambda_{\Gamma} = 6.0 \cdot 10^{-1}$).	47
3.6	Spectra of main field of the preferred time-dependent model for three different times (1980, 1990 and 2000), where the departure damping is chosen to be strong ($\lambda_{\Gamma} = 6.0 \cdot 10^6$) in comparison with the satellite main field models from MAGSAT and ØRSTED.	47
3.7	Radial component of the geomagnetic field at 1980, 1985, 1990, 1995 and 2000 from top to bottom (Mollweide equal-area projection).	51

3.8	Radial component of the geomagnetic field, with key features of the field: reverse flux patches are labeled R1 – R8, normal flux patches as N1 – N10 (Mollweide equal–area projection).	52
3.9	The mean change of the unsigned flux integral for 1980 – 2000.	52
3.10	Comparison of modeled secular variation (black line) with the secular variation estimates at selected permanent observatories (red line). From left to right: dX/dt , dY/dt , dZ/dt . From top to bottom: Resolute Bay (Canada), Niemegek (Germany), Newport (USA), MBour (Senegal), Pamatai (French Polynesian).	55
3.10	(<i>continued from previous page</i>) From top to bottom: Hermanus (South Africa), Eyrwell (New Zealand) and Scott Base (Antarctica).	56
3.11	Radial component of the secular variation at 1980, 1985, 1990, 1995 and 2000 from top to bottom (Mollweide equal–area projection).	57
3.12	In the left column, Residuals between model and the secular variation estimates for Resolute Bay, Niemegek, Pamatai, Hermanus and Scott Base (from top to bottom). Residuals for X in green, Y in blue and Z in red. Auto-correlation function is shown with the same color scheme as for the residuals (middle column). Cross-correlation functions are presented, where the pink line is the cross-correlation function of X and Y, blue for X and Z and red for Y and Z. The horizontal black lines represent the 95 % significance level.	59
3.13	Resolution estimates of the Gauss coefficients at different times. Gauss coefficients are ordered with increasing l and m , i. e. $g_1^0, g_1^1, h_1^1, \dots, h_{15}^{15}$. The resolution of the coefficients with an order greater than 12 are nearly zero this indicates a nearly complete control of these coefficients by the a priori beliefs.	61
3.14	Covariance estimates of the Gauss coefficients at six different times. Gauss coefficients are ordered with increasing degree l and order m , i. e. $g_1^0, g_1^1, h_1^1, \dots, h_{15}^{15}$.	62
4.1	Sketch of the geostrophic degeneracy, the white region are the areas where the geostrophic assumption is expected to fail. ζ is chosen to be $10^{-3}T$. . .	71
4.2	Sketch of the core geometry to illustrate the Taylor constraint	73
4.3	Figure shows the excitation mechanism of Alfvén like waves, such as torsional oscillation. Courtesy of C. Finlay	74
4.4	Steady flows centered on 1985, 1990 and 1995. The vectors show the velocity and direction of the fluid motion at the CMB.	76
4.5	Objective function as a function of drift rate for different damping parameters λ_v	77
4.6	The three top maps show the drifting flows for 1980, 1990, and 2000 in the mantle frame. The bottom map shows the steady flow in the drifting reference frame.	79
4.7	Trade off curves for three different temporal damping: strong $\lambda_t = 0.1E+03$, medium $\lambda_t = 0.1E-01$ and weak $\lambda_t = 0.1E-09$	80

4.8	Tangentially geostrophic flows for 1980, 1990 and 2000. The vectors show the velocity and direction of the fluid motion at the CMB. The color scale shows the intensity of the horizontal divergence (upwelling and downwelling) of the flow.	83
4.9	Sketch of the toroidal flux expulsion in an electrically conducting medium.	84
4.10	The ageostrophic force balance, where F is the frictional drag.	84
4.11	The ageostrophic part of the flow 2.	84
4.12	Torsional oscillation flows (flow 3) for 1980, 1990, and 2000. The vectors show the velocity and direction of the fluid motion at the CMB.	85
4.13	The resolution of the toroidal (left) and poloidal velocity coefficients (right) for flow 1.	86
4.14	The resolution of the toroidal (left) and poloidal velocity coefficients (right) for flow 2.	87
4.15	Comparison of modeled secular variation (solid black line) to the secular variation estimates at selected permanent observatories. Red curves are the prediction of flow 1, of flow 3 (green curves) and of the purely toroidal flow (blue curves). The pink curves are the prediction by the drifting flow (E1). From left to right: dX/dt , dY/dt , dZ/dt . From top to bottom: Resolute Bay (Canada), Niemegk (Germany), Newport (USA), MBour (Senegal), Pamatai (French Polynesian).	89
4.15	<i>(continued from previous page)</i> From top to bottom: Hermanus (South Africa), Eyrwell (New Zealand) and Scott Base (Antarctica).	90
4.16	Comparison of Λ prediction. The black represent the Λ taken from Holme & de Viron [2005]. The colored curves are the predictions from the flows accordingly to the legend in the lower left corner.	93
4.17	The zonal velocity profile for the epochs 1980, 1990, and 2000, derived from flow 1 (top) and flow 2 (bottom).	94
5.1	Mauersberger–Lowes spectra of the secular variation at the CMB of the <i>GUFM</i> (dashed lines) and of the P-UFM1 (solid lines).	95
C.1	Comparison of coefficients of the different drifting solutions. The black curves are the time–dependent model of the secular variation P-UFM1, pink line is the prediction of the westward solution W1, the green line the eastward solution E1 and the blue line the westward solution W2.	128

List of Tables

1	List of Abbreviations and parameters used in this Thesis	xv
2.1	Periods of solar and geomagnetic activity.	13
2.2	The rms misfit for three different observatories and three deterministic models.	19
3.1	Error estimates of the magnetic field component X, Y and Z and for their computed secular variations \dot{X}, \dot{Y} and \dot{Z} for European repeat surveys . . .	31
3.2	Smoothing norms for magnetic field inversion after Holme & Bloxham [1996].	44
3.3	Statistics and parameters of the time-dependent modelling	46
3.4	Listing of individual reverse flux patches for the epochs 1980 and 2000 . . .	49
4.1	Diagnostics of the drifting flow.	78
4.2	Parameters and diagnostics of the inversions for two tangentially geostrophic flow and the flow invoking torsional oscillation.	81
4.3	Characteristics of the two tangentially geostrophic flows and the flow invoking torsional oscillation. The total energy is given in arbitrary units and the components as percentage of the total flow (1) and the total symmetric component (2) and total asymmetric component (3), respectively.	82
A.1	Magnetic observatories and repeat stations	107
B.1	List of base line jumps, site changes and new instrumentation at permanent observatories during 1980 – 2000. The observatories are ordered by descending latitude, from north to south.	123

Table 1: List of Abbreviations and parameters used in this Thesis

EUV index	Extreme Ultra Violet index
D_{ST} -index	Daily storm index
SSN	Sun spot numbers
SVE	Secular variation estimates
GUFM	There is no official transcription given by authors of Jackson et al. [2000], but the geomagnetic community tend to believe that this abbreviations stands for <i>Grand Unified Field Model</i> .
a	Earth's radius 6371.2 km
c	Earth's core radius 3485.0 km
Λ	Decadal change of the length of day
λ_s	Spatial regularization or damping parameter
λ_t	Temporal regularization or damping parameter
λ_1, λ_2	Regularization or damping parameter of the a priori information
λ_v	Regularization or damping parameter of the flow velocity
$\oint(\cdot)dS$	Integration over a sphere
$\int(\cdot)d\Sigma$	Integration over a cylinder

Chapter 1

Earth's magnetic field

*It is well to observe the force and virtue and
consequence of discoveries, and these are to be seen
nowhere more conspicuously than in printing,
gunpowder, and the magnet.*

Francis Bacon

1.1 Observation of the geomagnetic field

The history of the probing of the Earth's magnetic field is tightly linked to the exploration of the oceans and the discovery of islands and continents. The magnetic field has been known for about 4000 years, having first been noted in China. Although the use of the magnetic field for navigation cannot be unequivocally identified until 1088 in China and nearly 100 years later in Europe [Backus et al., 1996], it was already known by the seamen in medieval times that an iron needle always aligns in one direction, giving the north course. It was also common knowledge that garlic weakened magnets, and even in the 1600's sailors avoided garlic and onions on board ship. This superstition might find its origin in a false transcription of "alio" (other) to "allio" (garlic) of an essay by Pliny (A.D. 23-79) discussing the action of magnets.

The growing interest in compass navigation may have influenced Gilbert somewhat because he wrote *De Magnete* [Gilbert, 1600] at the time the English were preparing to meet the Spanish Armada. *De Magnete* was the first comprehensive study of magnetism. Gilbert dedicated it to those who look for knowledge "not only in books but in things themselves". Since this initial work the Earth's magnetic field has been observed systematically for almost 450 years. Gauss led the effort to set up a global system of magnetic observatories, some of which have been running up to the present day. Geophysical exploration using measurements of the earth's magnetic field was employed earlier than any other geophysical technique. Even to this day, the magnetic methods are one of the most commonly used geophysical tools. This stems from the fact that magnetic observations are obtained relatively easily and cheaply and few corrections must be applied to the observations.

The early navigators observed that the compass does not point to the geographic north

given by celestial investigation. This discrepancy is referred as declination. Also the fact, that the true direction of the magnetic field is not horizontal, the magnetic inclination as it is called, was known to the navigators in the 16th century.

To introduce the geomagnetic elements that describe the magnetic field vector at a certain point on the Earth's surface, we may consider a local Cartesian coordinate system with x pointing to the geographic north, y to the east and z vertically downward. The magnetic elements X, Y, Z are the components of the magnetic field vector \mathbf{B} in this frame, then the declination D is obtained by

$$\tan D = Y/X, \quad (1.1)$$

the total force F is

$$F = \sqrt{X^2 + Y^2 + Z^2} \quad (1.2)$$

and the inclination I satisfies

$$\tan I = Z/\sqrt{X^2 + Y^2} = Z/H, \quad (1.3)$$

where H is the horizontal force.

1.2 The Earth's magnetic field, its temporal variation and its origin

Volcanoes are often active for long periods, and by comparing the magnetization of their lava flows from different times one can learn about changes in the direction of the local magnetic field. As Brunhes studied ancient lava flows in France he found that the magnetization appeared to be reversed [Brunhes, 1906]. Other examples were then found, and Matuyama [1929] examined the evidence and suggested that the magnetic signatures were evidence of actual reversals. Matuyama proposed that long periods existed in the past history of Earth in which the polarity of the magnetic poles was the opposite of what it is now.

Even on shorter time scales, the temporal behavior of the Earth's magnetic field shows a rich temporal variability, both periodic and aperiodic. These characteristics are caused by different mechanisms either external to the Earth's surface or internal.

In 1839, Karl Friedrich Gauss published his method for separation of magnetic field into parts due to external and internal sources by spherical harmonic analysis [Gauss, 1839]. Applying this method to measurements of the Earth's magnetic field, he could show that most of the field was of internal origin, thus confirming Gilbert's early work. The internal part of the geomagnetic field is now referred to as main field and its temporal change as secular variation.

The change of field in time was first detected by Gunter in 1624. He and Gellibrand collected measurements of magnetic declination made at Limehouse near London which showed a systematic decrease in magnetic declination between 1580 and 1634. On the

basis of this study Halley produced a model for the variation in terms of dipole moving generally westward, deep within the earth, making a circuit every 700 years [Halley, 1683, 1692]. He explained this property by an Earth composed of magnetized concentric shells separated by a fluid and rotating relative to each other.

The westward drift is a particular feature of the geomagnetic field originating internal to the Earth's surface. However, this phenomenon does not manifest globally. Figures (1.1) illustrate the westward drift of the zero declination line, the Agonic line, at 100-year intervals from 1590 to 1990. The eastern Agonic line moves in this period steadily westward, whereas the western line approaches the Americas.

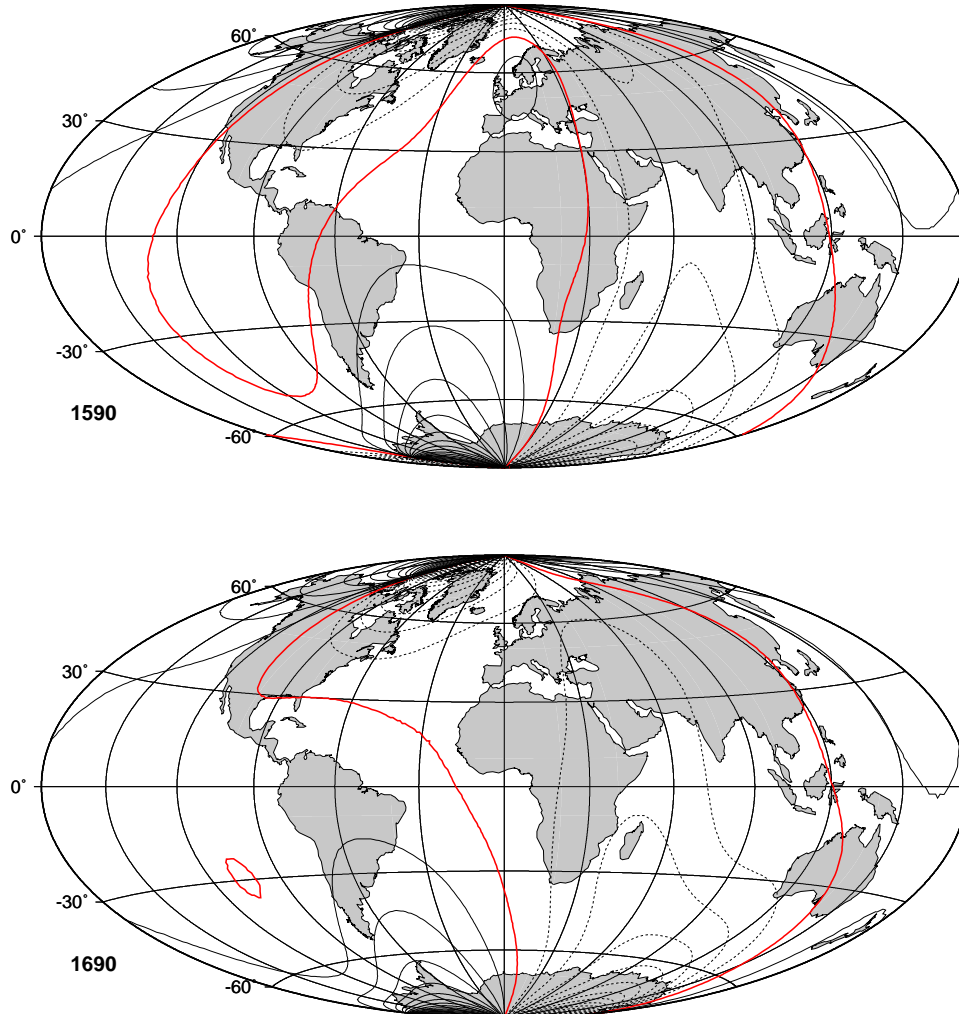


Figure 1.1: Global chart of the Declination (D) derived from *GUFM* [Jackson et al., 2000] for 5 epochs 1590, 1690, 1790, 1890 and 1990 from top to bottom. The red line is the zero Declination line (agonic line). Units are degrees.

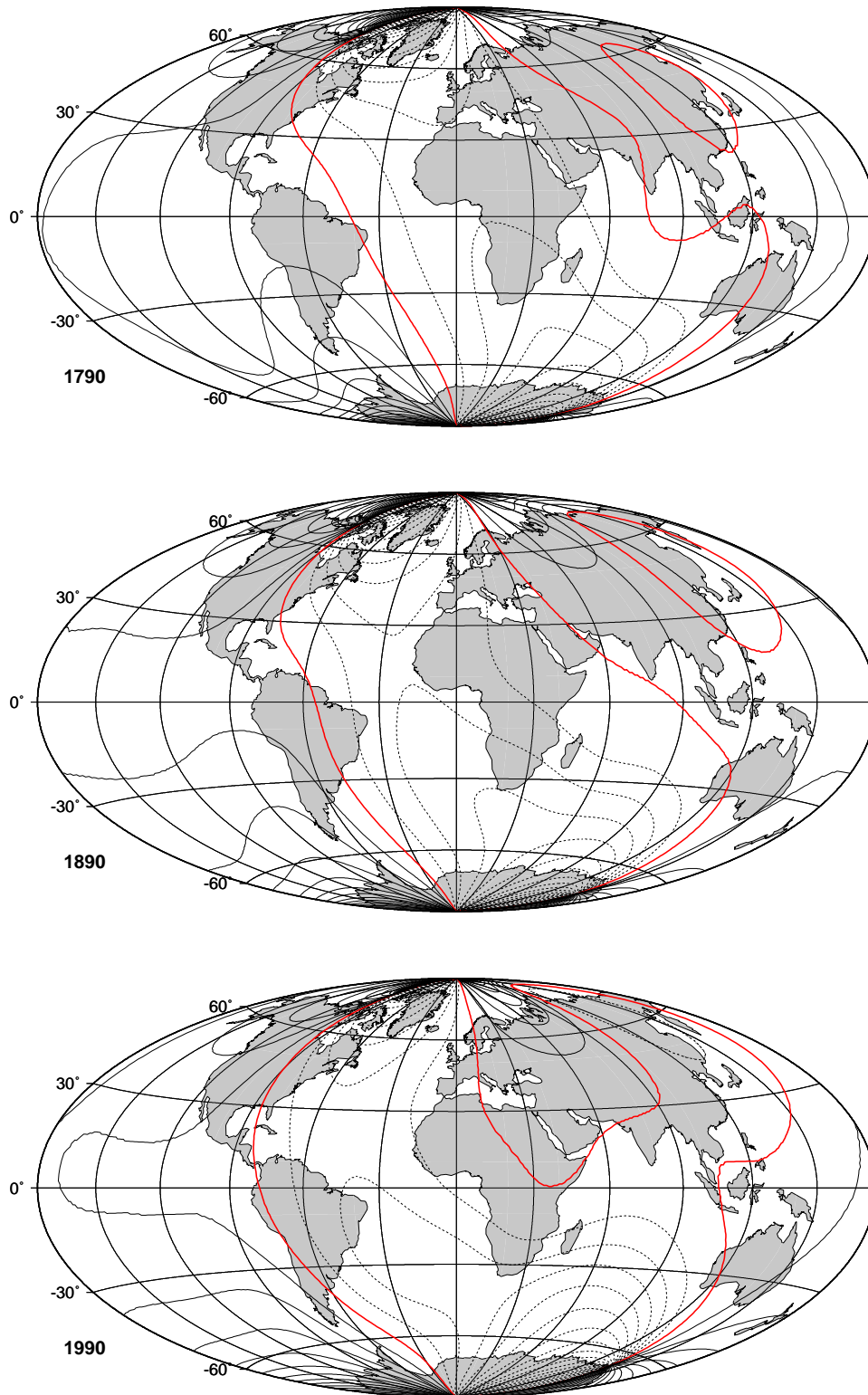


Figure 1.1: Concluded.

From discussion of fig.(1.1), part of the field seems to drift and part not. Langel [1987] discusses several methods to quantify the westward drift. The basic assumption therein is that the entire temporal change of the field is due to the westward drift. Following [Langel, 1987, p. 445, method 2], a crude estimate of the drift can be achieved by minimizing

$$\chi = \sum_i [C(\theta, \phi_i, t_2) - C(\theta, \phi_i + \Delta\phi, t_1)]^2 \quad (1.4)$$

with respect to $\Delta\phi$, the drift between two times t_1 and t_2 . Here, C is any main field or secular variation component for a fixed latitude θ and longitudes ϕ_i . The drift rate is then given by

$$\dot{\phi} = \Delta\phi / \Delta t. \quad (1.5)$$

For the period 1980 – 2000 the westward drift depends on the latitude, as shown in figure (1.2). The averaged drift rate is $0.11^\circ/\text{year}$ (see for further discussion section 4.1.3). The westward drift is by no means steady in time: rather, it shows a complex transient

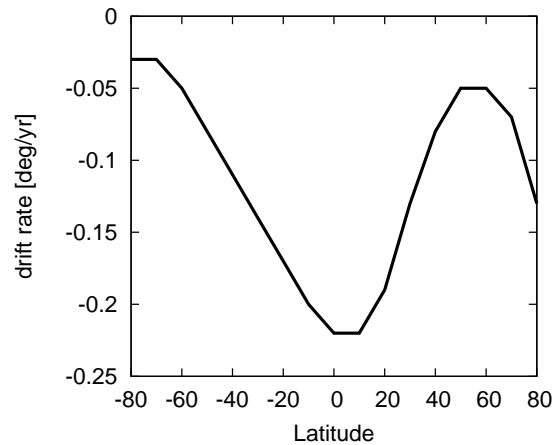


Figure 1.2: Westward drift for different latitudes during the period 1980 – 2000. After [Langel, 1987, p. 445, method 2].

behaviour, which seems to be related to what is known as geomagnetic jerks. Such jerks are event-like features which show up as a change of sign of the slope of the secular variation, a discontinuity in the second time derivative of the field, most clearly seen in the east (Y) component of the geomagnetic field. For the last 100 years at least seven jerks have been reported (1912, 1925, 1969, 1978, 1983, 1991 and 1999), some of them of global extent. The 1969 event (first described by Courtillot et al. [1978]) was widely investigated; on the basis of observatory records Courtillot et al. [1978] and Malin & Hodder [1982] showed its global extent, although it was not evident in all field components. This fact and the coinstantaneous occurrence of jerks and Sun spot maxima hinder the understanding of the

causative processes for jerks, as the lively discussion between Allredge and McLeod in the 1980's shows [Allredge, 1984; McLeod, 1985; Backus et al., 1987].

In addition to long term behavior and short term events the geomagnetic field also exhibits periodic variations. Most of the variations have been identified as external, including the single solar cycle, its harmonics [Currie, 1966, 1976] and a quasi-biennial variation generated by solar activity [Sugiura & Poros, 1977]. The origin of variations with a near 22-year period is less clear. As Allredge [1977] pointed out, the origin of these variations cannot be external because they occur at only a subset of observatories and do not have a common phase. Even longer periods have been found in geomagnetic observatory measurements. The most interesting, a 60-year period [Slaucitajis & Winch, 1965; Currie, 1973], which could be associated to torsional oscillation in the core [Braginskii, 1970].

An apparent periodicity of nearly 60 years occurs also in the decadal change of the length of days (Λ). Vestine [1953] and Vestine & Kahle [1968] showed an evidence for a correlation between Λ and the westward drift, and also it seems that a slow down of the mantle or spin up of the core precede a jerk [Kahle et al., 1969; Davis & Whaler, 1997].

The origin of the Earth's magnetic field is most likely due to dynamo action in the Earth's interior, where the field is generated by motions of a conducting fluid [Larmor, 1919]. These motions are driven by the heat loss of the inner core to maintain a convective dissipation of heat to the mantle.

The origin of secular variation could be either due to MAC-wave dynamo [see Finlay & Jackson, 2003; Finlay, 2004b, for recent discussion] or due to fluid flows at the core-mantle boundary. MAC-waves are magnetohydrodynamic waves which are dependent on magnetic, Archimedean (buoyancy) and Coriolis force, therefore MAC-waves. They occur on diffusive time scales (≥ 300 years) and might account to the long term secular variation and westward drift. As this thesis will point out, core-surface flows have the ability to account for the most of the short term secular variation. An interaction of MAC-waves and core-surface flows is very conceivable.

1.3 Outline of this thesis

In this study I focus on the secular variation over the period 1980-2000. This time interval is bracketed by high-quality satellite vector data (from MAGSAT in 1980 and ØRSTED and CHAMP in 2000). My aim is to model the magnetic field and secular variation simultaneously throughout this period by a fit to all available data. The use of the two satellite epochs as “bookends” will enable a higher resolution of secular variation modelling than has been possible to date. In particular, we hope to answer the question as to whether we can see subdecadal or shorter period variation in the internal field, which in turn will provide important constraints on processes in the core.

As already mentioned, an important feature of the secular variation is the occurrence of geomagnetic jerks. In chapter 2 I will analyze how much of the jerk signal for the best known jerk in 1969 and the secular variation can be modeled by external variation;

this study is undertaken for three geomagnetic observatories Eskdalemuir, Hermanus and Kakioka.

Chapter 3 gives the description of data, data processing and satellite models used for simultaneous time-dependent modelling of main field and secular variation. Also the modelling approach is developed in this chapter. In chapter 4 the time-dependent model is inverted to assess the fluid motion at the core-mantle boundary. Herein different assumptions of the nature of the flow and their prediction of secular variation and the angular momentum budget are analysed. The fifth chapter summarizes the findings and provides some prospects.

Chapter 2

A deterministic model of the temporal variation of the geomagnetic field

*The art of prophecy is very difficult –
especially with respect to the future.*

Mark Twain

Much of the scientific controversy regarding the origin of geomagnetic jerks is certainly a result of the difficulty in distinguishing between fields of external and internal origin. It is also very puzzling, that the appearance of jerks and solar maxima in the last three decades coincide suggesting a coherent cause. However, the most clearly observed jerk, which occurred around 1969, appeared in period where the solar maximum was weaker than the adjacent ones, and the jerks around 1958 and 1978 were not observed globally (c.f figure 2.1 and 2.2).

This chapter presents an attempt to describe the geomagnetic field variation in terms of a deterministic model. For this study the magnetic field measurements of three observatories are examined. The first step is to look at a variety of measures of magnetic activity to explore the periodicity which one might expect in geomagnetic field measurements. I seek to eliminate the variations caused by external field fluctuations from a time series of geomagnetic observations in three Magnetic observatories Eskdalemuir (ESK, Scotland) Hermanus (HER, South Africa) and Kakioka (KAK, Japan) to gain some insights onto the short term variations caused by internal processes. The procedure relies on a deterministic model of these fluctuations and the steady secular variation. Therefore geomagnetic records of the period 1957 – 2001 are examined; while this extends outside our main period of interest, the most studied and strongest geomagnetic jerk appeared in this period, around 1969.

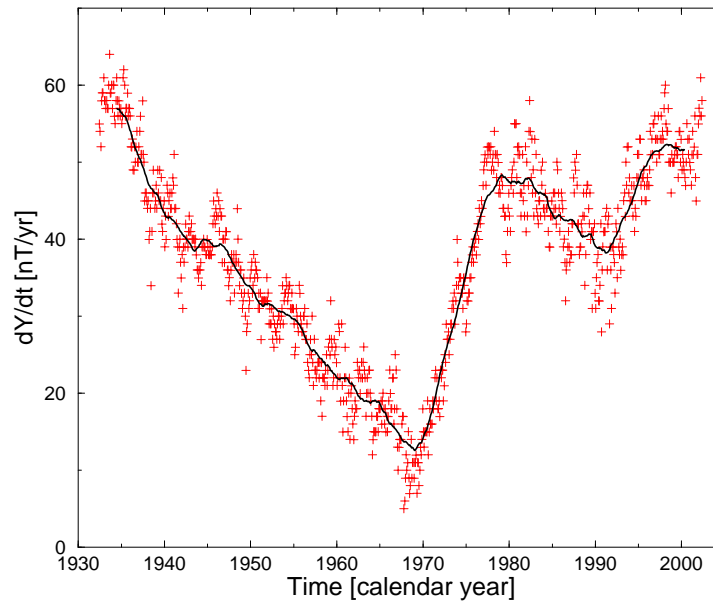


Figure 2.1: The secular variation of the east magnetic component (dY/dt) for Eskdalemuir (Scotland) from 1932 to 2002 (red dots). The black solid line is a moving average of the red dots. The geomagnetic jerks, around 1969 and 1991 are both present in the series. The jerk around 1999 is less clear.

2.1 Analysis of the external field variation

The interactions of the solar wind with the Earth’s core field, influencing the dynamics of the magnetosphere and ionosphere, cause secondary magnetic fields (external fields) [Chapman & Bartels, 1940] and the fluctuation of these external fields induces currents in the lithosphere which result in tertiary time varying fields (induced fields) [Banks, 1969]. These field contributions are subsumed as disturbance fields and are directly linked to solar activity. As good proxies for solar-related disturbances the sun spot numbers, the EUV-Index, Ap-Index and D_{ST} -Index are analyzed to reveal typical time scales for disturbance field contributions.

The sun spot numbers (SSN) are defined as

$$N_Z = k(10g + n),$$

where k is a correction factor for the observer, g the number of identified sun spot groups and n the number of individual spots. These numbers, also known as Zürich numbers, were introduced by Wolf in 1848 and provide the longest continuous measure of solar activity. They show a quasi periodic variation of 10.6 years, which is referred as solar cycle. The SSN directly indicate the solar activity: high SSN connote high solar activity.

The EUV-Index represents the extreme ultraviolet flux, produced by the sun, integrated from 1 – 105 nm. Its units are $\text{Wm}^2 \text{H}^{-1}$.

The Ap-Index monitors the disturbances in the horizontal field components caused by

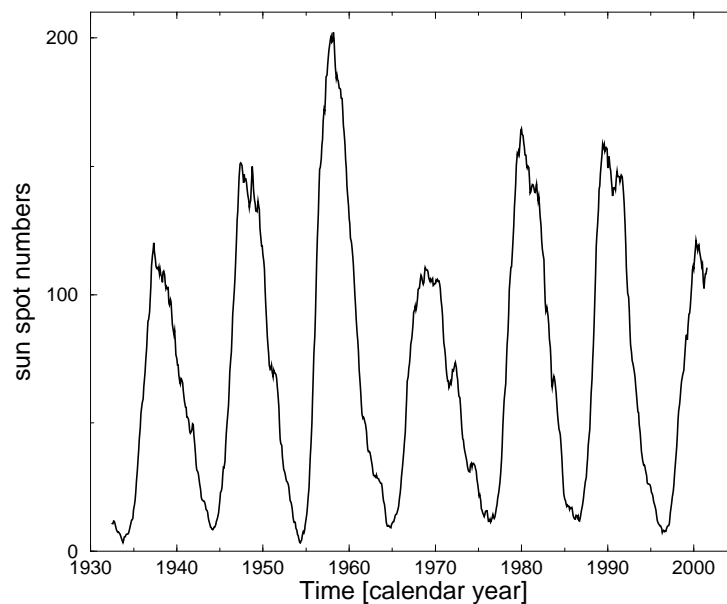


Figure 2.2: Smoothed and monthly averaged sun spot numbers, from 1932 to 2002.

solar particle radiation. It is calculated from 13 geomagnetic observatories, and reflects disturbances of the Earth's magnetic field due to solar activity.

The D_{ST} (Disturbance storm-time) index represents the axially symmetric disturbance of the magnetic field at the dipole equator on the Earth's surface [Sugiura, 1964]. D_{ST} values above -20 nT correspond to quiet behaviour of the field, values below -50 nT indicate a moderate disturbance in the field. In extreme cases, D_{ST} can drop to below -400 nT. D_{ST} is measured by a equatorial chain of observatories, which send their data to the World Data Centre for Geomagnetism, Kyoto¹. Because preparing the D_{ST} -index for scientific study is a complex process, several versions of D_{ST} are released, from quick-look D_{ST} which is released between 12 and 36 hours after the measurements are made, to the definitive D_{ST} -index, which arrives several years afterwards.

In order to quantify typical frequencies of the disturbances and the magnetic activity external to the Earth the spectral power density function (SDF) of the SSN, EUV-, Ap- and D_{ST} -Index are estimated, from data covering the period form 1932 – 2001, and also for the, where data are available from 1957 – 2001.

A variety of spectral analysis techniques have been widely employed in the analysis of geophysical processes [Brillinger, 1981, and references therein]. More sophisticated methods have been developed which make more realistic assumptions to the irregular oscillatory behavior (noise) expected in these signals. Among these techniques, the multi-taper method (MTM) for estimations of the SDF is one of the most promising [Park et al., 1987a,b; Ghil et al., 2002].

¹(<http://swdcd.db.kugi.kyoto-u.ac.jp/>)

2.1.1 The multi-taper method

The multi-taper method (MTM) makes use of a multiple orthogonal data taper to describe structures in time series that are modulated in frequency and amplitude. This method provides a spectral estimate with an optimal trade-off between spectral resolution and variance.

Conversely, the standard approach has been to multiply a time series by a data taper (data window such as Hanning, Blackman, Parzen, etc.) which arises when performing a discrete Fourier transform (DFT) to reduce the spectral leakage [see Percival & Walden, 1993, for details on tapering]. The use of only a single taper leads to large variances of the estimates of the SDF. Thomson [1982] introduced the use of multiple orthogonal tapers to avoid this problem and to minimize the spectral leakage. The optimal tapers are defined as the eigenvectors of a minimization problem [Slepian, 1978; Thomson, 1982].

For a given time series $F(t)$, a set of k orthogonal tapers $a_k(t)$ and their Fourier transforms are determined

$$Y_k(f) = \sum_{t=1}^N a_k(t)F(t)e^{i2\pi ft\Delta t}, \quad (2.1)$$

where N is the number of data, f the Fourier frequency and Δt the sampling interval. From (2.1) the multi-taper power spectrum is constructed as

$$S(f) = \frac{\sum_{k=1}^K \lambda_k |Y_k(f)|^2}{\sum_{k=1}^K \lambda_k}. \quad (2.2)$$

λ_k measures the fractional leakage associated with the k^{th} data taper [see Percival & Walden, 1993, for the choice of the λ_k].

2.1.2 Statistical confidence

Discriminating statistics are essential in geophysical studies, where the nature of the temporal variation is complex. A pure line test as given by Mann & Lees [1996] to verify the significance of spectral features against the null hypothesis of a red noise background is utilized here. The red noise hypothesis is a reasonable description of the slowly varying geomagnetic continuum, i.e., secular variation. Significance levels are computed from the quantiles of a chi-squared distribution, assuming that the spectrum has degrees of freedom $\nu \approx 2k$. For our analysis we disregard spectral features below 99% significance.

2.1.3 Results

The spectra of the sun spot numbers and the activity indices show a complex structure, this will not be discussed in detail here. Only those periodicities and harmonics are emphasized which have significant power. At the very low frequency range, at 0.04 cycles/year the 22 years period of the solar turnover is appearing, but the dominating signal in all spectra is the solar cycle at the low frequency end of the spectrum, figure 2.3 (left). The harmonics

of this signal, 0.185 and 0.41 cycles/year (5.4 and 2.45 years period) are also resolved in this spectrum. The peak around 0.71 cycles/year (1.4 years) has been already reported [e.g., Fraser-Smith, 1972; Delouis & Mayaud, 1975; Gonzalez & Gonzalez, 1987] and shows close relation to the sector structure variation of the interplanetary field as well as the occurrences of auroras [Silverman & Shapiro, 1983] and the solar wind speed variation [Paularena et al., 1995; Krivova & Solanki, 2002].

In the intermediate and short-period branch of the spectrum of the sun spot numbers, four peaks are most clearly detectable: 2.35 cycles/year (155 days), 3.76 cycles/year (97 days), 13.5 cycles/year (27 days), 27 cycles/year (13.5 days) and 40.5 cycles/year (9 days). The first variation is related to the recurrence of the solar flares. The solar rotation period shows up as a hump at 13.5 cycles/year; its broad appearance is due to the different rotation period of sun spots at different solar latitudes. Spots close to the solar equator rotate faster than the ones towards the poles. During each solar cycle the spot locations move from $\pm 35^\circ$ latitude towards the equator. The peak at about 27 cycles/year, half the solar rotation, originates from two high speed streams per solar rotation. According to the tilted solar dipole model, such two-stream structure appears if the heliospheric current sheet is narrow and tilted [Mursula & Zieger, 1996].

All of these periodicities are apparent in the EUV-Index and also in the spectra of the proxies of geomagnetic activity and disturbance field, see figures 2.4, 2.5 and 2.6. Further, the geomagnetic activity indices feature three additional periods. An annual fluctuation appears due to variation of the solar wind speed. It is known [Zieger & Mursula, 1998], that the solar wind speed is asymmetric with respect to the solar equator. And as the Earth revolves around the sun it changes its heliocentric latitude from 7.2° to -7.2° ; thus, it is affected by different solar wind conditions in its equinoxes. A semi-annual line is also evident in the spectra of geomagnetic activity indices, most likely caused by geometrical variation of the ring current, a current system in the sunlit magnetosphere at 5 - 6 Earth's radii distance. Furthermore a period of 9 days is clearly visible in the spectra of Ap - and D_{ST} -index, which is believed to be the second harmonic of the solar rotation. Table 2.1 lists all significant signals, their frequency, periods and origin.

2.2 The formalism for the deterministic modelling of the disturbance fields

In this section a deterministic time series model is developed to eliminate the variation of the disturbance fields and the long term behaviour of the secular variation from geomagnetic field observations. This model is based on the results of the previous section and should only model these contribution for a period from 1957 - 2001.

In general the disturbances vary in a transient and irregular manner and the predominant duration of these is of the order of seconds to hours. However, a simple time averaging of the field cannot be expected to remove the effect of disturbance phenomena [Stewart & Whaler, 1992], because of the modulation by the solar cycle or longer cycles. The time

Frequency [cycles/year]	Period	Origin
40.5	9 days	possible harmonic of the solar rotation
27.0	13.5 days	two high speed streams per solar rotation
13.5	27 days	solar rotation
3.76	97 days	solar origin, but unknown cause
2.35	155 days	solar flare period
2.0	183 days	semi-annual variation
1.0	365 days	period of the Earth's revolution
0.41	2.4 yrs/894 days	solar cycle harmonic
0.18	5.4 yrs/1972 days	solar cycle harmonic
0.09	11 yrs/3872 days	solar cycle
0.04	22 yrs/7743 days	solar magnetic field turnover

Table 2.1: Periods of solar and geomagnetic activity.

series analysis of the magnetic activity indices, EUV-Index and SSN reveals at least 11 substantial periodicities, all listed in table 2.1.

2.2.1 Method

To build the deterministic model I adopt an approach introduced by Gavoret et al. [1986] and developed by Stewart & Whaler [1992] to separate external and internal signals from the geomagnetic field. The model is set up to reproduce secular variation estimates (first time derivatives) of geomagnetic field components. These are computed using, e.g.

$$X(t) = X(t + 183[days]) - X(t - 182[days]), \quad (2.3)$$

where t is an integer and indicates the day of the year and 182 and 183 days are the nearest integer values of half a year, respectively. The model is linearly constrained by the solar sun spot numbers (D_{ST} - and Ap-Index might be affected by secular variation, and therefore are only optionally considered in the modelling scheme) and as linear combination of sines and cosines with the typical periodicities

$$M(t) = \beta_0 + \beta_1 SSN(t) + \beta_2 AP(t) + \beta_3 D_{ST}(t) + \sum_i [\beta_i \sin(t/T_i) + \beta_{i+1} \cos(t/T_i)], \quad (2.4)$$

where $M(t)$ is the prediction of the secular variation of a field component at a certain time t . The coefficients α_i and β_i are assumed to be time invariant.

$$\{T_i\} = \{9, 13.5, 27, 97, 155, 183, 365, 894, 1972, 3872, 7743\}$$

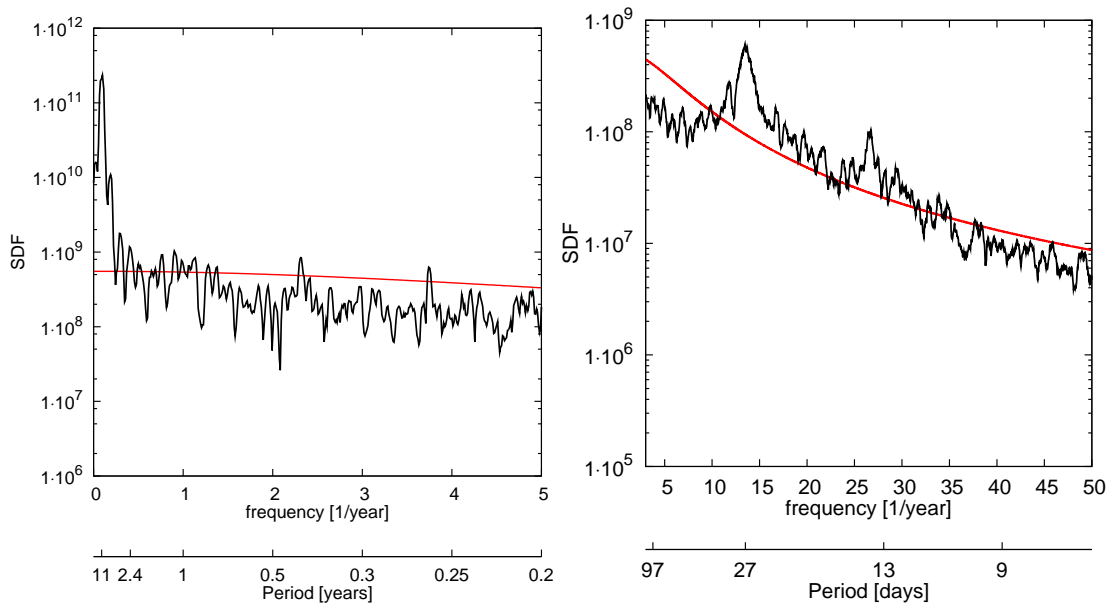


Figure 2.3: Spectral power density of the daily sun spot numbers from 1932 – 2001. The black curve is the smoothed spectrum, and the red line indicate the 90% significance level.

is the set of typical periods given in days. For the modelling, the general form of this kind of parametric model is

$$y(t) = \sum_{k=1}^M \alpha_k f_k(t) \quad (2.5)$$

where $f_k(t)$ are functions of t , called the basis functions and could in general be non-linear. Now defining the misfit between data and model

$$\chi^2 = \sum_{i=1}^N \left(\frac{y_i - \sum_{k=1}^M \alpha_k F_k(x_i)}{\sigma_i} \right)^2 \quad (2.6)$$

where σ_i is the measurement error of y_i (if it is unknown, it is set to $\sigma_i = 1$).

For convenience (2.5) is given in its matrix form

$$\mathbf{b} = \mathbf{A}\mathbf{x}, \quad (2.7)$$

where

$$\mathbf{b} = \frac{y_i}{\sigma_i}, \quad \mathbf{A}_{ij} = \frac{F_j(f_i)}{\sigma_i}, \quad \mathbf{x} = \{\alpha_1, \dots, \alpha_k\}. \quad (2.8)$$

To solve this linear least-squares problem, I apply a technique known as singular value decomposition, or SVD [Golub & van Loan, 1989; Press et al., 1993]. The singular value

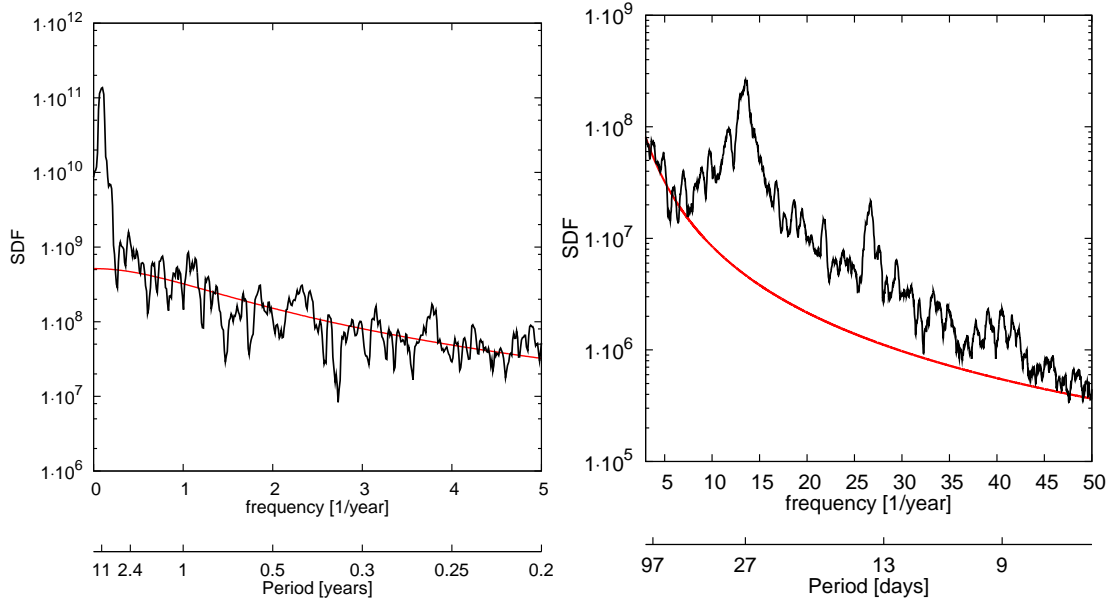


Figure 2.4: Spectral power density of the daily means of the EUV-Index from 1947 – 2001. The black curve is the smoothed spectrum, and the red line indicate the 90% significance level.

decomposition theorem says that any $M \times N$ matrix \mathbf{A} whose number of rows M is greater or equal to its number of columns N has a factorization of the form

$$\mathbf{A} = \mathbf{U}\mathbf{W}\mathbf{V}^T, \quad (2.9)$$

where \mathbf{U} is an $M \times M$ unitary matrix and \mathbf{V} is an $N \times N$ unitary matrix, both of which have orthogonal columns so that

$$\mathbf{U}^T\mathbf{U} = \mathbf{V}^T\mathbf{V} = \mathbf{1}. \quad (2.10)$$

\mathbf{W} is an $M \times N$ diagonal matrix, whose diagonal entries are non-negative real numbers in descending order. Then the SVD provides a numerically robust solution to the least squares problem even if \mathbf{A} is singular or close to singular. The general solution

$$\mathbf{x} = (\mathbf{A}^T\mathbf{A})^{-1}\mathbf{A}^T\mathbf{b} \quad (2.11)$$

of the least squares problem becomes with (2.9)

$$\mathbf{x} = \mathbf{V}\mathbf{W}^{-1}\mathbf{U}^T\mathbf{b}, \quad (2.12)$$

where \mathbf{x} minimizes (2.6).

The algorithm is arranged in 7 steps:

1. Find the eigenvalues λ_i of the matrix $\mathbf{A}^T\mathbf{A}$ and arrange them in descending order.

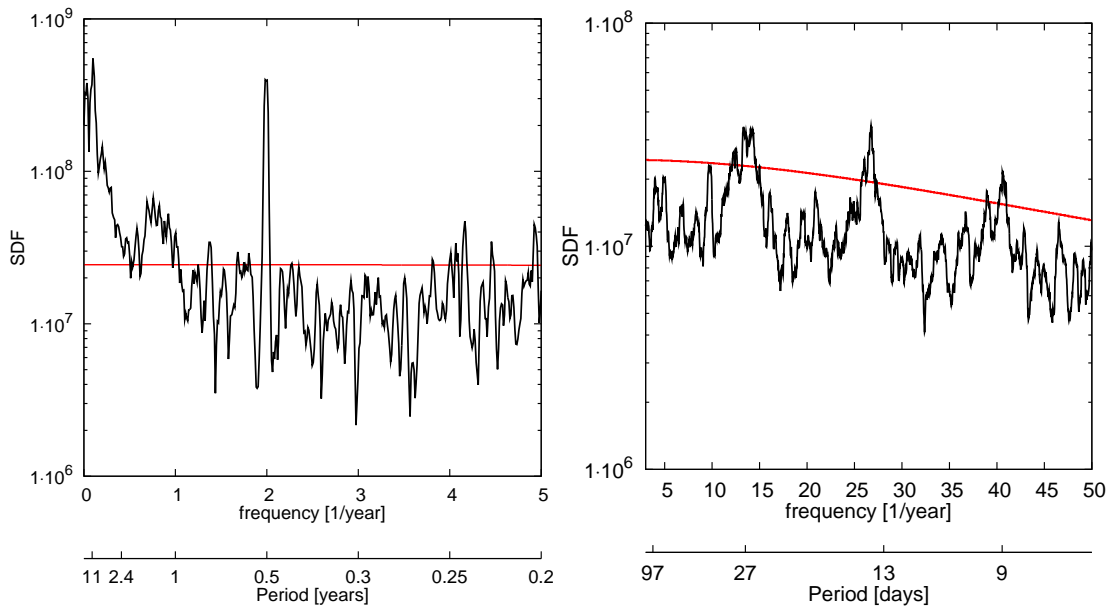


Figure 2.5: Spectral power density of the daily means of the Ap-Index from 1932 – 2001. The black curve is the smoothed spectrum, and the red line indicate the 90% significance level.

2. Find the number of nonzero eigenvalues r of the matrix $\mathbf{A}^T \mathbf{A}$.
3. Find the orthogonal eigenvectors of the matrix $\mathbf{A}^T \mathbf{A}$ corresponding to the obtained eigenvalues, and arrange them in the same order to form the column-vectors of the matrix \mathbf{V} .
4. Form a diagonal matrix \mathbf{W} placing on the leading diagonal of it the square roots of first eigenvalues of the matrix $\mathbf{A}^T \mathbf{A}$ in descending order.
5. Find the first column-vectors of the matrix \mathbf{U}

$$\mathbf{u}_i = (\lambda_i)^{-1/2} \mathbf{A} \mathbf{v}_i, \quad i = 1, \dots, r.$$

6. Add to the matrix \mathbf{U} the rest of $m-r$ vectors using the Gram-Schmidt orthogonalization process.
7. Forward computation from the solution \mathbf{x}

$$X(t)^{\text{model}} = \mathbf{A} \mathbf{x}.$$

Then the residuals are given by

$$R(t) = X(t)^{\text{observation}} - X(t)^{\text{model}} \quad (2.13)$$

which are expected to be the remaining internal signal.

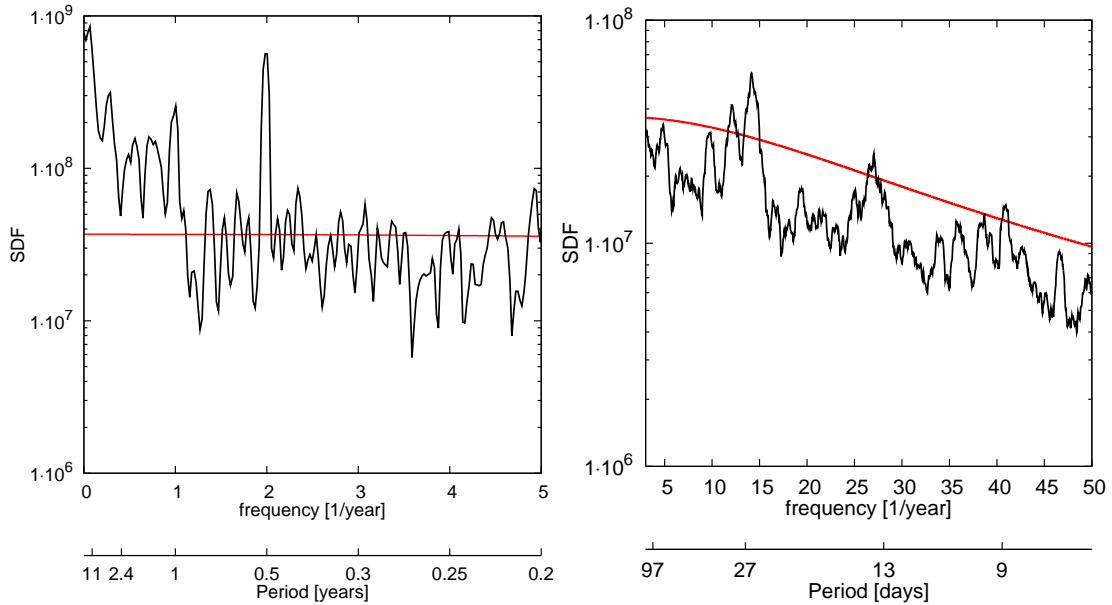


Figure 2.6: Spectral power density of the daily means of the D_{ST} -Index from 1957 – 2001. The black curve is the smoothed spectrum, and the red line indicate the 90% significance level.

2.2.2 Results and Discussion

The left panels of Fig.(2.7), (2.8) and (2.9) show the secular variation estimates of the model (red curve) and derived from the X, Y and Z components of three different observatories (black curve). The model fits the secular variation very well and even recovers the geomagnetic jerks occurred in this period, 1969 and 1991 easily seen in dY/dt at Eskdalemuir. Invoking the D_{ST} -Index reduces the residuals further, shown in Fig.(2.7), (2.8) and (2.9) (right column).

One key to interpret these results is given with the power spectra of the coefficients β_i Fig.(2.10). It shows how much of the power is accounted for the principal frequencies $\{T_i\} = \{9, 13.5, 27, 97, 155, 183, 365, 894, 1972, 3872, 7743\}$ (days) to fit the secular variation. The first 15 coefficients represent periodicities up to 365 days. These are more or less of the same order. The 16. and 17. coefficients represent the 11-year solar cycle, 18 and 19 are the coefficients for 894-days period, coefficients 20 – 23 are the ones of the 1972 and 7743 days periods and coefficients 24, 25 belong to the $SSN(t)$ and $AP(t)$. The D_{ST} -Index is not considered in this analysis. Much power is accounted to the long term variation.

In contrast, results by Yukutake [1965], who analysed the solar cycle effect to the secular variation on the basis of a spherical harmonic decomposition, indicated that this effect is rather weak. However, disregarding long term periods ($T_i > 365$ days) leaves a significant amount of unmodeled signal, as shown in Fig.(2.11), (2.12) and (2.13). In order to eval-

uate the long term behaviour a model was derived where the four longest periods $\{T_i\} = \{894, 1972, 3872, 7743\}$ were replaced by fake periods $\{T_i^f\} = \{1200, 2500, 3000, 10950\}$ (days). Table (2.2) gives the rms misfit of the three models (invoking all periods resulting from the time series analysis of solar and geomagnetic activity, the short term periods and fake periods). The rms misfits of the fake model and those of the model with the real periodicities do not differ significantly and even for Hermanus the fit is improved. Therefore, it is not clear, if the long term behaviour of the secular variation are really caused by long term external variations, such as the solar magnetic field turnover.

2.3 Arguments against the external field variations cause of jerks

I would like to argue for a non-external origin of geomagnetic jerks on ground of two arguments:

1. The effect of solar activity phenoma, such as solar magnetic field turnover, the 11 year solar cycle and its harmonics should average out and should be zonal in the Earth coordinate frame, whereas the geomagnetic jerks are not zonal by nature [see figures 17 and 18 of Alexandrescu et al., 1996].
2. Only the geomagnetic jerks occurred 1969, 1991 and clearly detectable in the Y component of European observatories, show a conspicuous 22-year period, but why are there no jerks around 1947 detectable in Eskdalemuir?

This line of arguments does not rule out a linkage of the solar magnetic field turnovers and the occurring of geomagnetic jerks, but the evidence is rather weak. As these models are only valid for a single location a much stronger persuasiveness would have the results of the same analysis, but carried out on a time-dependent model of the internal field, i.e. *GUFM*. A future plan could be the description of the Gauss coefficients belonging to such model by a single deterministic model.

Observatory	Model	X	Y	Z
Eskdalemuir (ESK)	all	12.7953	8.86353	14.4843
	short term	16.3296	14.8127	16.7678
	fake	12.9739	9.10849	16.5145
Kakioka (KAK)	all	21.4368	5.29365	10.10121
	short term	24.7739	8.35060	24.5176
	fake	21.5067	5.67791	10.7869
Hermanus (HER)	all	20.8919	8.80827	9.64212
	short term	28.3469	18.0062	10.9068
	fake	20.9287	8.57450	9.62499

Table 2.2: The rms misfit for three different observatories and three deterministic models.

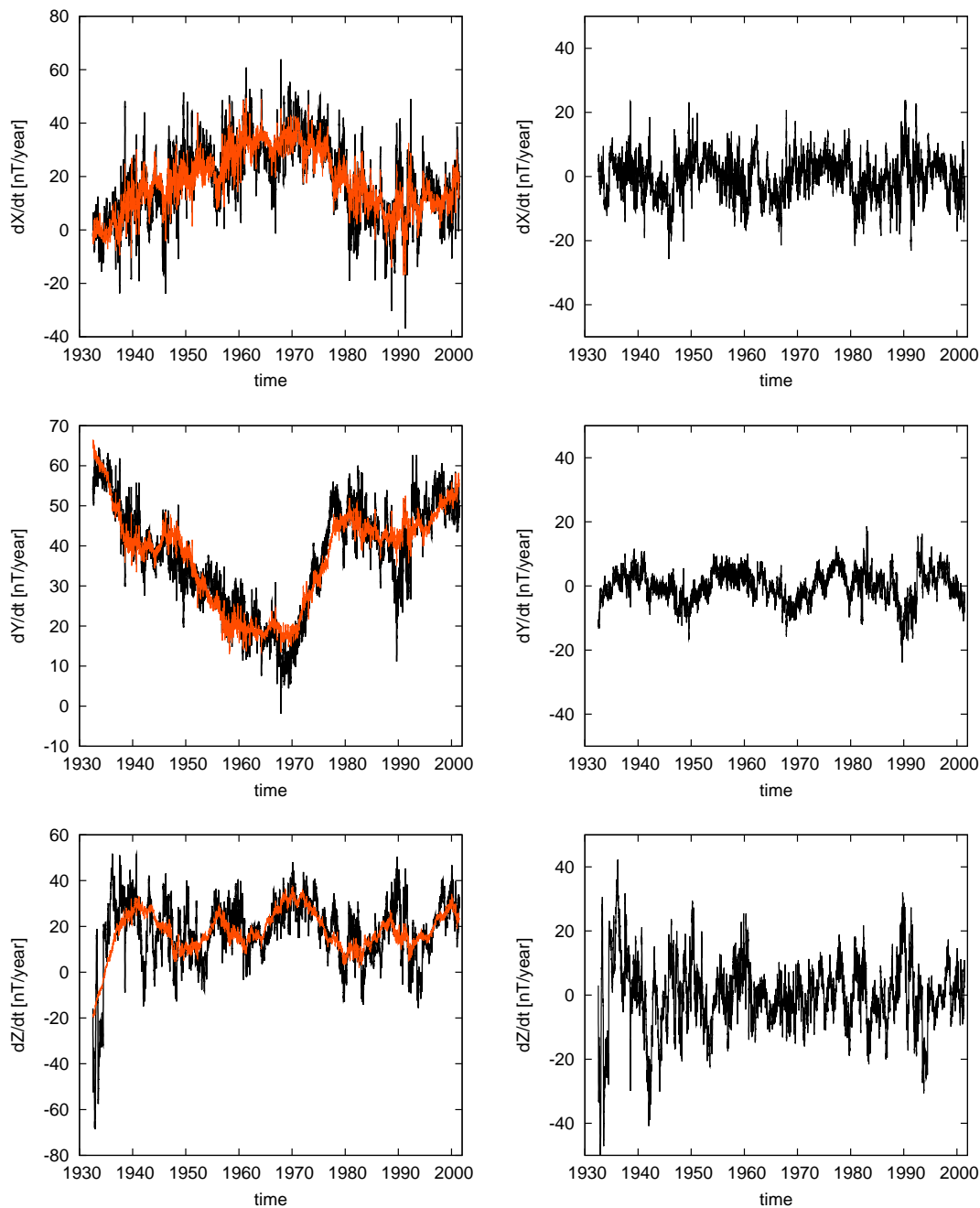


Figure 2.7: The left figures are the direct comparison of the prediction of deterministic model (red curve) valid for the period 1932 – 2001 and secular variation estimates for the X, Y and Z component in Eskdalemuir (from top to bottom, black curves). All curves are smoothed by a moving average of 20 days. The right column pictures are the remaining signal, the residuals, which cannot be explained by the deterministic model (red curve). The black curve represents the smoothed residuals.

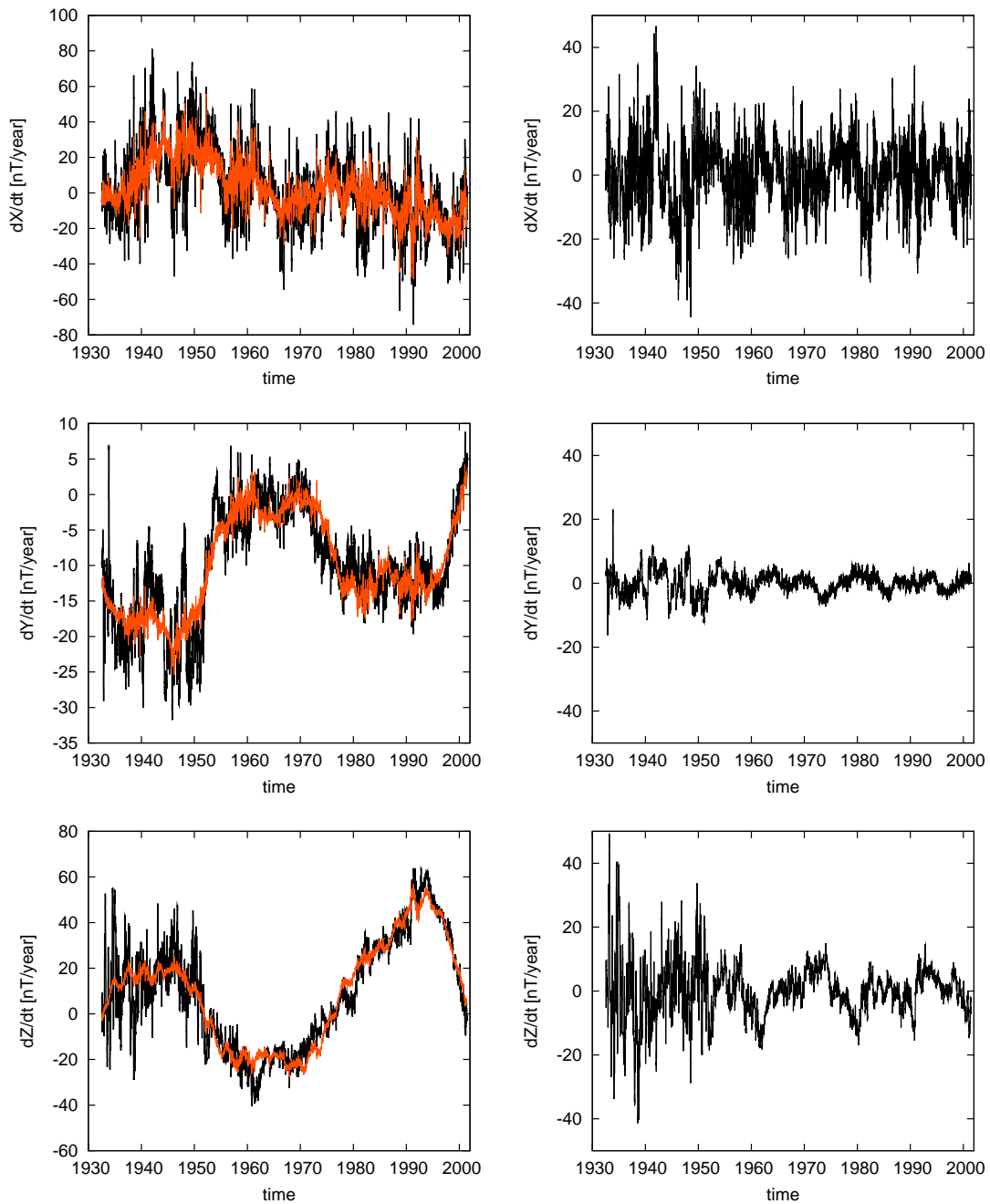


Figure 2.8: The fit to the secular variation estimates for the X, Y and Z component in Kakioka. Curves are assembled and smoothed in same way as in Fig.(2.7).

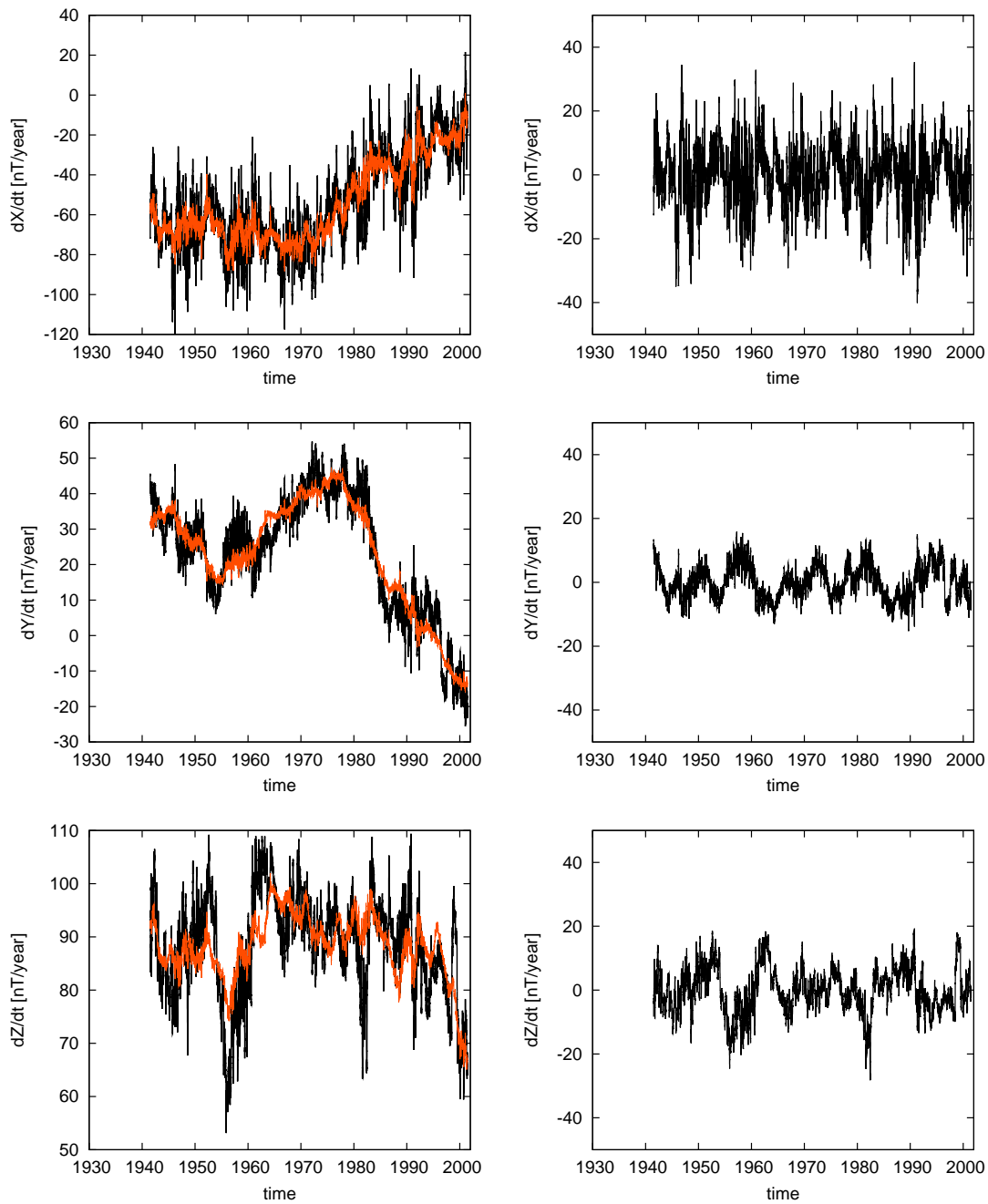


Figure 2.9: Shown here the fit for the secular variation estimates for the X, Y and Z component in Hermanus for the period 1941 – 2001. Curves are assembled and smoothed in same way as in Fig.(2.7).

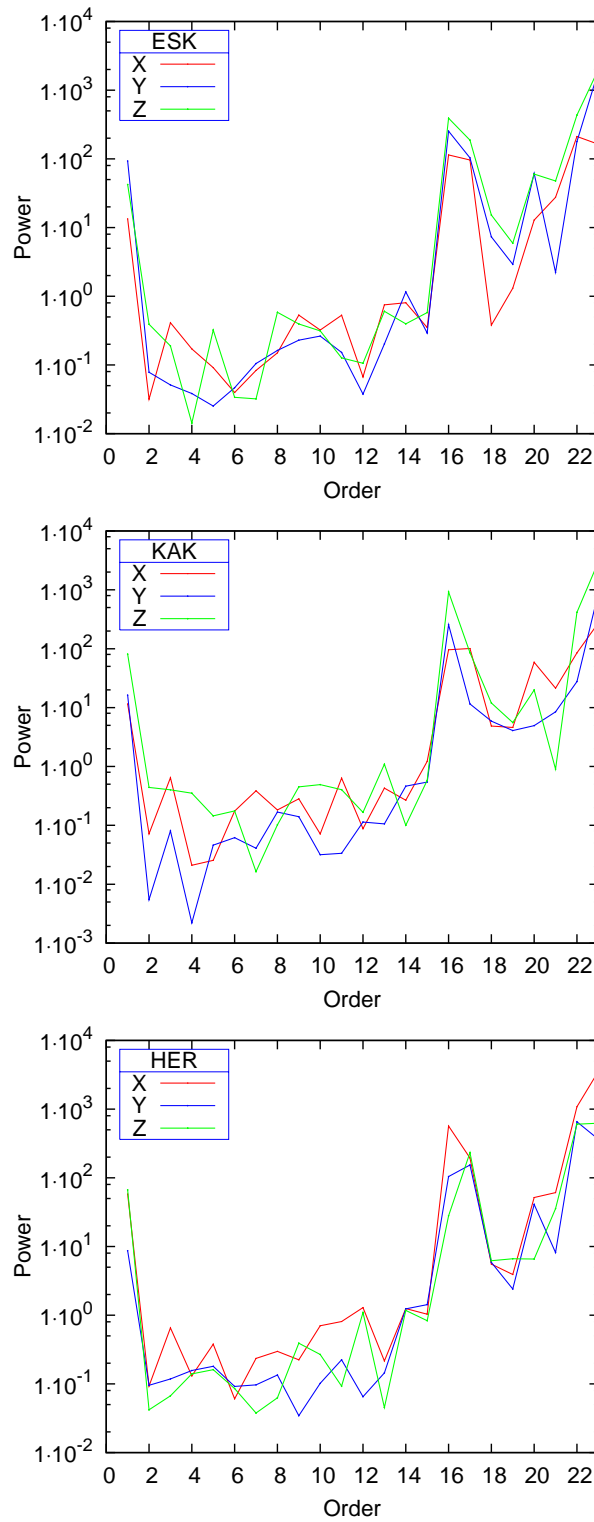


Figure 2.10: Spectra of the principal components coefficients for X, Y and Z of the analysis of the three sites Eskdalemuir (ESK), Kakioka (KAK) and Hermanus (HER).

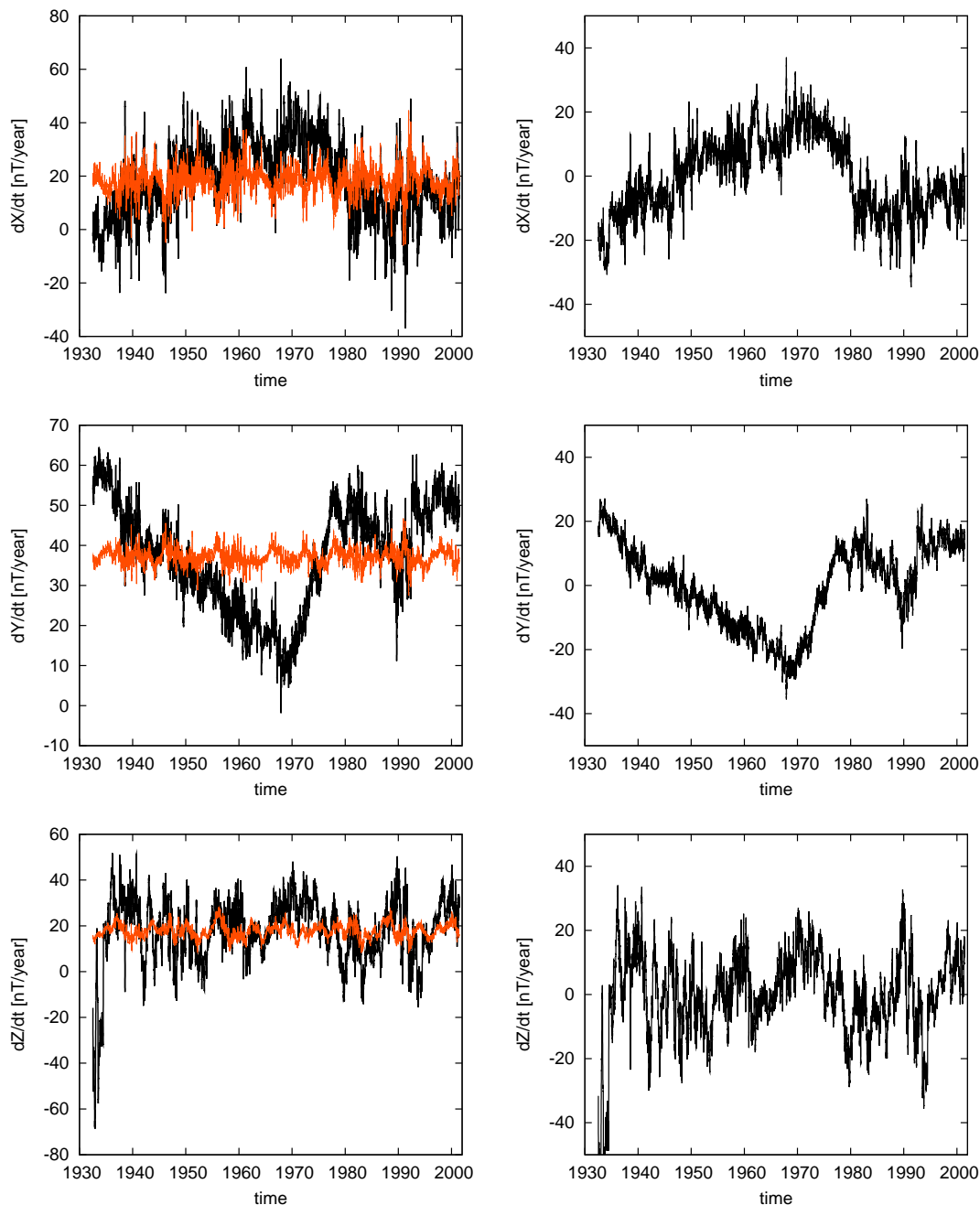


Figure 2.11: The left figures are the direct comparison of the prediction of deterministic model considering only short periods (red curve) valid for the period 1932 – 2001 and secular variation estimates for the X, Y and Z component in Eskdalemuir (from top to bottom, black curves). All curves are smoothed by a moving average of 20 days. The right column pictures are the remaining signal, the residuals, which cannot be explained by the short periods of the deterministic model (red curve). The black curve represents the smoothed residuals.

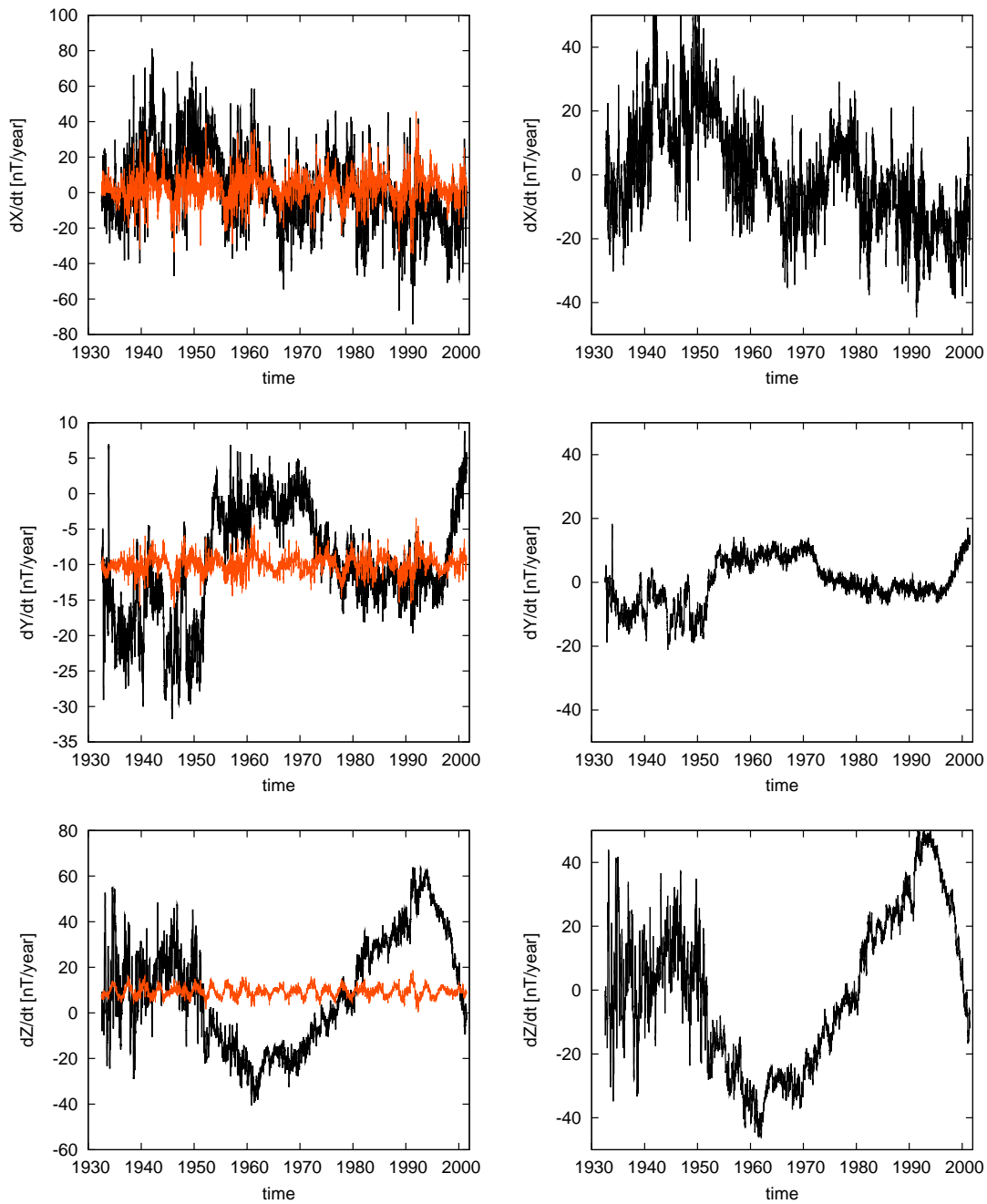


Figure 2.12: Shown here the fit for the secular variation estimates for the X, Y and Z component in Kakioka for short periods only. Curves are assembled and smoothed in same way as in Fig.(2.11).

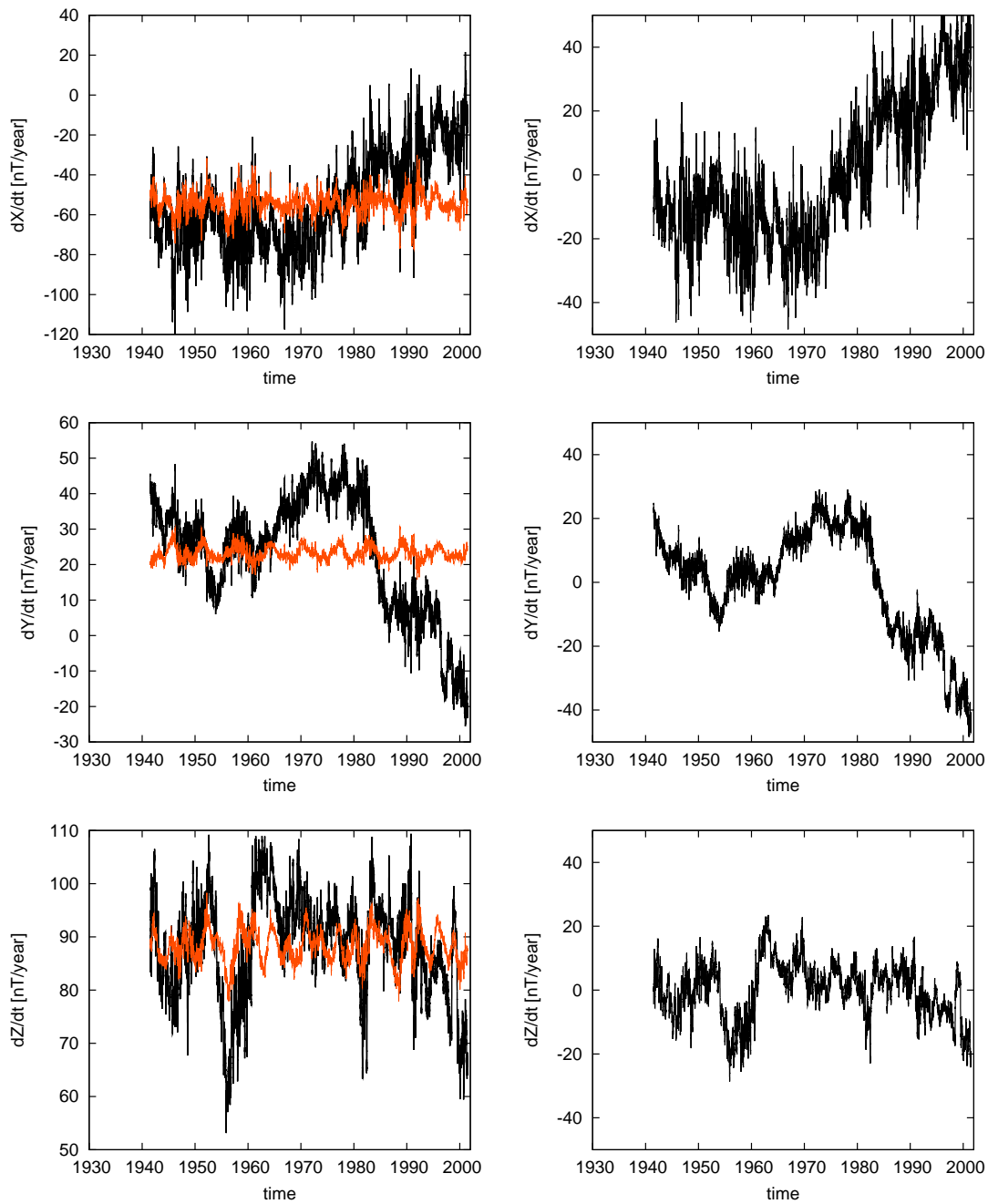


Figure 2.13: Shown here the fit for the secular variation estimates for the X, Y and Z component in Hermanus for short periods only. Curves are assembled and smoothed in same way as in Fig.(2.11).

2.4 Conclusions

In this chapter a method has been developed specifically for the analysis of the influence of solar related activity phenomena to the geomagnetic field at a individual location. The algorithm considers all significant periodicities deduced from a time series analysis of the sun spot numbers, EUV-, D_{ST} - and Ap-Index. Then the algorithm is set up to model the geomagnetic field variations as a superposition of harmonics of these periodicities. The model fit is achieved in linear least squares sense by using a singular value decomposition. Observation and predictions for each magnetic field component are differentiated in time to gain a secular variation estimate and then compared to each other. Consequently, the unmodeled signal, which cannot be explained in terms of disturbance field variation, should therefore represent the noise-free secular variation.

This analysis reveals that almost all of the secular variation can be explained by a simple deterministic model, which superpose all significant periods of solar and Earth-Sun interaction phenomena. But caution has to be paid for two reasons: First, a simple model which is partly built up with artificial long periods (fake model) explain the secular variation at the three station evenly good as the real deterministic model. Secondly, the fact that this model is not capable of distinguishing between external and internal variations on the basis of typical time scales of those variations, is important. And therefore, the conclusion drawn from the comparison of the observations between the model predictions, that the geomagnetic jerks originate externally is not necessarily correct. The rest of this thesis will consider a model of the field observations based on an internal field. With this model, I will be able to fit the jerk signal, suggesting further that jerks are primarily of internal origin.

Chapter 3

Time-dependent modelling of the geomagnetic field

*A lack of information cannot be remedied by
any mathematical trickery.*

C. Lanczos

In this chapter I will outline the method used for the simultaneous time-dependent field modelling of the geomagnetic main field and its secular variation between 1980 and 2000. The idea of simultaneous inversion of main field and secular variation dates back to Cain et al. [1965] and has been further developed by Bloxham [1987]; Bloxham & Jackson [1989].

The new aspect of the methodology developed in this thesis is the usage of additional a priori information to constrain the time-dependent model in 1980 and 2000 by field models of high-quality satellite vector data. The use of the two satellite epochs as “bookends” will enable a higher resolution of secular variation modelling than has been possible to date.

I will begin this chapter with a description of the data and data processing. Then follows some basic discussions of inverse problems and their solution. In section 3.4 I will describe the new method used to develop time-dependent models of the geomagnetic main field and the secular variation. Also, I hope to make clear, why such a intricate apparatus is required to model the Earth’s magnetic field. The results are presented in section 3.5.

3.1 Data

The data used in this work are magnetic observatory annual means, monthly means and repeat station measurements. The observatory annual means and the repeat survey data were kindly provided by S. Macmillan (British Geological Survey (BGS), Edinburgh). Monthly means, defined as being the average over all days of the month and all times of the day, were derived from hourly mean values downloaded from the World-Data-Center Copenhagen¹ and from the Intermagnet database². Table (A.1) lists observatories and repeat

¹(<http://web.dmi.dk/projects/wdcc1/master.html>)

²(http://www.intermagnet.org/myservlet/imotbl_e.jsp)

stations locations from which the data were used, the number of data for each field component and its uncertainty estimates. The computation of the errors for each component will be outlined in chapter 3. Figure (3.1) shows the global distribution of the observatories, where the different symbols correspond to observatories with monthly means (red circle), observatories with only annual means (black circle). A similar map (figure 3.2) is drawn for the repeat stations: a red triangle indicate multiply visited stations and black triangle station only visited once.

3.1.1 Geomagnetic observatory data

For the field modelling three components, northward (X), eastward (Y) and downward (Z), were compiled for each single observatory. Table (A.1) lists the number of available data for each component and observatory. The coding of the observatories is basically identical with the 3 character coding of IAGA (International Association of Geomagnetism and Aeronomy), but it differs for those sites, where location changes happened between 1980 and 2000, or an observatory with the same coding already existed at another location. These stations are marked with an additional digit after the IAGA-coding, and although a correction of these changes for most sites would be possible, it was not applied, e.g. Tucson as TUC1 and TUC2. Also sites, where for a longer period no data are available are marked with an extra digit, for example Addis Abbeba (Ethiopia), AAE1 before 1995.2 and AAE2 after 1997³.

Table (B.1) lists the known base line jumps, site changes or instrument changes during the period 1980 and 2000.

3.1.2 Repeat station data

Repeat stations are established to record the secular variation in a certain region. The spatial resolution should be high but is typically less than that for the ground measurements carried out to map magnetic anomalies. As the name implies, repeat stations mean a network of fixed sites, where the magnetic field is measured at a more or less regular interval. The occupation interval varies between one year and 10 years; in this study, it is restricted not to be longer than seven years. Any occupation period beyond that is believed not to be useful to uncover short term secular variation as analysed in this study.

The data of repeat surveys are commonly provided after they have been reduced to an epoch, such as annual mean. The reduction is made using

$$C_{rp}(t) = C_{rp}(t_0) + C_{obs}(t) - C_{obs}(t_0), \quad (3.1)$$

where $C_{rp}(t)$ is the annual mean of the repeat station, $C_{rp}(t_0)$ the repeat station measurement, $C_{obs}(t)$ the observatory annual mean and $C_{obs}(t_0)$ the simultaneous measurement at the observatory. Relation (3.1) assumes, that the difference between the observation and annual mean is the same, i.e. that secular variation and external induced variations

³This coding corresponds to the coding preferred by the BGS

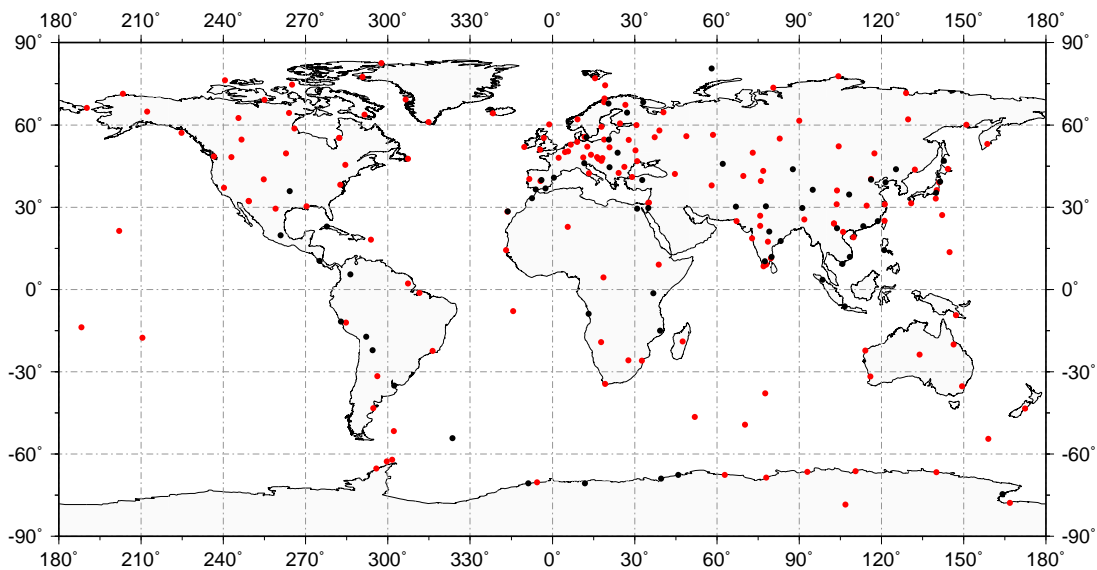


Figure 3.1: Global chart of permanent observatories, red circles shows places for which monthly means are available, black dots for sites where only annual means are available.

$$\begin{array}{l|l}
 X & \pm 5 \text{ nT} - \pm 20 \text{ nT} & \dot{X} & \pm 7 \text{ nT} - \pm 40 \text{ nT} \\
 Y & \pm 4 \text{ nT} - \pm 13 \text{ nT} & \dot{Y} & \pm 3 \text{ nT} - \pm 26 \text{ nT} \\
 Z & \pm 4 \text{ nT} - \pm 12 \text{ nT} & \dot{Z} & \pm 3 \text{ nT} - \pm 24 \text{ nT}
 \end{array}$$

Table 3.1: Error estimates of the magnetic field component X, Y and Z and for their computed secular variations \dot{X}, \dot{Y} and \dot{Z} for European repeat surveys

are identical at the nearby observatory and the repeat station. These idealizations lead to errors in the reduced data depending on the distance from the repeat station to the observatory. If there is no observatory within a radius of 1000 km, then the reduction is sometimes undertaken using a main field model instead of the observatory measurements, but even with main field models (e.g. DGRF-models) the reduction leads to errors, because of limited spatial resolution of these models. Korte [1999] gives the following error estimates of the measurements of the field components and the computed secular variation for European repeat surveys.

Ideally data for field modelling should not be reduced to observatory annual means, but rather to quiet night time. The data should be acquired as a mean of several measurements at different external conditions and separated by 24 hours in order to reduce the external contributions [Newitt et al., 1996].

The repeat survey data considered in this study are taken from a database maintained by the British Geological Survey (BGS)⁴. Only the data from repeat stations outside the

⁴<http://www.geomag.bgs.ac.uk/gifs/surveydata.html>

European mainland are incorporated. Certainly, the coverage and regular occupations of repeat stations across Europe are much better than in any other part of the world, but I would not expect any improvements in recovering the secular variation, as there already is a good coverage of observatories. Therefore, only repeat survey data are involved for regions, where the observatory density is sparse. The selection of repeat surveys will be listed below with a short description of the data.

Canada:

50 stations, of which nine were occupied more than 5 times, 23 visited four times.

United States including pacific islands:

61 stations, 5 more than 5 times, 7 more than 4 times

Columbia:

79 stations from which 13 were occupied 4 times between 1987 and 1995 and the rest at least twice in this period

Venezuela:

10 stations occupied twice in 1978 and years around 1983

Brazil:

78 stations, 19 of them were visited 4 times or more at an interval of about 5 years

Iceland, Norway, Finland, Portugal and Atlantic Islands:

3 Icelandic stations with 5 or more occupations

1 Norwegian station occupied once every year between 1991 and 1997

16 Finish stations visited up to six times in the period 1978.5 and 1986.5

7 Portuguese stations either on the Azores or on Madeira occupied up to three times during 1989 and 1991

2 stations in the south Atlantic (St. Helena and Ascension Island) which were visited three times.

Near East:

6 stations in Saudi Arabia visited twice, in 1980 and 1983

5 stations in Israel visited up to four times between 1992 and 1999

West and Central Africa:

26 stations were occupied in western and central Africa during 1986 and 1993

Southern Africa:

77 stations in southern Africa, 21 of them were visited five times or more during 1979 and 2000.

Japan and Indonesia:

3 Japanese station located not on the mainland

15 Indonesian sites.

Australia and New Zealand:

69 Australian stations, where 10 were occupied 5 or more times, and 4 stations were occupied four times.

45 stations in New Zealand, six four times and 30 five or more times.

Antarctic region:

14 Antarctic stations, from which seven were occupied five times or more and three visited four times.

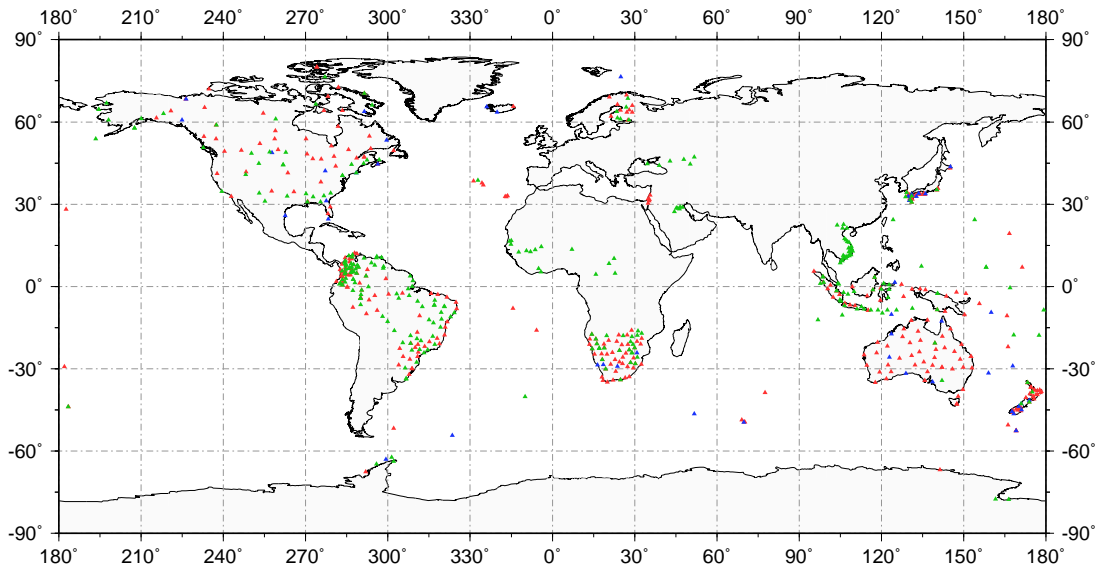


Figure 3.2: Global chart of repeat station, green triangles sites provided one secular variation estimate (SVE), red dots indicate sites of multiple visits, but less than 5 SVE, blue dots indicating sites with more than 4 SVE.

3.2 Data processing

In addition to internal field variation, ground based measurements are also subject to crustal fields and external field variations. Observatories and repeat station are fixed relative to crust and therefore the correlation in these data due to the crustal bias are in the temporal domain, as far as the spatial separation of observatories are comparable longer than the length scale of the crustal field.

Interference from external field variations show temporal as well as spatial correlation. Distinct features of these variations are the semi-annual and the annual signal, which are caused by the movement of the ring-current, a magnetospheric current system in 3–5 Earth radii distance, and the change of heliographic latitude of Earth's orbit.

Using first differences of the measurements – secular variation estimates – should eliminate

the contributions due to crustal biases. In the next section a simple approach is outlined, which reduces the crustal and external biases.

3.2.1 Secular variation estimates

Filtering of time series is always a delicate issue: On one side the applied filter removes essential information inherent in the data and on the other side it introduces artificial signals to the time series. The right balance of both effects is decisive to any conclusion one will draw from this research.

A simple method for removing seasonality, or periodicity, in the data with a period p is differencing in the way, that, if p is a multiple of the sampling interval one could choose to examine

$$C_t - C_{t-p}.$$

In the case, that p and t are not commensurable then using

$$C_t - (1 - \delta)C_{t-p} - \delta C_{t-n-1},$$

where $n = |p|$ and $\delta = p - n$, the periodicity can be largely removed [Conradsen & Spliid, 1981]. This approach is known as the *p-step difference filter* [Box & Jenkins, 1976; Priestley, 1981] and it is appropriate to derive a secular variation estimate from observatory monthly means with reducing the contribution of annual and semi-annual variations, e. g. for the northward component

$$dX/dt = X(t + n/2) - X(t - n/2), \quad n = 12 \quad (3.2)$$

Observatory annual means are treated using, e. g.

$$dX/dt = X(t) - X(t - 1). \quad (3.3)$$

This also reduces the crustal bias, because the crustal signal is assumed to be the same for both dates t and $t - 1$ and therefore should cancel.

3.3 Some fundamental concepts of Inverse Problems

3.3.1 Statement of the forward problem and inverse problem

Any inverse problem is intertwined with its related forward problem which in general can be stated as

$$y = F(\mathbf{x}) \quad (3.4)$$

where F is a integral operator, which is in general nonlinear, y is the observation, e.g. the observed magnetic field at Earth's surface, and \mathbf{x} denotes the vector of the unknown magnetic field at the core-mantle boundary (CMB). The approach for the determination of the magnetic field at the CMB consists then in either:

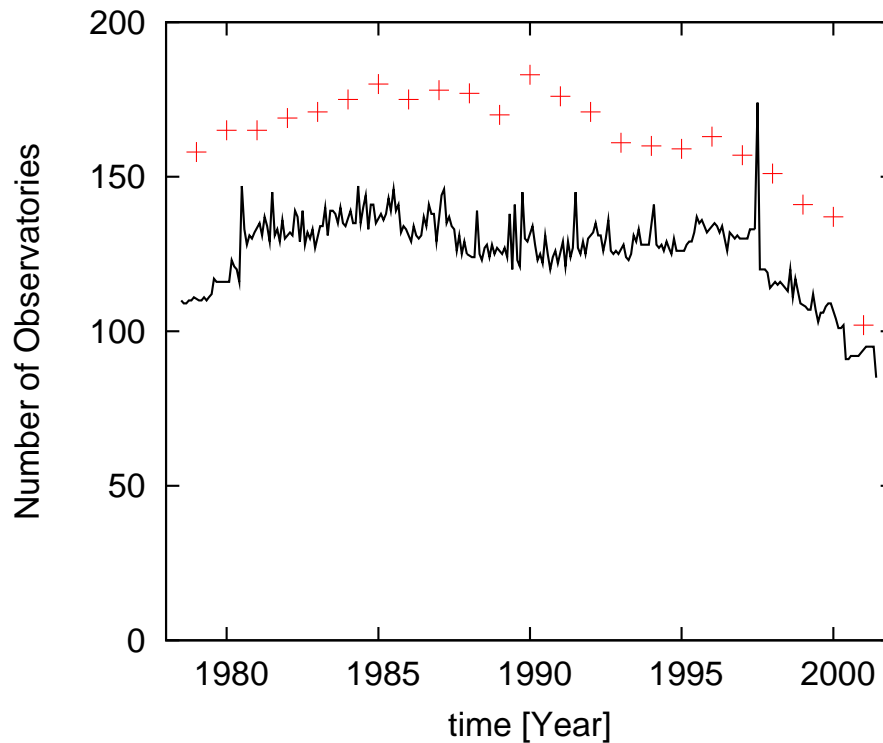


Figure 3.3: The number of available annual secular variation estimates shown as red crosses and the number of monthly secular variation estimates (either based on observatory or repeat station measurements) shown as solid black curve.

- a) The repeated forward solving of (3.4) for a trial- and error model x until the observation y is satisfied.
- b) The inversion of (3.4) to infer x directly from y .

While forward modelling provides one particular model which fits the observed data, inversion usually allows one to explore the whole model space and to delimit a range of possible models, which fit the data within its experimental and observational error interval equally well.

The inverse solution of (3.4) can be formally written as

$$x = F^{-1}(y). \quad (3.5)$$

where F^{-1} is the inverse operator of F .

There are three issues related to the problem of finding the solution of (3.5):

- 1) **Existence of a solution** or of the inverse operator F^{-1} . This is a fundamental problem in the theoretical analysis of inverse problems. However, it is of minor

importance for the solution of geophysical inverse problems where an inverse operator can generally be computed by some discrete numerical technique.

2) **Uniqueness of the solution** holds if, and only if the operator F is injective, i.e.

$$y_1 = y_2 \Rightarrow x_1 = x_2. \quad (3.6)$$

As Backus & Gilbert [1967, 1968]; Backus [1970] pointed out, geophysical inverse problems are inherently non-unique as a consequence of the a priori infinite dimensionality of the model space. Therefore, with only finite data, the model cannot be uniquely determined.

3) **Stability of the solution** questioned how small fluctuation in the data y propagate into changes in the model x . The inverse solution is to be said stable if, for two sufficiently close data sets y, y' and two corresponding models x, x' it is

$$|y - y'| \leq \varepsilon \Rightarrow |x - x'| \leq d(\varepsilon). \quad (3.7)$$

An inverse problem which does not satisfy condition 2 and 3 is called an ill-posed inverse problem as opposed to a well-posed inverse problem. To gain a well-posed inverse problem several regularization techniques have been introduced and developed in the past decades, such as Tikhonov regularization, Least squares collocation, Bayes-estimation and Backus-Gilbert formalism [Parker, 1994; Backus & Gilbert, 1967, 1968; Backus, 1970].

3.4 Method

From now the inverse problem is considered to be linear: either linearized using Fermat's principle, or linear by nature, then the linear system of equation is given:

$$y = \mathbf{A}m + e. \quad (3.8)$$

This is the equation of condition, where \mathbf{A} is a design matrix mapping the model vector m to the data y , and e is the error vector.

3.4.1 The least-squares estimator

The classical approach to solve linear inverse problems such as (3.8) is based on measures of the distance of modeled or predicted conditions $y^{mod} = \mathbf{A}m + e$ and data y as,

$$e = y - y^{mod} = y - \mathbf{A}m \quad (3.9)$$

$$\|e\|^2 = e^T e = (y - \mathbf{A}m)^T (y - \mathbf{A}m) \quad (3.10)$$

The aim of utilizing this method is to gain a model where the predicted data are as close as possible to the observed data, so the misfit $\|e\|^2$ is minimal. Assuming that the matrix

\mathbf{A} has full column rank $p = m$ and that $m < n$, the condition for $\|\mathbf{e}\|^2$ to be a minimum follows:

$$\mathbf{A}^\top(\mathbf{y} - \mathbf{A}\mathbf{m}) = 0, \quad (3.11)$$

which is equivalent to the normal equations

$$\mathbf{A}^\top \mathbf{A} \mathbf{m} = \mathbf{A}^\top \mathbf{y}. \quad (3.12)$$

This gives the formal solution, which exists since $p = m$

$$\mathbf{m} = (\mathbf{A}^\top \mathbf{A})^{-1} \mathbf{A}^\top \mathbf{y}. \quad (3.13)$$

This solution is the maximum likelihood; here, it is tacitly assumed the error in (3.8) are additive, independent and to be normal distributed with expectation $E(\mathbf{e}) = 0$ and standard deviation $\sigma^2 = 1$. If on the other hand the errors have a non-uniform variance, then (3.13) reads

$$\mathbf{m} = (\mathbf{A}^\top \mathbf{C}_e^{-1} \mathbf{A})^{-1} \mathbf{C}_e^{-1} \mathbf{A}^\top \mathbf{y}, \quad (3.14)$$

where \mathbf{C}_e^{-1} is the error covariance matrix.

In case of an ill-posed inverse problem, evaluations of the least-squares solution (3.13) by any numerical technique, such as Gaussian elimination, Single Value- or Cholesky decomposition give solutions \mathbf{m} and covariances of the model parameter \mathbf{C}_m , which are oscillating and large. In the next section I will discuss the origins and consequences of an ill-posed problem, and the general methodology of regularization.

3.4.2 Regularization of ill-posed inverse problem

If the third of the requirements in section 3.1.1 is not fulfilled, then the inverse problem is called ill-posed. As pointed out in the previous section, a solution of the inverse problem can generally be computed. Now the question is, how does the solution depend on the data? We need to quantify the criterion (3.7) for the stability of the solution and how variations of the data map into the model. To quantify the stability of solutions of a set of linear equations, we estimate the total error of the solutions

$$\|\mathbf{m} - \mathbf{m}_\delta\| \leq \|\mathbf{A}^{-1}\| \|\mathbf{y} - \mathbf{y}_\delta\|, \quad (3.15)$$

where \mathbf{m}_δ and \mathbf{y}_δ are estimates of the vectors \mathbf{m} and \mathbf{y} , respectively. Furthermore, $\mathbf{m}_\delta = \mathbf{A}^{-1} \mathbf{y}_\delta$. Lawson & Hanson [1974] obtain the following conservative bound

$$\frac{\|\mathbf{m} - \mathbf{m}_\delta\|}{\|\mathbf{m}\|} < \kappa(\mathbf{A}) \frac{\|\mathbf{y} - \mathbf{y}_\delta\|}{\|\mathbf{y}\|}, \quad (3.16)$$

where $\kappa(\mathbf{A})$ is the so called condition number of the matrix \mathbf{A} defined as

$$\kappa(\mathbf{A}) = \|\mathbf{A}\| \|\mathbf{A}^{-1}\| = \frac{\max |s_i|}{\min |s_i|}, \quad (3.17)$$

s_i are the singular values of the matrix \mathbf{A} computed using the singular value decomposition.

It follows that the solution will be unstable if $\kappa(\mathbf{A}) \gg 1$. Beside numerical round-off errors, the instability of the solutions are also caused by partly collinearity of columns and/or rows. This occurs when the data coverage is insufficient.

Stochastic inversion

I now discuss regularization methods to stabilize the solution of an ill-posed inverse problem. The technique treated here is the stochastic inversion. It is set up to reduce the covariances of the model parameters by invoking objective a priori information of the likeness of the sought solutions. The method was developed by Wiener [1949] and introduced to geophysics by Franklin [1970]. Now consider a linear system (3.8)

$$\mathbf{y} = \mathbf{A}\mathbf{m} + \mathbf{e},$$

where \mathbf{m} and \mathbf{e} are stochastic processes with zero means. The auto- and cross-covariance matrices are given by

$$\mathbf{C}_m = E[\mathbf{m}\mathbf{m}^T], \quad (3.18)$$

$$\mathbf{C}_y = E[\mathbf{y}\mathbf{y}^T], \quad (3.18b)$$

$$\mathbf{C}_e = E[\mathbf{e}\mathbf{e}^T], \quad (3.18c)$$

$$\mathbf{C}_{my} = E[\mathbf{m}\mathbf{y}^T]. \quad (3.18d)$$

The objective of stochastic inversion is then to find an inverse matrix \mathbf{H} of \mathbf{A} , such that the covariance of the true error

$$E[\mathbf{e}_m \mathbf{e}_m^T] = E[(\mathbf{m} - \hat{\mathbf{m}})(\mathbf{m} - \hat{\mathbf{m}})^T] \rightarrow \text{minimum} \quad (3.19)$$

with

$$\hat{\mathbf{m}} = \mathbf{H}\mathbf{y}, \quad (3.20)$$

where \mathbf{H} is a $m \times n$ matrix such that the estimate $\hat{\mathbf{m}}$ is a stable average of the data with a meaningful physical interpretation [Jackson, 1979]. Combining (3.20) and (3.8) gives

$$\begin{aligned} \hat{\mathbf{m}} &= \mathbf{H}\mathbf{A}\mathbf{m} + \mathbf{H}\mathbf{e} \\ &= \mathbf{R}\mathbf{m} + \mathbf{H}\mathbf{e}. \end{aligned} \quad (3.21)$$

By definition it is $\mathbf{R} = \mathbf{H}\mathbf{A}$.

Following Jackson [1979] and Gubbins [1983] leads to an expression for the optimal \mathbf{H}

$$\begin{aligned} \mathbf{H}_{opt} &= \mathbf{C}_{my} \mathbf{C}_y^{-1} \\ &= (\mathbf{A}^T \mathbf{C}_e^{-1} \mathbf{A} + \mathbf{C}_m^{-1})^{-1} \mathbf{A}^T \mathbf{C}_e^{-1}. \end{aligned} \quad (3.22)$$

The final solution is given by

$$\mathbf{m} = (\mathbf{A}^T \mathbf{A} + k\mathbf{I})^{-1} \mathbf{A}^T \mathbf{y} \quad (3.23)$$

or more generally

$$\mathbf{m} = (\mathbf{A}^T \mathbf{C}_e^{-1} \mathbf{A} + \mathbf{C}_m)^{-1} \mathbf{A}^T \mathbf{C}_e^{-1} \mathbf{y} \quad (3.24)$$

where $k = \sigma_y^2/\sigma_m^2$ is a constant and \mathbf{I} the identity matrix. (3.24) follows directly from the assumption, that \mathbf{m} and \mathbf{e} are stochastic processes with zero means and variances $\mathbf{C}_e = \sigma_y^2\mathbf{I}$ and $\mathbf{C}_m = \sigma_m^2\mathbf{I}$. This method is exactly the damped least-squares method, here one adds white noise to the diagonal matrix elements of the normal matrix $\mathbf{A}^\top\mathbf{A}$ to stabilize the solution of the ill-posed inverse problem. The model vector \mathbf{m} estimated by (3.24) minimizes the objective function [Bloxham, 1987]

$$\Theta(\mathbf{m}) = (\mathbf{y} - \mathbf{A}\mathbf{m})^\top\mathbf{C}_e^{-1}(\mathbf{y} - \mathbf{A}\mathbf{m}) + \mathbf{m}^\top\mathbf{C}_m^{-1}\mathbf{m}. \quad (3.25)$$

3.4.3 Application to geomagnetic data

Now, after some theoretical discussions of solving ill-posed inverse problems, I want to apply these methods to develop a time-dependent model of the geomagnetic field and its secular variation between 1980 and 2000. But before, I would like to point out that the previous consideration are needed to model the geomagnetic field. The formalism, which is developed in this section, is based on an approach of Bloxham & Jackson [1992].

The Earth's magnetic field can be represented as a potential field as it is in an electrical insulator $\mathbf{B} = -\nabla V$, where V is a scalar potential field. The potential field has to satisfy the Laplace equation $\nabla^2 V = 0$, so the solution in spherical geometry reads:

$$V = a \sum_{l=1}^{\infty} \sum_{m=0}^l \left\{ (g_l^m \cos(m\phi) + h_l^m \sin(m\phi)) \left(\frac{a}{r}\right)^{l+1} P_l^m(\cos\theta) + (q_l^m \cos(m\phi) + s_l^m \sin(m\phi)) \left(\frac{r}{a}\right)^l P_l^m(\cos\theta) \right\}, \quad (3.26)$$

where a is the Earth's radius (6371.2 km) and (r, θ, ϕ) the geocentric coordinates, θ the colatitude. The $P_l^m(\cos\theta)$ are the Schmidt normalized associated Legendre functions

$$\int_{\phi=0}^{2\pi} \int_{\theta=0}^{\pi} (P_l^m(\cos\theta) \cos(m\phi))^2 \sin\theta \, d\theta \, d\phi = \frac{4\pi}{2l+1}, \quad (3.27)$$

where l are the degrees and m the order. The coefficients $\{g_l^m, h_l^m\}$ and $\{q_l^m, s_l^m\}$ are the Gauss coefficients.

$$V_{int} = a \sum_{l=1}^{\infty} \sum_{m=0}^l \left(\frac{a}{r}\right)^{l+1} [g_l^m \cos(m\phi) + h_l^m \sin(m\phi)] P_l^m(\cos\theta) \quad (3.28)$$

$$V_{ext} = a \sum_{l=1}^{\infty} \sum_{m=0}^l \left(\frac{r}{a}\right)^l [q_l^m \cos(m\phi) + s_l^m \sin(m\phi)] P_l^m(\cos\theta).$$

The potential equation consists of two parts; terms in $(a/r)^{l+1}$ to describe the internal potential or field V_{int} , which vanish at infinity and terms in $(r/a)^l$ to describe fields with external origin with respect to the Earth's surface V_{ext} , which must remain finite within a volume of interest [Langel, 1987].

Basically, the method here relies on the evaluation of the geomagnetic potential at the core–mantle boundary, derived from quantities measured at the Earth’s surface. The problem is ill-posed due to the fact that the geomagnetic potential is not known entirely at Earth’s surface. In practice the expansion of (3.26) is truncated at a certain level, and therefore the geomagnetic potential is unknown from that level onward. Formally, there are infinite (truncated) description of the potential at the core–mantle boundary, which would describe the observed geomagnetic field at Earth’s surface. One assumption which may help here, is to declare any Gauss coefficient greater than the truncation level as equal to zero. One other approach is developed in the following.

The Gauss coefficients are expanded in time as spline functions $S(\xi)$

$$g_l^m(t) = S(\xi) \quad (3.29)$$

and likewise for $h_l^m(t)$.

The (natural) spline functions $S(\xi)$ is a linear combination of B(asis)–spline functions

$$S(\xi) = \sum_{j=-1}^{n+1} a_j B_{j,k}(\xi), \quad (3.30)$$

in which a_j are the spline coefficients (g_l^{mj}) and $B_{j,k}(\xi)$ are the piecewise polynomial functions of order k and degree $(k - 1)$. For $k = 4$ these polynomials are cubics. Unlike other polynomial functions (e.g. Legendre), which are defined on the whole interval $[t_1, t_j]$, a single B–spline function is defined very locally.

A set of non–decreasing real numbers $t_0 \leq t_1 \leq \dots \leq t_j$ are called the knots, the knot points and the half–open interval $[t_i, t_{i+1})$ is called the knot span. The knots can be considered as division points that subdivide the interval $[t_1, t_j]$ into $n + 2$ knot spans. Generally, the i –th B–spline of degree k is defined recursively by the Cox–DeBoor formula

$$B_{i,1} = \begin{cases} 1 & t_i \leq \xi < t_{i+1}, \\ 0 & \text{otherwise} \end{cases} \quad (3.31)$$

and for $k \geq 1$

$$B_{i,k}(\xi) = \frac{\xi - t_i}{t_{i+k-1} - t_i} B_{i,k-1}(\xi) + \frac{t_{i+k} - \xi}{t_{i+k} - t_{i+1}} B_{i+1,k-1}(\xi) \quad (3.32)$$

The B–splines are for $k = 2$ piecewise linear, for $k = 3$ piecewise quadratic, for $k = 4$ piecewise cubic, and so on. In particular for cubic B–splines with equidistant knots it follows

$$B_{i,4}(\xi) = \begin{cases} 1/6z^3 & t_{i-2} < \xi < t_{i-1}, \\ 1/6[1 + 3(1 + z(1 - z))z] & t_{i-1} \leq \xi < t_i, \\ 1/6[1 + 3(1 + z(1 - z))(1 - z)] & t_i \leq \xi < t_{i+1}, \\ 1/6(1 - z)^3 & t_{i+1} \leq \xi < t_{i+2}, \\ 0 & \text{otherwise,} \end{cases} \quad (3.33)$$

where d is the distance between the knots (e.g. $d = t_{i+1} - t_i$) and z the distance between the t_{i+k} and ξ divided by d (e.g. $z = (\xi - t_{i+2})/d$). Within the i -th knot span only k B-splines $B_{i-k+1}, \dots, B_{i,k}$ are non-zero and normalized to 1. Also note, that the B-spline is symmetric about the knot around which it is centered.

The motivation of using splines is mainly because of three reasons:

1. basis functions are non-zero on a few adjacent subintervals, therefore ideal for recovering very localized features, i. e. temporal discontinuities,
2. the spline curve $S(\xi)$ has a minimum curvature in the interval $[t_1, t_j]$,
3. the banded form of the normal equation matrix makes large problems feasible for given computational power, what is the most important reason.

In matrix form (3.30) reads

$$S = \mathbf{A} \cdot \mathbf{x}, \quad (3.34)$$

where the vector \mathbf{x} contains the spline coefficients a_j . \mathbf{A} is symmetric and positive definite, and therefore nonsingular⁵. Cholesky decomposition is commonly used to solve linear systems equations with this matrix \mathbf{A} ; it is a special case of the LU-decomposition. These decompositions are based on the following considerations: a symmetric and positive definite matrix \mathbf{A} can be formulated as

$$\mathbf{A} = \mathbf{L}\mathbf{U}, \quad (3.35)$$

\mathbf{L} and \mathbf{U} are quadratic matrices, where for the upper matrix \mathbf{U} all elements below the diagonal are equal to zero

$$\mathbf{U}_{ij} = 0 \text{ for } i > j \quad \mathbf{U} = \begin{pmatrix} U_{11} & U_{12} & U_{13} & \dots & U_{1n} \\ & U_{22} & U_{23} & \dots & U_{2n} \\ & & U_{33} & \dots & U_{3n} \\ & & & \ddots & \\ & & & & U_{nn} \end{pmatrix} \quad (3.36)$$

whereas for the lower matrix \mathbf{L} all elements above the diagonal are equal to zero

$$\mathbf{L}_{ij} = 0 \text{ for } i < j \quad \mathbf{L} = \begin{pmatrix} L_{11} & & & & \\ L_{21} & L_{22} & & & \\ L_{31} & L_{32} & L_{33} & & \\ \vdots & & & \ddots & \\ L_{n1} & L_{n2} & L_{n3} & \dots & L_{nn} \end{pmatrix} \quad (3.37)$$

Equation (3.34) can then be written as

$$\mathbf{A} \cdot \mathbf{x} = \mathbf{L} \cdot (\mathbf{U} \cdot \mathbf{x}) = S, \quad (3.38)$$

⁵ \mathbf{A} becomes positive definite, when appropriate regularization is applied, which shifts zero eigenvalues by the value of damping

and solving for x takes two steps, first by solving the intermediate vector y

$$\mathbf{L} \cdot y = b \quad (3.39)$$

and then solving (backward substitution)

$$\mathbf{U} \cdot x = y. \quad (3.40)$$

The forward substitution of (3.39) reads

$$\begin{aligned} y_1 &= \frac{b_1}{L_{11}} \\ y_i &= \frac{b_i - \sum_{j=1}^{i-1} L_{ij} y_j}{L_{ii}} \quad i = 2, \dots, n \end{aligned} \quad (3.41)$$

and the backward substitution

$$\begin{aligned} x_n &= \frac{y_n}{U_{nn}} \\ x_i &= \frac{y_i - \sum_{j=i+1}^n U_{ij} x_j}{U_{ii}} \quad i = n-1, n-2, \dots, 1. \end{aligned} \quad (3.42)$$

The Cholesky decomposition takes advantage of the fact that if $\mathbf{A} = \mathbf{A}^T$ then (3.35) is

$$\mathbf{A} = \mathbf{U}^T \mathbf{U}, \quad (3.43)$$

i. e. upper and lower triangular matrices are the same and the forward and backward substitution read

$$\begin{aligned} y_1 &= \frac{b_1}{U_{11}^T} \\ y_i &= \frac{b_i - \sum_{j=1}^{i-1} U_{ij}^T y_j}{U_i^T i} \quad i = 2, \dots, n \\ x_n &= \frac{y_n}{U_{nn}} \\ x_i &= \frac{y_i - \sum_{j=i+1}^n U_{ij} x_j}{U_i i} \quad i = n-1, n-2, \dots, 1. \end{aligned} \quad (3.44)$$

Utilizing the method of stochastic inversion to construct solutions to the simultaneous inverse problem requires minimizing (3.25). In fact it means minimizing of the misfit between model and observation and a model norm $\mathbf{m}^T \mathbf{C}_m^{-1} \mathbf{m}$. \mathbf{C}_m is chosen to reflect the spatial and temporal a priori variance in the field at the CMB.

One source of prior information about \mathbf{B}_r at the CMB is the heat flux bound Q , derived from the Maxwell equations and Ohm's law. Gubbins [1975] analysis leads to the condition

$$F(\mathbf{B}_r) = \sum_{l=1}^{\infty} \frac{(l+1)(2l+1)(2l+3)}{l} \sum_{m=0}^l [(g_l^m)^2 + (h_l^m)^2] \leq Q \quad \text{for } r = c, \quad (3.45)$$

where the heat flux bound is given by

$$Q = \Upsilon \frac{\kappa \mu_0^2}{4\pi c}, \quad (3.46)$$

with Υ the rate of the ohmic heat production of the core, κ the maximum electrical conductivity in the core, and μ_0 the magnetic permeability of vacuum. Taking $\kappa = 3 \times 10^5 \text{Sm}^{-1}$, $c = 3.48 \times 10^6 \text{m}$, $\mu_0 = 4\pi \times 10^{-7} \text{NA}^{-2}$ and $\Upsilon = 3 \times 10^{13} \text{W}$ (the observed heat flow out of the Earth's surface) gives

$$Q = 3 \times 10^{17} \text{nT}^2. \quad (3.47)$$

However this value of Q may vary between 3×10^{16} and $3 \times 10^{18} \text{nT}^2$ depending on Υ^6 , but it should give an upper limit.

The spatial regularization condition is then

$$S = \frac{4\pi}{(t_2 - t_1)} \int_{t_1}^{t_2} F(\mathbf{B}_r) dt = \mathbf{m}^T N_S^{-1} \mathbf{m} \leq Q. \quad (3.48)$$

The condition to adjust the temporal behaviour of the solution, one seeks to minimize the norm

$$T = \frac{1}{(t_2 - t_1)} \int_{t_1}^{t_2} \oint_{CMB} (\partial \mathbf{B}_r / \partial t)^2 dS dt = \mathbf{m}^T N_T^{-1} \mathbf{m}, \quad (3.49)$$

with

$$\oint_{CMB} (\partial \mathbf{B}_r / \partial t)^2 dS = \sum_{l=1}^{\infty} (l+1) \left(\frac{a}{c}\right)^{2l+4} \sum_{m=0}^l [(\dot{g}_l^m)^2 + (\dot{h}_l^m)^2] \quad (3.50)$$

Finally the regularization condition is given by

$$\mathbf{C}_m^{-1} = \lambda_s N_S^{-1} + \lambda_t N_T^{-1}, \quad (3.51)$$

whith the damping parameters λ_s and λ_t [c.f. Bloxham & Jackson, 1992]. Other possible regularization conditions are listed in table (3.3).

3.4.4 Extension of the Bloxham–Jackson formalism

The essential new aspect of this study is the invoking of a priori information for the geomagnetic field at the endpoints of the time interval 1980 and 2000.

$$\Theta(m) = (\mathbf{y} - \mathbf{A}\mathbf{m})^T \mathbf{C}_e^{-1} (\mathbf{y} - \mathbf{A}\mathbf{m}) + \mathbf{m}^T \mathbf{C}_m^{-1} \mathbf{m} + \mathbf{C}_a^{-1}. \quad (3.52)$$

⁶For simplicity, here is assumed that the heat flux out of the core is equal to that, which is observed at the Earth's surface. In fact, the largest portion of the heat flux comes from the crust. Labrosse [2002] gives estimates of the heat flux of the core ranging from $2 \times 10^{12} \text{W}$ to $10 \times 10^{12} \text{W}$.

integral to minimize	Norm function $f(r_0, l)$	Comments
(a) $\oint \mathbf{B}^2 dS _{r=r_0}$	$(l+1) \left(\frac{a}{r_0}\right)^{(2l+4)}$	Mean square field intensity
(b) $\oint \mathbf{B}_r^2 dS _{r=r_0}$	$\frac{(l+1)^2}{2l+1} \left(\frac{a}{r_0}\right)^{(2l+4)}$	Mean square radial field
(c) $\oint (\nabla_h \mathbf{B}_r)^2 dS _{r=r_0}$	$\frac{l(l+1)^3}{2l+1} \left(\frac{a}{r_0}\right)^{(2l+6)}$	Mean square of horizontal derivative of radial field

Table 3.2: Smoothing norms for magnetic field inversion after Holme & Bloxham [1996].

The magnetic field is constrained by models derived from high-quality satellite vector data \mathbf{m}_0^{1980} and \mathbf{m}_0^{2000} , respectively. The a priori model regularization condition is then

$$\begin{aligned} \oint \mathbf{B}^2 dS|_{t=1980} &= (\mathbf{m} - \mathbf{m}_0^{1980})^\top N_1^{-1} (\mathbf{m} - \mathbf{m}_0^{1980}) \\ \oint \mathbf{B}^2 dS|_{t=2000} &= (\mathbf{m} - \mathbf{m}_0^{2000})^\top N_2^{-1} (\mathbf{m} - \mathbf{m}_0^{2000}) \end{aligned} \quad (3.53)$$

giving

$$\mathbf{C}_a^{-1} = \lambda_1 N_1^{-1} + \lambda_2 N_2^{-1}. \quad (3.54)$$

The advantage of using satellite based models is their higher spatial resolution of the magnetic field. At the endpoints the time-dependent field model is constrained by a priori field models in 1980 and 2000 [Cain et al., 1989; Olsen, 2002]. These models are constructed by tapering single epoch models from satellite data. The taper is defined by the minimization conditions

$$(\mathbf{B} - \mathbf{B}_0)^2 \quad (3.55)$$

at the Earth's surface where \mathbf{B}_0 is the MAGSAT or ØRSTED model including crustal field, respectively. But also minimise

$$(\mathbf{B})^2 \quad (3.56)$$

at the CMB. Integration over the Earth's surface leaves to minimize

$$\sum_{l,m} (l+1) ((g_l^m - g_{l0}^m)^2 + (h_l^m - h_{l0}^m)^2) + \lambda (l+1) \left(\frac{a}{c}\right)^{(2l+4)} ((g_l^m)^2 + (h_l^m)^2), \quad (3.57)$$

where λ is a Lagrange multiplier. Differentiating with respect to the Gauss coefficients, setting each differential to zero, and rearranging, this gives

$$g_l^m = \frac{g_{l0}^m}{1 + \lambda \left(\frac{a}{c}\right)^{(2l+4)}}. \quad (3.58)$$

The high-degree coefficients are damped much more than the low degree ones. The degree of fall-off is obviously controlled by λ .

3.4.5 Modelling and selection of damping parameter

The modelling is undertaken in an iteratively re-weighting scheme comprising four steps:

1. A first guess model is computed weighting all data with the same uncertainty (5 nT).
2. The second step is to derive the deviations of the data from the first guess model to compute new weights for the data. Data, which scatter extremely from the model are down-weighted.
3. Now a model is derived from the newly (re-) weighted data set.
4. In the final step, data are discarded which deviates more than 2σ from the second model. From this reduced data set the final model is derived.

Models were derived for ranges of temporal damping parameters $3.5 \cdot 10^2 \leq \lambda_t \leq 3.5 \cdot 10^{-5}$. In order to choose an appropriate damping the objective function (3.52) might be transformed into

$$F(\kappa) = E + \kappa N, \quad (3.59)$$

where E is the misfit and N the solution norm. κ is a positive parameter which determines the relative importance of E and N . There are two extremal situations 1.) $\kappa = 0$, a priori information of the model are neglected 2.) $\kappa = \infty$, the data are ignored completely and the minimized norm gives $m = 0$. Therefore minimizing $F(\kappa)$ is a compromise between these extrema. A satisfying solution can be read from a plot E versus N .

The selection of the spatial damping parameter is founded by an a priori knowledge of core physics, which is independent of the data set inverted. The condition (3.45) assigns to a sequence of Gauss coefficients in the model space the probability distribution which has a zero mean and the variance

$$\langle |g_l^m(c)|^2 \rangle = Ql(l+1)^{-1}(2l+1)^{-1}(2l+3)^{-1}. \quad (3.60)$$

This limits each Gauss coefficient only by requiring it not to produce by itself more ohmic heat in the core than is observed in the surface heat flow [Backus, 1988]. Following Backus [1988] gives a

$$\lambda_s = 8 \times 10^{-17} \text{nT}^2$$

with $Q = 3 \times 10^{18} \text{nT}^2$. This Bayesian approach facilitates error estimates and to quantify the range of permissible models (see section 3.5.4). The solution for unchanged λ_s will be that where the trade-off curve has its knee. Figures (3.4) show the three trade-off curves of the temporal norm vs misfit for the three different values of departure damping. The damping controlling the departure from the a priori models is chosen in the way that the endpoint models for 1980.0 and 2000.0 are identical with the satellite main field models.

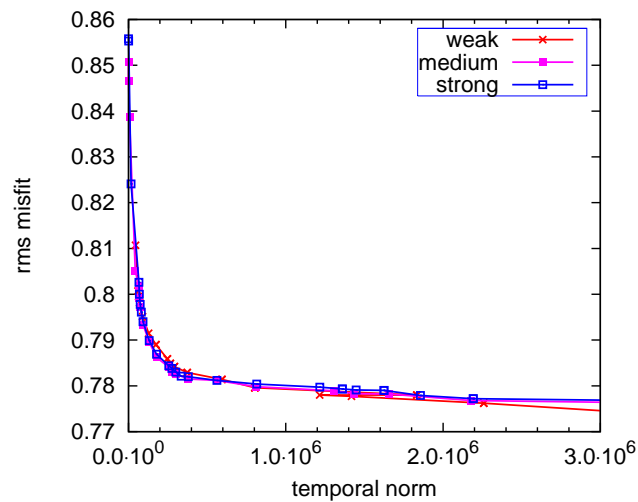


Figure 3.4: Trade-off curves of the temporal norm vs. misfit for different spatial damping weak: $\lambda_{\Gamma} = 4.0 \cdot 10^1$, medium: $\lambda_{\Gamma} = 4.0 \cdot 10^3$ and strong: $\lambda_{\Gamma} = 4.0 \cdot 10^6$.

Treating this constraint strongly obliges the degrees 10 to 14 of the main field for an epoch in between (i. e. 1991) to have significant information. Figure (3.5) shows power spectra of main fields for the epochs 1980, 1991 and 2000 and also for the main field models derived from MAGSAT or ØRSTED satellite data, respectively. Here the departure constraint is relaxed, the power spectrum for the 1991 main field model falls off at order 10. What means that the spectrum from this degree onward is comparable with those of a white noise process, where the Gauss coefficients behave erratically. Figure (3.6) shows when the departure constraint is applied strongly and the spectrum of the main field model for 1991 tends to fall off around degree 14.

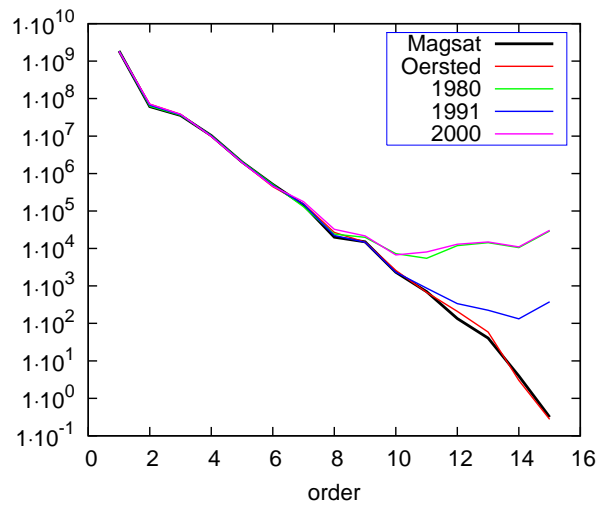


Figure 3.5: Spectra of main field of a time-dependent model for three different times 1980, 1991 and 2000 in comparison with the satellite main field models from MAGSAT and ØRSTED. The departure damping is chosen to be weak ($\lambda_{\Gamma} = 6.0 \cdot 10^{-1}$).

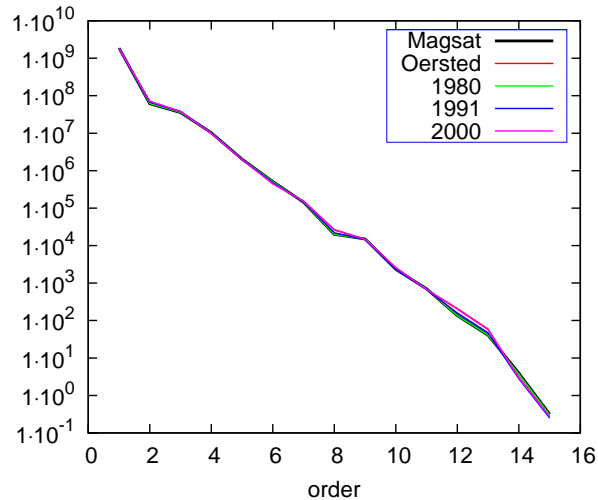


Figure 3.6: Spectra of main field of the preferred time-dependent model for three different times (1980, 1990 and 2000), where the departure damping is chosen to be strong ($\lambda_{\Gamma} = 6.0 \cdot 10^6$) in comparison with the satellite main field models from MAGSAT and ØRSTED.

Statistics	
Number of data	70939
Number of Splines	13
Damping	
spatial λ_s	0.3×10^{-17}
temporal λ_t	0.3×10^{-3}
departure λ_Γ 1980.0	0.60×10^3
departure λ_Γ 2000.0	0.60×10^3
Model norms	
spatial	3.56×10^8
temporal	3.69×10^5
departure	1.93×10^9
RMS Residual	0.782

Table 3.3: Statistics and parameters of the time-dependent modelling

3.5 Results

In the previous section I developed a time-dependent model of the main field and its secular variation for the period 1980 - 2000. The results of the time-depending modelling have been achieved under the assumption that the mantle is an insulator, except for possibly at its base, where a 200 km thick layer exists, known as D''. This layer is likely to be a boundary layer chemically and physically distinct from the rest of mantle. If this layer is conducting, then it would have only a little effect on the results of the downward continuation. In fact Voorhies [2000] could show that the core radius inferred from seismic methods differ by only 62 km from that of geomagnetic estimates. However, a conductivity jump across the CMB is expected, what causes that the horizontal components are discontinuous there. The radial component remains continuous. Therefore, in the next sections only results of the preferred model solution for the radial component of the magnetic field and secular variation are discussed.

3.5.1 Morphology of the magnetic field at the core-mantle boundary

In figure (3.7) the radial component of the magnetic field is shown for 5 epochs 1980.0, 1985.0, 1990.0, 1995.0 and 2000.0. The maps show basically a dipolar structure which is riddled with localized concentrations of high flux separated by larger areas of weaker flux. All features are apparently equally present in all maps.

In order to characterize the features a similar nomenclature as in Bloxham et al. [1989] is applied. Regions of high field are marked as N (normal) and R (reversed). The term reversed means here that these patches have a reverse flux with respect to their vicinity and are bounded by a null-flux curve. See for locations of these features figure (3.8). Bloxham et al. [1989] found in their analysis that patches have drifted by as much as 60° in longitude over a period of 265 years. This rate might be detected for some of the R patches. Table 3.4 lists the positions, size and the flux through the R patches.

The most prominent such feature is the patch R2 beneath the southern Atlantic. This dog-bone shaped patch with reversed flux (with respect to its surroundings) has grown continuously since it appeared around 1970 [Jackson et al., 2000]. In 1984 the patch merged with a minor patch R1 underneath Antarctica and finally united with the major positive flux pattern of the northern hemisphere in 1997. The size, position and flux of the other reversed flux patches of the southern hemisphere remained almost unchanged during this period. There are also reversed flux patches in the north polar region. Initially a single patch R8 existed, which split into two individual patches R8A and R8B in 1986.

It should be mentioned that some of the high flux patches remained steady over the last 20 years namely N1 and N2 in the southern and N9 and N10 in northern hemisphere. Certainly the period is too short to infer anything definitively, but as pointed out by Bloxham et al. [1989] these patches remained steady over the last 300 years and were unaffected by the westward drift, which should have shifted these by about 60° . This fact strongly suggests that these features are linked to a steady dynamo process and are

Patch	Year	Long.	Lat.	Flux [MWb]	$\langle B_r \rangle$ [nT]	Area [km ²]
R1	1980	53.042	-78.746	45.8	81650.4	1.8×10^{12}
	2000	–	–	–	–	–
R2	1980	345.940	-46.246	603.3	137814.3	14.6×10^{12}
	2000	–	–	–	–	–
R3	1980	344.833	-19.600	77.5	80684.6	3.2×10^{12}
	2000	341.263	-20.136	119.4	110936.9	3.5×10^{12}
R4	1980	241.259	-18.106	20.7	34081.6	2.0×10^{12}
	2000	240.895	-17.555	19.3	35121.4	1.8×10^{12}
R5	1980	165.165	19.727	46.1	60198.2	2.5×10^{12}
	2000	165.076	20.109	40.2	56636.3	2.3×10^{12}
R6	1980	316.803	25.524	10.9	34746.5	1.0×10^{12}
	2000	313.089	25.090	6.2	24390.6	0.8×10^{12}
R7	1980	188.700	44.285	16.1	28328.0	1.8×10^{12}
	2000	190.656	45.029	30.8	42026.2	2.4×10^{12}
R8	1980	317.882	80.531	34.9	46351.6	2.5×10^{12}
R8A	2000	31.141	71.053	13.0	32394.2	1.3×10^{12}
R8B	2000	258.085	83.815	65.6	71798.9	3.0×10^{12}

Table 3.4: Listing of individual reverse flux patches for the epochs 1980 and 2000

most likely convection columns along 120° longitude west and 120° longitude east. These columns originally postulated by Busse [1970], are aligned parallel with the rotation axis of the Earth and touch the inner core at the equator. There are substantiated arguments that a well-ordered arrangement of columnar vortices with helical velocity distribution exists in a highly conducting liquid core. This idea has been proven convincingly by model experiments of Carrigan & Busse [1983]. However, there are also arguments against this flow pattern, which basically rely on the fact that these rolls collapse, when the Lorentz force act on [Fearn, 1998]. That might be a reason, why a third column, which was expected on grounds of geometrical reasons [Gubbins & Bloxham, 1987] is not traceable.

Testing the frozen flux hypothesis

The hypothesis that the secular variation on short time scales is entirely given by the advection term of the induction equation is known as the frozen flux hypothesis [Alfvén, 1942; Roberts & Scott, 1965]. For reasons which will be discussed in more detail in section 4.1, the radial field at the core–mantle boundary has to satisfy certain conditions, such as

$$F_i = \int_S \partial_t B_r dS = 0, \quad (3.61)$$

the flux through a patch S on the core surface bounded by a contour of zero radial field must be constant. A valid test of this hypothesis is to compare the changes of the flux

through individual flux patches. The dog bone patch R2 shows in 17 years (1980 – 1997) a change of its flux of about -20 MWb, in good agreement with Bloxham [1988], who found -25 MWb in 11.5 years. Another patch which shows drastic increase of flux is the St. Helena patch R3: within 20 years it changed its flux by 40 MWb, also in agreement with Bloxham [1988]. In the northern hemisphere the North Pole patches show considerable changes in size and flux. Beside the analysis of the flux through individual flux patches, there is one further possibility to test the consistency of the model, and consequently of the data, with the frozen flux hypothesis. A necessary, but not sufficient condition for the frozen flux to apply is that the quantity of the unsigned flux integral

$$\oint_{CMB} |B_r| dS = \text{const.}, \quad (3.62)$$

integrated over the surface of the core-mantle boundary should not change with time. Therefore a computation of this integral for each year is carried out and the differences for successive years are averaged of the whole period. In figure (3.9) the averaged differences, in fact time derivatives of eq.(3.62), is shown. The given error-bars are the sample variance of the integral for a specific truncation degree. For truncation degrees less than 9 a conservation of unsigned flux is not achieved, for higher degree this seems to be achieved within error margins, but it should be mentioned that the higher degrees of the model more and more reflects the a priori beliefs, i.e. spatial and temporal damping.

Holme & Olsen [2005] computed the unsigned flux integral as here, but using models of the secular variation and main field based on satellite data. Their results for unsigned flux integral concur with those here discussed up to truncation degree 9 or 10. Beyond that the integrals differ due to different modelling approaches. The conclusion on this might be that diffusion is more effective on larger length scales than on smaller ones.

This all gives rise to the presumptive evidence that the model can resolve the diffusion and further indicates a violation of the frozen flux hypothesis even on sub-decadal time scales [Bloxham & Gubbins, 1986], but it does not inevitably mean that the frozen flux assumption has to be abandoned, rather that the assumption is inadequate to explain the resolved secular variation entirely. Thus the observed secular variation in the southern hemisphere may be partly due to diffusion. It is most likely that diffusion might be enhanced by expulsion of toroidal flux by upwelling [Bloxham, 1986]. This mechanism also operates on the Sun, where regions of toroidal flux expulsion are seen as Sun spots. I will return to this topic at the end of the section 4.2.3, where I discuss flux expulsion due to fluid upwelling.

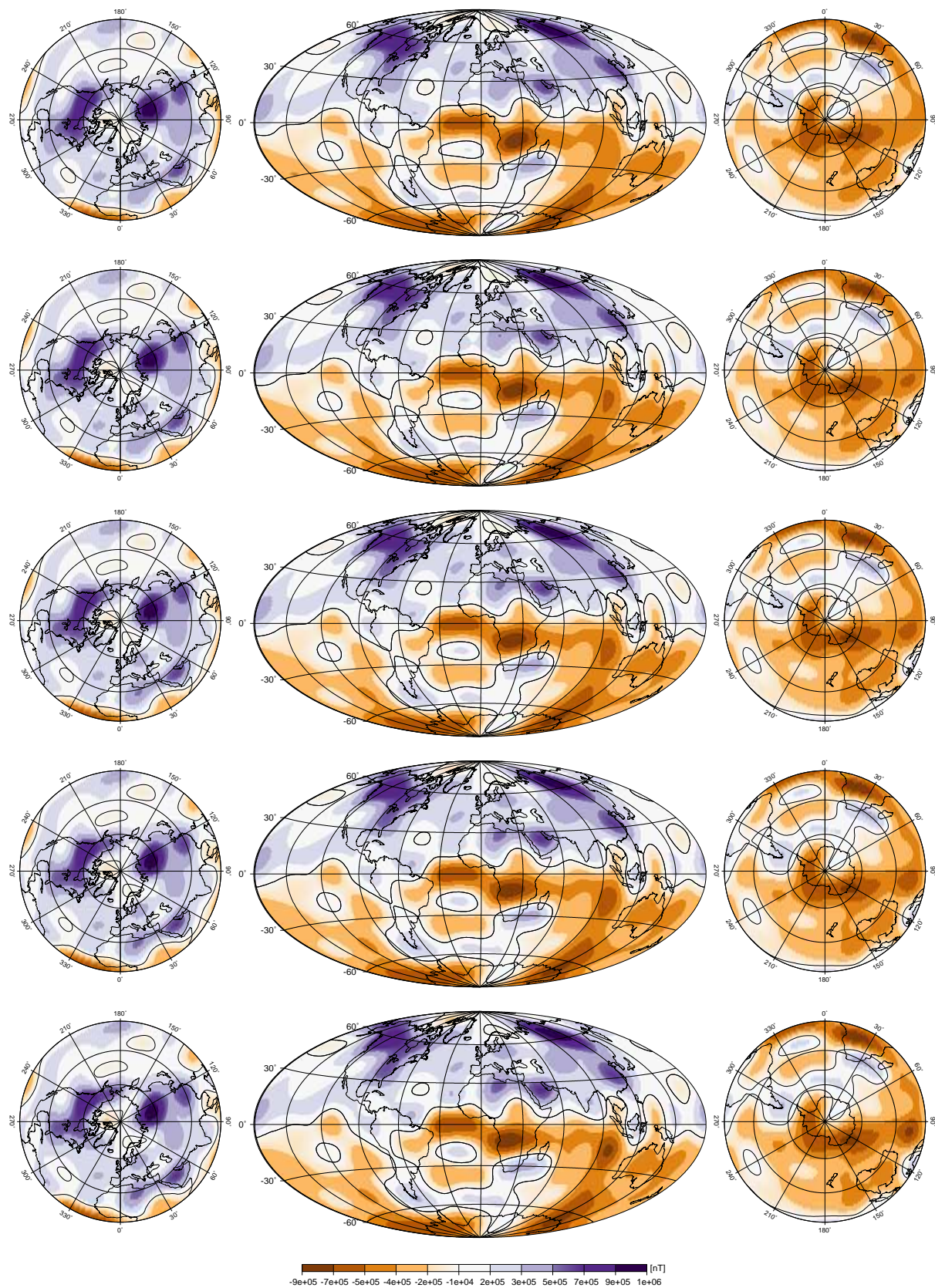


Figure 3.7: Radial component of the geomagnetic field at 1980, 1985, 1990, 1995 and 2000 from top to bottom (Mollweide equal-area projection).

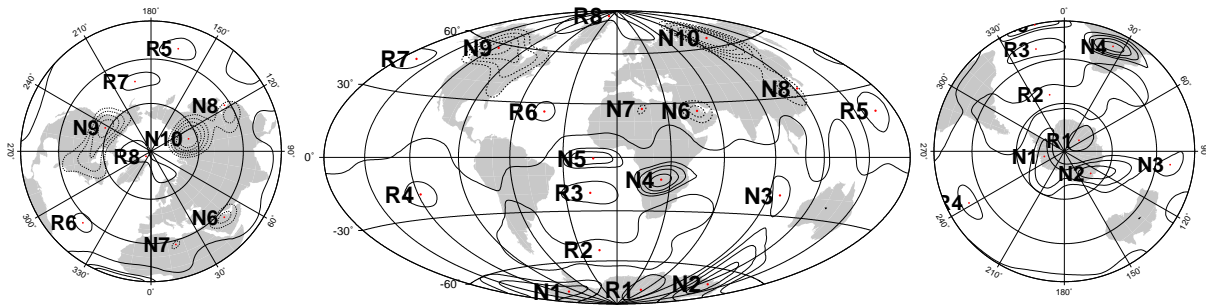


Figure 3.8: Radial component of the geomagnetic field, with key features of the field: reverse flux patches are labeled R1 – R8, normal flux patches as N1 – N10 (Mollweide equal-area projection).

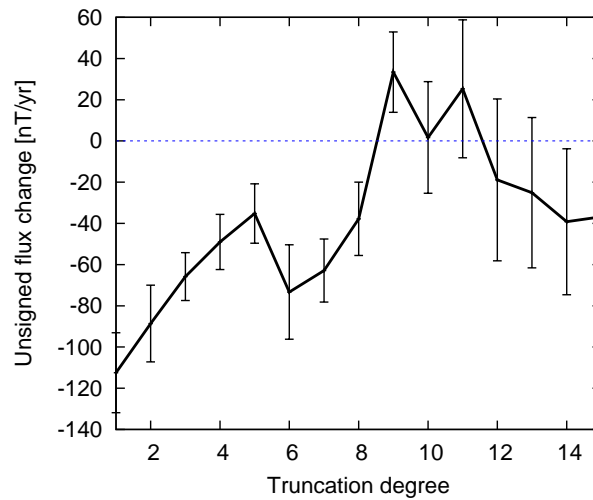


Figure 3.9: The mean change of the unsigned flux integral for 1980 – 2000.

3.5.2 The secular variation and geomagnetic jerks during this period

I now discuss the details of the modelled secular variation using the comparison between the model and the secular variation estimates of monthly means at a number of permanent observatories. In figure 3.10 this comparison is shown. The observatories are chosen to represent different latitudinal regions, polar as well as mid and low latitudinal regions.

The time-dependent model renders the observed secular variation well and even makes it possible to detect data errors such as unreported base line jumps, see for instance the graphs of Y and Z in Hermanus around 1997.

The model reveals a short term variability on sub-decadal scale for all components of the presented observatories in mid and low latitudes. What is also appearing, the secular variation of observatories at nearly the same latitude, but different longitude, show different monotonic behaviour, for example Niemegk and Newport or MBour and Pamatai. Only the monotonic behaviour of Hermanus and Eyrwell are comparable. These periods of increasing and decreasing secular variation are delineated by sudden events, where the slope of the secular variation changes its sign – geomagnetic jerks. These jerks are mainly identified on ground of the secular variation of the Y-component, because this component is less influenced by external field variation. I will discuss these events first on ground of the Y-component of the secular variation. The first of the geomagnetic jerks, which occurred during this period is visible around 1983 in the Y component of Hermanus [Dowson et al., 1987; Kotzé, 2003]. It was originally thought, that this event was only discernible in the recordings of observatories in the southern hemisphere, but the extent of this event seems to reach even mid latitudinal observatories as MBour. In 1990 a jerk was reported [Macmillan, 1996], mainly visible in East components of European observatories such as Niemegk. The third jerk during this period took place around 1999, also visible in European observatories [Mandea et al., 2000].

So far a discussion of the secular variation recorded in polar observatories has been left out, certainly because of the jammer of external field variation, which makes a discussion of secular variation at those sites not easy. However, the secular variation modelled by the time-dependent field model seems to be unaffected by this external noise. The variance of the observed secular variation is by a factor of 10 larger than the modelled secular variation. The 1983 and 1999 jerks are clearly seen in the Y-components of Resolute Bay and Scott Base, whereas the 1990 event is missed out in both observatories.

Beside the known jerks, there are further sudden events present in the secular variation. Clearly around 1986 and 1995, jerks happened in the southern hemisphere, whose amplitude fades away at more northerly observatories.

Also, the other components show distinct variation in this 20 years time span. My belief is that the secular variation in Y should not be discussed independently of those in X and Z, but caution should be paid to induction effects which might be present in the Z-component. However, the short term variations (shorter than 5 years) caused by external field variation seem to be not present in the model. This will be much clearer when considering figure 4.15. In these figures, without the large amplitude variation of the

secular variation estimates, the modelled secular variation (black line) is easier to view. Whereas the secular variation in X and Z of Resolute Bay and Scott Base is more or less featureless, for the others it is rich on details. All non-polar observatories show a distinct feature in Z around 1982 which also seen in dX/dt of Mbour and Pamatai. This feature is chronologically before the 1983 jerk. Also for the 1991 jerk, there are sharp changes in the secular variation of X and Z for most of the observatories visible, which leading or trailing the 1991 event by about one year.

In figure 3.11 the secular variation of the radial component of the magnetic field at the core-mantle boundary is shown. The structure is very heterogeneous. The largest amplitudes of the secular variation appear within a band $\pm 30^\circ$ about the equator. These patches remain steady within some margins during the 20 years.

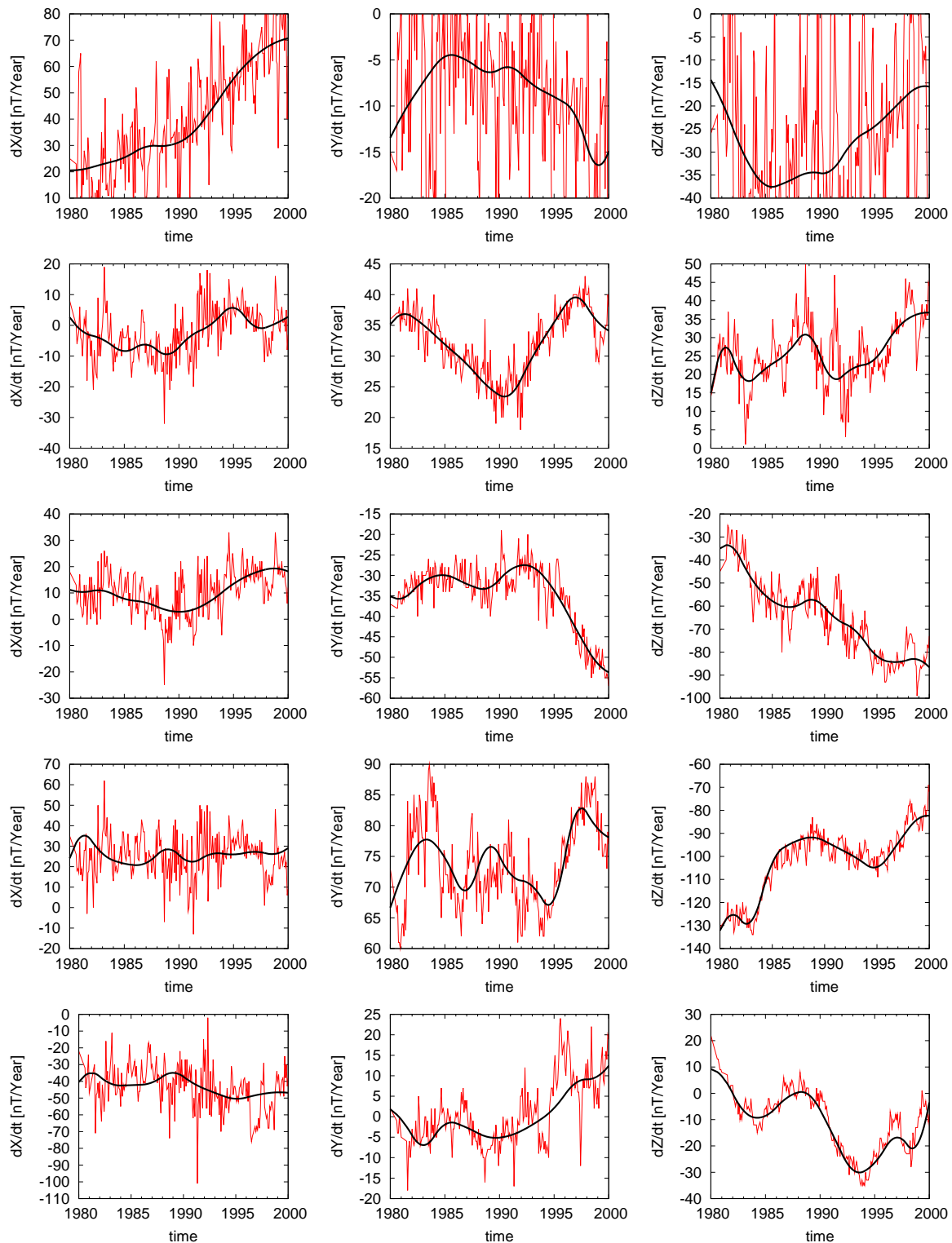


Figure 3.10: Comparison of modeled secular variation (black line) with the secular variation estimates at selected permanent observatories (red line). From left to right: dX/dt , dY/dt , dZ/dt . From top to bottom: Resolute Bay (Canada), Niemeck (Germany), Newport (USA), MBour (Senegal), Pamatai (French Polynesian).

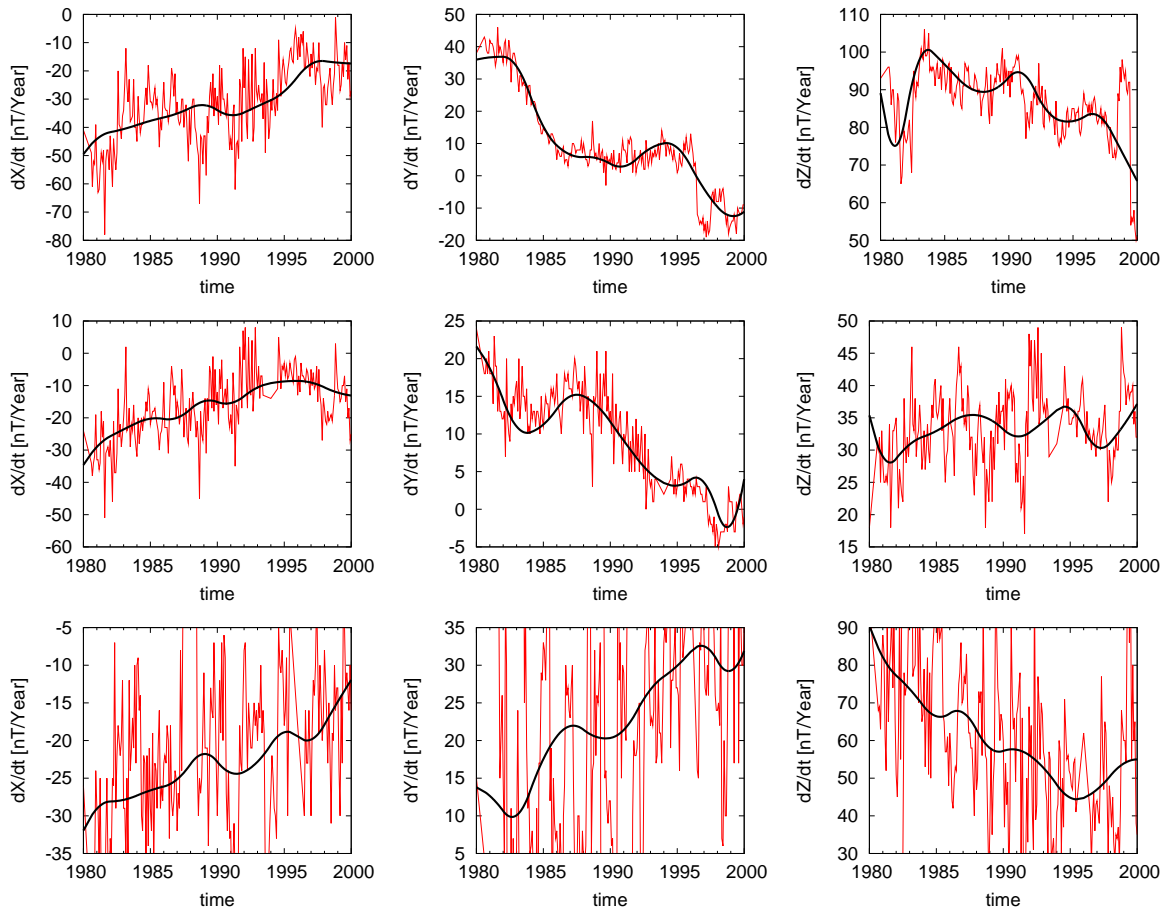


Figure 3.10: (*continued from previous page*) From top to bottom: Hermanus (South Africa), Eyrewell (New Zealand) and Scott Base (Antarctica).

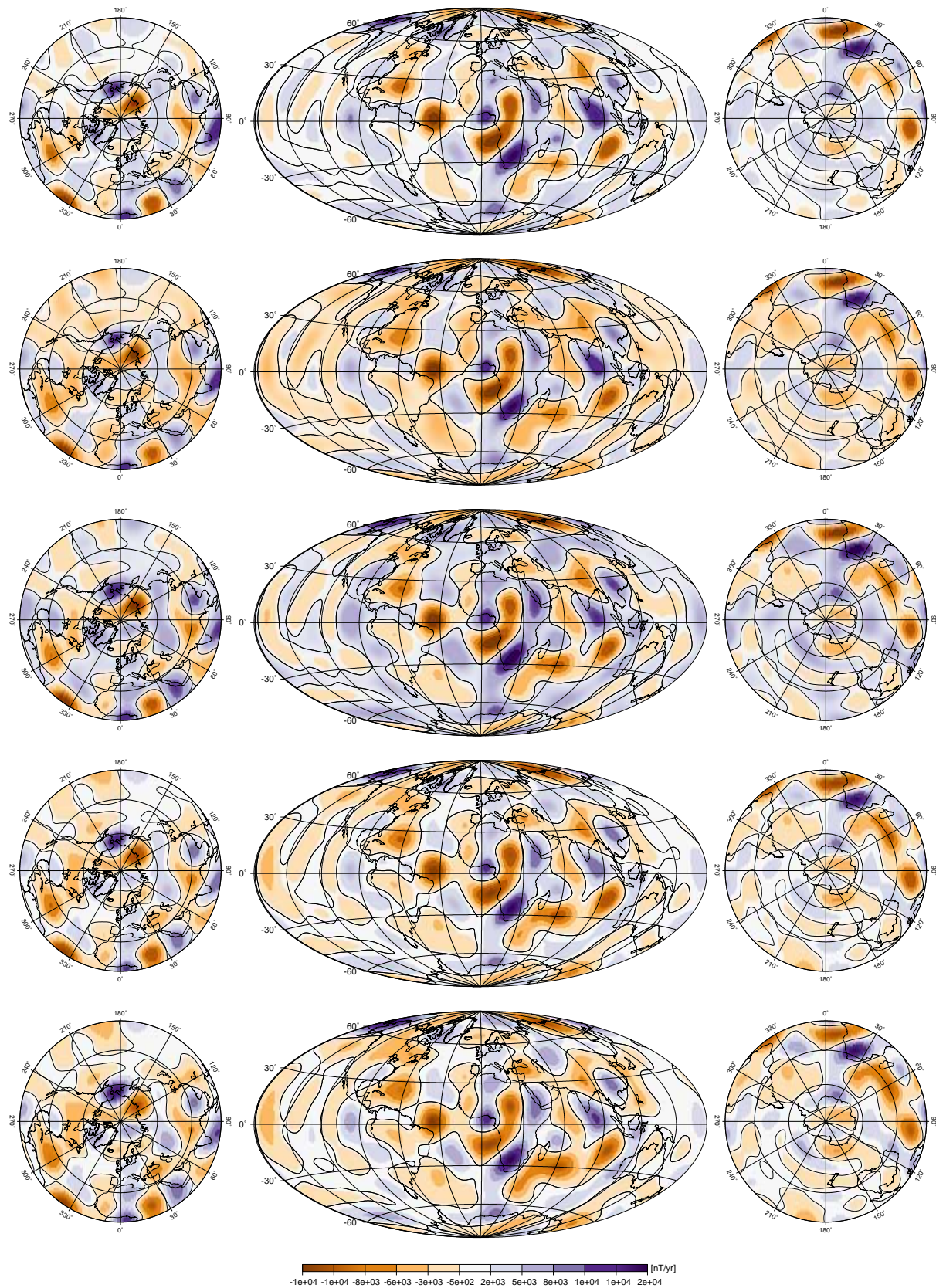


Figure 3.11: Radial component of the secular variation at 1980, 1985, 1990, 1995 and 2000 from top to bottom (Mollweide equal-area projection).

3.5.3 Analysis of the residuals

Figure 3.12 shows the residuals between model and data (left column). The highest residuals appear in both polar observatories Resolute and Scott Base. The variance of the residuals of the Y component in Resolute is smaller than for the other components. The same is true for the observatories in Niemeqk, Guam and Hermanus. Attention should be paid to the base line jumps in Hermanus in Y around 1997 and in Z around 1998. The curves in the middle column depict the autocorrelation function of the residuals in each component. The autocorrelation function is given by

$$A(\tau) = \frac{1}{N-r} \sum_{t=1}^{N-\tau} (x_t - \langle x_t \rangle) (x_{t+\tau} - \langle x_{t+\tau} \rangle) / (x_t - \langle x_t \rangle)^2, \quad (3.63)$$

where x_t is time series of the residuals and τ is the shift. Variations with periods multiple of τ will have a local maximum in $A(\tau)$. Apparently the dip at $\tau = 12$ in all curves is due to the processing of the data, to derive the secular variation estimates (cf. eq.3.2). The residuals show basically the same periodicities, with external origins as already discussed in chapter 1 for single observatories. The cross correlation function of the residuals against each other is given in the right column of the figure and is defined as

$$C(\tau) = \frac{1}{N-r} \frac{\sum_{t=1}^{N-\tau} (x_t - \langle x_t \rangle)(y_{t+\tau} - \langle y_{t+\tau} \rangle)}{\sqrt{(\sum_t (x_t - \langle x_t \rangle)^2)} \sqrt{(\sum_t (y_{t+\tau} - \langle y_t \rangle)^2)}}. \quad (3.64)$$

It shows the common correlations of two independent time series x_t and y_t .

The maxima at a lag of zero, which are evident in all figures, indicate that the variation of the residual components are correlated or anti-correlated, respectively. This could mean that the effect of variations, i.e. the semi-annual variation, causes a increase of the residuals lets say in X and Y, what gives a correlation, an increase in the residuals of X and a decrease of the residuals of Y signify an anti-correlation. In detail; Y and Z are anti-correlated in RES and HER and correlated in NGK and SBA, X and Y are correlated in RES and GUA and anti-correlated in NGK and HER, X and Z are anti-correlated in RES and NGK and correlated in HER. This behaviour is mainly due to the different geometries of the ring current at different location and due to different interaction with the distinct magnetization of the crust at each observatory site.

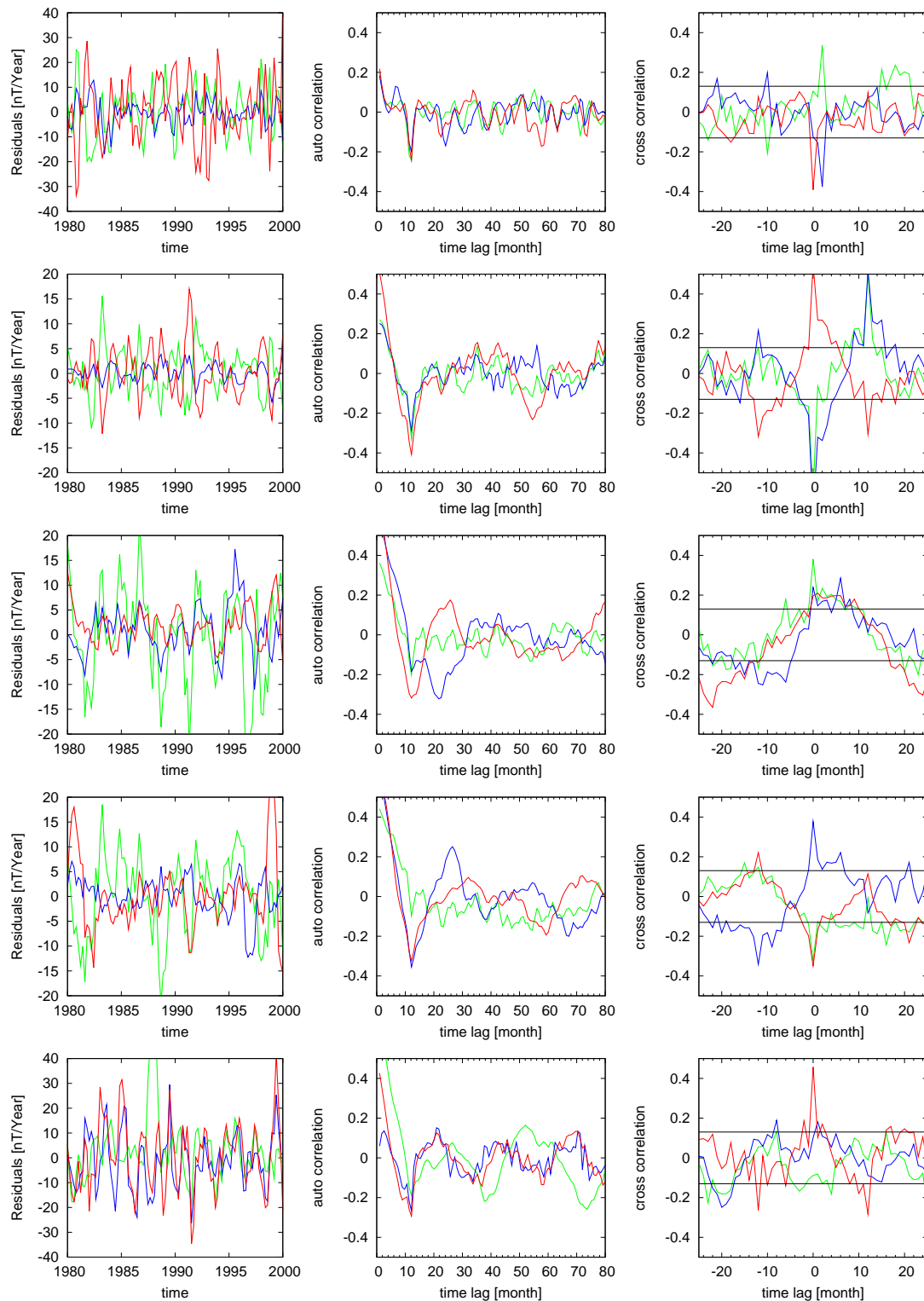


Figure 3.12: In the left column, Residuals between model and the secular variation estimates for Resolute Bay, Niamegk, Pamatai, Hermanus and Scott Base (from top to bottom). Residuals for X in green, Y in blue and Z in red. Autocorrelation function is shown with the same color scheme as for the residuals (middle column). Cross-correlation functions are presented, where the pink line is the cross-correlation function of X and Y, blue for X and Z and red for Y and Z. The horizontal black lines represent the 95 %

3.5.4 Covariance and Resolution Analysis

Up to now nothing has been stated about the confidence and errors of the gained solution \mathbf{m} . Therefore in this section the estimation of the uncertainties in the model is developed and discussed.

The significance of the model parameters are measured by the resolution and covariance matrices. The first gives the extent to which an individual parameter is determined by the data. The second quantifies the uncertainties in the model estimates due to inaccuracies in the measurements. Low resolution and inability to satisfy the data entirely are both sources of uncertainty in the model estimates. The resolution matrix is given by

$$\mathbf{R} = (\mathbf{A}^T \mathbf{C}_e^{-1} \mathbf{A} + \mathbf{C}_m^{-1} + \mathbf{C}_a^{-1})^{-1} \mathbf{A}^T \mathbf{C}_e^{-1} \mathbf{A}, \quad (3.65)$$

where \mathbf{C}_a and \mathbf{C}_m are defined in (3.54) and (3.51). Ideally, this matrix would be an identity matrix. Due to inadequacy of the data, a regularization scheme must be applied in the solving process to obtain a stable solution this is reflected in the form of the resolution matrix. A resolution near 1.0 signifies that a model parameter is wholly determined by the data, whereas a low resolution means that the model is mostly constrained by the a priori information. Figure 3.13 shows the estimates of the resolution of all 255 model parameters ($g_1^0, \dots, g_{15}^{15}$) for six different times of the interval. The model is less resolved by the data for 1980 and 2000, rather being constrained by the satellite models. This follows from (3.30) and (3.33), two of the four B-splines are constrained dominantly by the a priori model, whereas the two other are confined by the data. This is not an evidence of a contradiction in the method, it is rather a competition between the different qualities of satellite models and models derived from observatory data. The step-like appearance of these curves indicates that the resolution of the coefficients within a degree is nearly even. Only the coefficients g_8^m, h_8^m (coefficient numbers 64–80) show a slight tendency to a higher resolution with increased order. Gauss coefficients of order and degree greater than 12 (coefficient number > 168) are not resolved at all, only the resolution of the coefficients for 1980 (solid black line) seems not to vanish. This is certainly, because of the high spatial resolution of the MAGSAT satellite model, which originally was derived to degree and order 66.

Following the same considerations as in section 3.4.2, the covariance matrix of the solution is given by

$$\mathbf{C} = \hat{\sigma}^2 (\mathbf{A}^T \mathbf{C}_e^{-1} \mathbf{A} + \mathbf{C}_m + \mathbf{C}_a)^{-1} \quad (3.66)$$

where $\hat{\sigma}^2$ is the misfit of the model

$$\hat{\sigma}^2 = \frac{\mathbf{e}^T \mathbf{C}_e^{-1} \mathbf{e}}{N - Tr(\mathbf{R})} \quad (3.67)$$

and N the number of data and $Tr(\mathbf{R})$ the trace of the resolution matrix is equivalent to the degree of freedom. On ground of these considerations one would expect this matrix to be purely diagonal, but in fact the non-diagonal elements are not zero, which means that there is a dependency between coefficients of the same degree but different order.

This dependency is caused by an uneven distribution of observatories. Figure 3.14 shows the covariance estimates of the Gauss coefficients for six different times of the interval, separated by four years. The highest variance is shown by the dipole coefficients for the model in 1980. The variances for the Gauss coefficient of order and degree > 10 (coefficient numbers > 120) are almost zero. Higher damping parameters would force these curves to be equal zero for lower degrees. A zero variance of a model parameter means that this parameter does not deviate from the a priori beliefs. Hence, the high covariance of the dipole term is caused by a deviation of the MAGSAT model from the time-dependent model for 1980. Here again the different quality of satellite and observatory data are noticed.

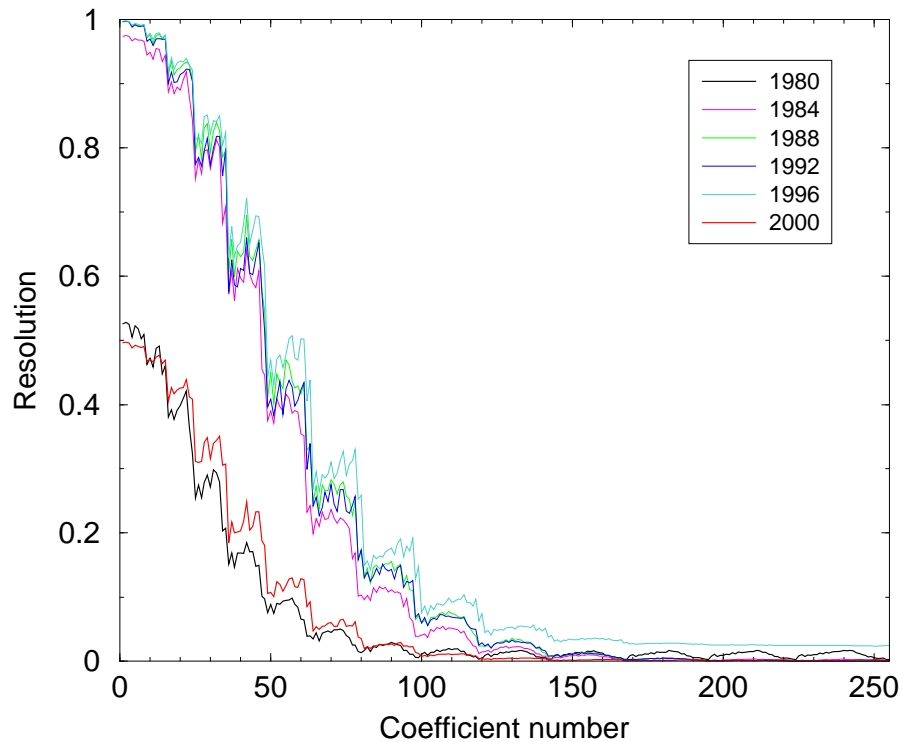


Figure 3.13: Resolution estimates of the Gauss coefficients at different times. Gauss coefficients are ordered with increasing l and m , i. e. $g_1^0, g_1^1, h_1^1, \dots, h_{15}^{15}$. The resolution of the coefficients with an order greater than 12 are nearly zero this indicates a nearly complete control of these coefficients by the a priori beliefs.

3.5.5 Conclusion

In this chapter, a time-dependent model of the secular variation up to degree and order 15 has been developed for the period 1980 to 2000. The model is constrained at the end points by satellite models derived from MAGSAT, CHAMP and ØRSTED data. It is unique in the (linear square) sense that it minimizes the model norms for the chosen

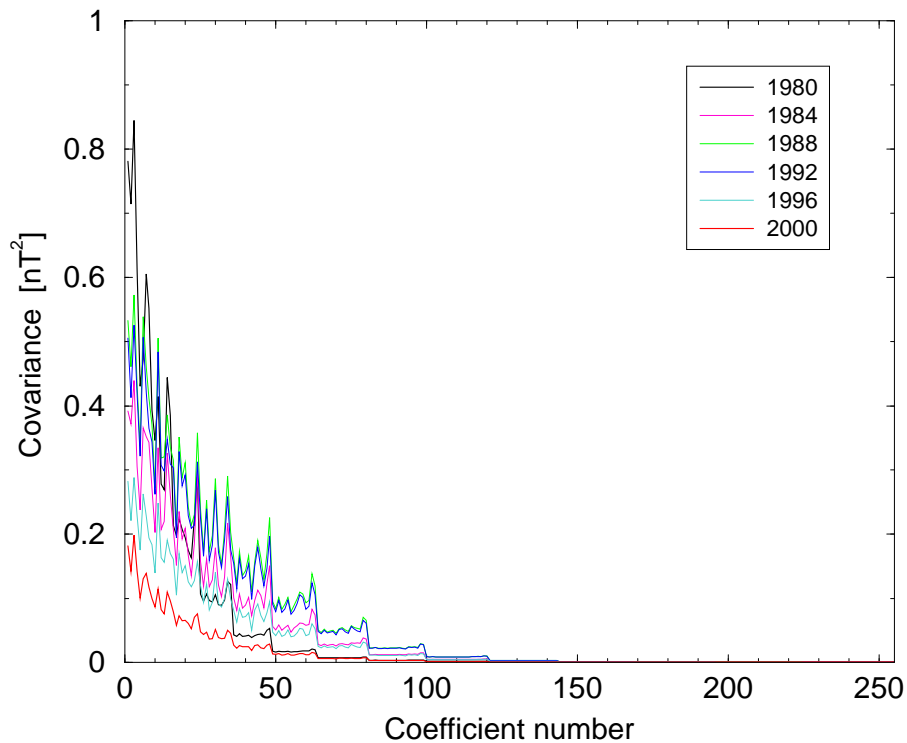


Figure 3.14: Covariance estimates of the Gauss coefficients at six different times. Gauss coefficients are ordered with increasing degree l and order m , i. e. $g_1^0, g_1^1, h_1^1, \dots, h_{15}^{15}$.

damping parameters. The results of the resolution analysis suggest that the constructed model is resolved by the data at least up to degree 11, hence, a good representation of the real geomagnetic field and its temporal behaviour. The model is a sensitive test to recover the geomagnetic jerks occurred in this period, and even resolve the changes of flux through the core–mantle boundary. Further, it gives evidence for a violation of the frozen flux hypothesis and therefore facilitates a valuable test of this hypothesis, which is essential in the computation of core surface motion.

Chapter 4

Qualitative analysis of the core–surface fluid motions

«Τὰ πάντα ρεῖ καὶ οὐδὲν μένει»
Heracleitos

In this chapter I explore core–surface fluid motions which explain the temporal variation of the magnetic field at the CMB over the period 1980 – 2000. The non-uniqueness of this inverse problem is fundamental and was first recognized by Roberts & Scott [1965] and formalized by Backus [1968] leading to some assumptions to reduce the non-uniqueness of the geomagnetic core–surface motion problem. I will discuss the main assumptions, their shortcomings and the resulting fluid motion prediction. Furthermore I will highlight some geophysical implications for the Earth’s angular momentum budget and geomagnetic jerks.

4.1 Inversion for core–surface flows

The secular variation of the magnetic field at a fixed point is characterized by two processes. First, there is a change in the field due to the advection of magnetic flux tubes by the fluid motion. Second, there is a diffusion of field lines relative to the motions due to ohmic dissipation. The induction equation for the magnetic field,

$$\partial_t \mathbf{B} = \nabla \times (\mathbf{u} \times \mathbf{B}) + \eta \nabla^2 \mathbf{B} , \quad (4.1)$$

with the condition

$$\nabla \cdot \mathbf{B} = 0 \quad (4.2)$$

describes how the time rate of change of the magnetic field \mathbf{B} is due to these effects. \mathbf{u} is the fluid velocity and $\eta = 1/(\mu\sigma)$ the magnetic diffusivity assumed uniform, with the magnetic permeability μ and σ the electrical conductivity of the core fluid. The first term of the right hand side (rhs) of the induction equation (4.1) represent the advection, the second term the diffusion of magnetic field lines. The ratio of transport to diffusion terms

in equation (4.1) is usually quantified by the magnetic Reynolds number R_m

$$\frac{|\nabla \times (\mathbf{u} \times \mathbf{B})|}{|\eta \nabla^2 \mathbf{B}|} \sim \frac{UL}{\eta} = R_m, \quad (4.3)$$

where U and L are characteristic velocity and length scales of the fluid motion, respectively. The length scales for advection and diffusion are assumed to be the same. With typical values ($L \simeq 10^6$ m, $U \simeq 5 \times 10^{-4}$ m s $^{-1}$, $\eta \simeq 1$ m 2 s $^{-1}$) equation (4.3) gives that $R_m \approx 500$. Convection is apparently more important than diffusion. Alfvén [1942] suggested that diffusion could be neglected, the magnetic field being effectively frozen into the fluid. The magnetic field in a moving perfect conductor is governed by the diffusion-less induction equation

$$\partial_t \mathbf{B} = \nabla \times (\mathbf{u} \times \mathbf{B}) \quad (4.4)$$

With this condition, it can be shown that the frozen flux condition applies; the magnetic field is frozen within the fluid. The frozen–flux theorem and was first applied by Roberts & Scott [1965] to analyze the secular variation. They inverted the reduced equation for the flow at the core surface.

Now requiring that there is no fluid flow across the core–mantle boundary,

$$\mathbf{u}_r = 0 \Big|_{r=c} \quad (4.5)$$

and following the arguments of Backus [1968], then a further condition can be deduced which $\partial_t \mathbf{B}_r$ must satisfy if it is purely due to advection of \mathbf{B}_r in a continuous velocity field \mathbf{u} on the CMB:

If A is any patch on the CMB whose boundary ∂A is a null-flux curve ($\mathbf{B}_r = 0$ along this curve), then

$$\int_A \partial_t \mathbf{B}_r dA = 0. \quad (4.6)$$

If either of these conditions fails, no continuous \mathbf{u} will generate $\partial_t \mathbf{B}_r$ from \mathbf{B}_r , and flux diffusion must be invoked. From these conditions, Backus [1968] showed that, if there exists one (unique) \mathbf{u} which satisfies (4.4), then there exist infinitely many. This is more obvious considering the radial diffusion-less induction equation

$$\begin{aligned} \partial_t \mathbf{B}_r + \nabla_h \cdot (\mathbf{u} \mathbf{B}_r) &= 0 \\ \partial_t \mathbf{B}_r + \mathbf{B}_r \nabla_h \cdot \mathbf{u} + \mathbf{u} \cdot \nabla_h \mathbf{B}_r &= 0 \end{aligned} \quad (4.7)$$

where $\nabla_h = \nabla - \hat{r}(\hat{r} \cdot \nabla)$ is the horizontal divergence. A single equation (4.7) must be solved for two unknowns $\mathbf{u}_h = \{\mathbf{u}_\theta, \mathbf{u}_\phi\}$. The non–uniqueness can be reduced by imposing further constraint on the nature of the flow. Four different methods, which have been developed in the last two decades, are discussed in this chapter: steady flow, steady flow in an azimuthally drifting reference frame, tangentially geostrophic flow and flow caused by torsional oscillations. All these flow assumptions have in common a scheme of computation, which is outlined in the next section.

4.1.1 Scheme of the flow computation

The formalism of the flow calculation bases on a poloidal–toroidal decomposition of the velocity field as formulated by Roberts & Scott [1965]. Assuming $\nabla \cdot \mathbf{u} = 0$, the velocity field can be expressed in terms of two scalar functions of positions on the sphere, S and T . These functions can be expanded in spherical harmonics. So the decomposition reads

$$\mathbf{u} = \mathbf{u}_p + \mathbf{u}_t, \quad (4.8)$$

where

$$\begin{aligned} \mathbf{u}_p &= \nabla_H(r S) = \left(0, \frac{\partial S}{\partial \theta}, \frac{1}{\sin \theta} \frac{\partial S}{\partial \phi} \right) \\ \mathbf{u}_t &= \nabla_H \times (\mathbf{r} T) = \left(0, \frac{1}{\sin \theta} \frac{\partial T}{\partial \phi}, -\frac{\partial T}{\partial \theta} \right), \end{aligned} \quad (4.9)$$

are the poloidal and toroidal velocities and

$$\begin{aligned} S(\theta, \phi) &= \sum_{l=1}^{\infty} \sum_{m=0}^l s_l^m Y_l^m(\theta, \phi) \\ T(\theta, \phi) &= \sum_{l=1}^{\infty} \sum_{m=0}^l t_l^m Y_l^m(\theta, \phi). \end{aligned} \quad (4.10)$$

Y_l^m is a real Schmidt quasi–normalized spherical harmonic. Substituting (4.8), (4.9), (4.10) into the rearranged radial induction equation (4.7)

$$\partial_t \mathbf{B}_r + \mathbf{u} \cdot \nabla_h \mathbf{B}_r + \mathbf{B}_r \nabla_h \cdot \mathbf{u} = 0$$

leads to a matrix equation

$$\dot{\mathbf{b}} = \mathbf{A} \mathbf{m} = \mathbf{E} \mathbf{t} + \mathbf{G} \mathbf{s} \quad (4.11)$$

which relates secular variation coefficients $\dot{\mathbf{b}} = \partial_t \mathbf{B} = \{\dot{g}_l^m, \dot{h}_l^m\}$ with toroidal and poloidal coefficients as model vector $\mathbf{m} = \{t_l^m, s_l^m\}$. The matrices \mathbf{E} , \mathbf{G} are the Elsasser and Gaunt matrices. Following Bloxham [1988] the matrices have elements like

$$\begin{aligned} E_{l_1 l_3}^{m_1 m_3} &= \frac{1}{4\pi c} \left(\frac{c}{a}\right)^{l_1+2} \frac{2l_1+1}{l_1+1} \sum_{l_2, m_2} \left(\frac{c}{a}\right)^{l_2+2} (l_2+1) g_{l_2}^{m_2} \\ &\quad \times \oint \left(\frac{\partial Y_{l_3}^{m_3}}{\partial \theta} \frac{\partial Y_{l_2}^{m_2}}{\partial \phi} - \frac{\partial Y_{l_2}^{m_2}}{\partial \theta} \frac{\partial Y_{l_3}^{m_3}}{\partial \phi} \right) \frac{Y_{l_1}^{m_1}}{\sin \theta} dS \\ G_{l_1 l_3}^{m_1 m_3} &= \frac{1}{8\pi c} \left(\frac{c}{a}\right)^{l_1+2} \frac{2l_1+1}{l_1+1} \sum_{l_2, m_2} \left(\frac{c}{a}\right)^{l_2+2} (l_2+1) [l_1(l_1+1) + l_3(l_3+1) - l_2(l_2+1)] g_{l_2}^{m_2} \\ &\quad \times \oint Y_{l_1}^{m_1} Y_{l_2}^{m_2} Y_{l_3}^{m_3} dS \end{aligned}$$

These integrals are non-zero only for certain pairs of $(l_1, m_1), (l_2, m_2), (l_3, m_3)$ [Bullard & Gellman, 1954].

Equation (4.11) represents a linear inverse problem, $\partial_t \mathbf{B}$ and \mathbf{B} are given in terms of Gauss coefficients, which were derived in the previous part of this study (chapter 3).

In the next sections I discuss some assumptions of how to relate the poloidal and toroidal velocities in order to solve equation (4.7) with less ambiguity for the core–surface flow.

4.1.2 Steady motion theorem

The idea first made by Gubbins [1982] that an unique solution could be derived by assuming the flow to be the same at three different times for a given point on the CMB was first formalized by Voorhies & Backus [1985]. Their approach as follows.

Suppose that for a given point on the CMB at three different times $\{t_i; i = 1, 2, 3\}$ \mathbf{u}_h is the same, then three simultaneous equations for the unknowns $\mathbf{u}_\theta, \mathbf{u}_\phi, \partial \mathbf{u}_r / \partial r$ are given, namely

$$\partial_t \mathbf{B}_r(t_i) = \mathbf{B}_r(t_i) \frac{\partial \mathbf{u}_r}{\partial r} - \frac{1}{r} \frac{\partial \mathbf{B}_r(t_i)}{\partial \theta} \mathbf{u}_\theta - \frac{1}{r \sin \theta} \frac{\partial \mathbf{B}_r(t_i)}{\partial \phi} \mathbf{u}_\phi. \quad (4.12)$$

A unique solution exists, when the determinant is

$$\Delta = \hat{r} \cdot [\mathbf{B}_1(\mathbf{b}_2 \times \mathbf{b}_3) + \mathbf{B}_2(\mathbf{b}_3 \times \mathbf{b}_1) + \mathbf{B}_3(\mathbf{b}_1 \times \mathbf{b}_2)] \neq 0, \quad (4.13)$$

where $\mathbf{B}_i = \mathbf{B}_r(t_i)$, $\mathbf{b}_i = \nabla_h \mathbf{B}_r(t_i)$ and $\dot{\mathbf{B}}_i = \partial_t \mathbf{B}_r(t_i)$. Then the solution is given by

$$\mathbf{u}_h = \Delta^{-1} \hat{r} \times \begin{vmatrix} \mathbf{b}_1 & \mathbf{b}_2 & \mathbf{b}_3 \\ \mathbf{B}_1 & \mathbf{B}_2 & \mathbf{B}_3 \\ \dot{\mathbf{B}}_1 & \dot{\mathbf{B}}_2 & \dot{\mathbf{B}}_3 \end{vmatrix}. \quad (4.14)$$

The condition $\Delta \neq 0$ reflects the fact that a minimal temporal variation of \mathbf{B}_r is required to solve for the core–surface motion uniquely. Without this variability, even the assumption $\partial_t \mathbf{u}_h = 0$ does not permit \mathbf{u}_h to be uniquely determined from magnetic measurements [Voorhies & Backus, 1985]. The immanent problem of the steady motion theorem is the fact that for short periods (some decades) applied the determinant Δ decreases and the three simultaneous equations become progressively less well conditioned, whereas applied for long periods (50 – 300 years) it does not recover rapid secular variation, i.e. geomagnetic jerks, at all. The conclusion is that time dependence of the flow is critical to the validity of the frozen flux hypothesis.

4.1.3 Steady flow in a azimuthally drifting reference frame

An extension of the steady flow assumption is the consideration of a steady flow in an azimuthally drifting reference frame. This approach, suggested by Voorhies & Backus [1985], and developed by Davis & Whaler [1996]; Holme & Whaler [2001] assumes the flow is steady in a frame fixed to the core, where the core frame is allowed to rotate with respect to the mantle about the Earth’s rotation axis. The drift rate of this core frame might be

variable. For the remainder of this section, the primed variables are those of the drifting core frame.

Let

$$\psi = \phi - \phi', \quad (4.15)$$

where ψ is the accumulated drift angle. Then the flow as seen from the mantle frame is

$$\mathbf{u}(\theta, \phi, t) = \mathbf{u}'(\theta, \phi - \psi(t)) + r_c \frac{d\psi}{dt} \cos \theta \hat{\phi}, \quad (4.16)$$

where $\hat{\phi}$ is the azimuthal unit vector. Then

$$\partial_t \mathbf{B}_r' + \nabla_h (\mathbf{u}_h' \mathbf{B}_r') = 0 \quad (4.17)$$

is solved under the assumption of steady flow in the drifting core frame. Because of the Galilean invariance of \mathbf{B} it must be the same whether in the stationary or drifting frame, so the Gauss coefficients in the drifting frame are

$$\begin{aligned} g_l^{m'} &= g_l^m \cos m\psi + h_l^m \sin m\psi, \\ h_l^{m'} &= h_l^m \cos m\psi - g_l^m \sin m\psi. \end{aligned} \quad (4.18)$$

The secular variation coefficients are

$$\begin{aligned} \dot{g}_l^{m'} &= \dot{g}_l^m \cos m\psi + \dot{h}_l^m \sin m\psi + m\dot{\psi} h_l^{m'}, \\ \dot{h}_l^{m'} &= \dot{h}_l^m \cos m\psi - \dot{g}_l^m \sin m\psi - m\dot{\psi} g_l^{m'}, \end{aligned} \quad (4.19)$$

where the last term accounts for the relative velocity between mantle and core. Both transformations (4.18) and (4.19) are non-linear in drift angle Ψ .

Prescribed by the non-linearity of the transformation of the predicted $\dot{\mathbf{B}}_r$ from the core to the mantle frame, the inversion is divided into two steps:

- 1.) The computation of the steady flow in the core frame. Here the flow velocity is represented as a linear combination of toroidal and poloidal vectors as outlined in section (4.1.1). The objective function to be minimized

$$\Theta(m) = (\mathbf{y} - \mathbf{A}\mathbf{m})^\top \mathbf{C}_e^{-1} (\mathbf{y} - \mathbf{A}\mathbf{m}) + \lambda_v \mathbf{m}^\top \mathbf{C}_m^{-1} \mathbf{m}, \quad (4.20)$$

where

$$\mathbf{m}^\top \mathbf{C}_m \mathbf{m} = \oint \left[(\nabla_h^2 \mathbf{u}_\theta)^2 + (\nabla_h^2 \mathbf{u}_\phi)^2 \right] dS = \sum_l \frac{l^3 (l+1)^3}{2l+1} \sum_m [(t_l^m)^2 + (s_l^m)^2]. \quad (4.21)$$

λ_v is the damping parameter. Finally the solution for the model vector \mathbf{m} is given by (3.24).

- 2.) The accumulated drift angle is parameterized as a function of time on the basis of cubic B-splines with 2.5 year knot spacing. Utilizing the cubic B-splines allows easy derivation of the drift rate $\dot{\psi}$ and the drift acceleration $\ddot{\psi}$.

The algorithm is set up to optimize for a set of spline coefficients which minimize the integral

$$\int_{t_1}^{t_2} \left[\int_{CMB} (\dot{\mathbf{B}}_r^{obs} - \dot{\mathbf{B}}_r^{pred}) dS + \lambda_d (\ddot{\psi})^2 \right] dt + \mathbf{C}_m \quad (4.22)$$

For each (non-linear) optimization step, to find the spline coefficients, the linear flow problem is solved. The non-linear optimization method applied here is the Powell's method to minimize a function of multiple variables [Press et al., 1993].

4.1.4 Geostrophic flow

This method follows from consideration of the force balance at the core–mantle boundary. Let us first consider the Navier–Stokes equation, which describes the forces acting in the viscous top layers of the core. The equation of motion and transfer of a viscous fluid in a rotating system reads

$$\rho \left(\frac{\partial \mathbf{u}}{\partial t} + (\mathbf{u} \cdot \nabla) \mathbf{u} \right) = -\nabla p + \rho \left(\rho' \mathbf{g} - 2\boldsymbol{\Omega} \times \mathbf{u} - \boldsymbol{\Omega} \times (\boldsymbol{\Omega} \times r) + \mu \nabla^2 \mathbf{u} \right) + \mathbf{J} \times \mathbf{B} \quad (4.23)$$

where p is the non-hydrostatic part of the pressure, \mathbf{g} gravitation, ρ the density, ρ' density fluctuation, \mathbf{u} the fluid velocity, $\boldsymbol{\Omega}$ the Earth's angular velocity, μ the dynamic viscosity, \mathbf{J} the current density and \mathbf{B} the magnetic field. Suppose ρ is uniform and \mathbf{g} is a conservative force, so that

$$\mathbf{g} = -\nabla \Phi \quad (4.24)$$

where Φ is the potential function¹. The centrifugal terms can be rewritten by

$$\boldsymbol{\Omega} \times (\boldsymbol{\Omega} \times r) = -\nabla \left(\frac{1}{2} |\boldsymbol{\Omega} \times r|^2 \right), \quad (4.25)$$

then combining (4.24) and (4.25) gives an effective gravity $g_e = -\nabla(\Phi + \frac{1}{2} |\boldsymbol{\Omega} \times r|^2)$; then we can write (4.23)

$$\frac{\partial \mathbf{u}}{\partial t} + (\mathbf{u} \cdot \nabla) \mathbf{u} = -\frac{1}{\rho} \nabla p - 2\boldsymbol{\Omega} \times \mathbf{u} + \nu \nabla^2 \mathbf{u} + \frac{1}{\rho} (\mathbf{J} \times \mathbf{B}) + \frac{\rho'}{\rho} g_e \quad (4.26)$$

where $\nu = \mu/\rho$ is the kinematic viscosity.

The geostrophic motion constraint, suggested by Hills [1979] and Le Mouél [1984] is based on the hypothesis that the Coriolis force balances the pressure gradient. This seems

¹There are various sign conventions, I prefer to use the sign, that positive work is done against the potential.

to be justified, when all other forces compared with the Coriolis force are small:

$$\frac{\text{inertial force}}{\text{Coriolis force}} = \frac{|(\mathbf{u} \cdot \nabla)\mathbf{u}|}{|2(\boldsymbol{\Omega} \times \mathbf{u})|} \cong \frac{U}{2\boldsymbol{\Omega}L \cos \theta} \cong 10^{-6}/\cos \theta, \quad (4.27)$$

$$\frac{\text{driving force}}{\text{Coriolis force}} = \frac{|\partial\mathbf{u}/\partial t|}{|2(\boldsymbol{\Omega} \times \mathbf{u})|} \cong \frac{1}{2\boldsymbol{\Omega}T \cos \theta} \cong 10^{-5}/\cos \theta, \quad (4.28)$$

$$\frac{\text{viscous force}}{\text{Coriolis force}} = \frac{|\nu^2 \nabla^2 \mathbf{u}|}{|2(\boldsymbol{\Omega} \times \mathbf{u})|} \cong \frac{\nu}{2\boldsymbol{\Omega}L^2 \cos \theta} \cong 10^{-15}/\cos \theta, \quad (4.29)$$

where $L = 10^6\text{m}$, $U = 10^{-4}\text{ms}^{-1}$ (corresponding to a westward drift rate of 0.2° per year) and $T = 10^8\text{s}$. Estimations of the ratio of the Lorentz to Coriolis force are less simple, because only poloidal field is observable outside the core, whereas little is known about the toroidal field in the core–mantle boundary region. Every assessment of the ratio of the Lorentz and Coriolis force rely on the assumption that the toroidal field is weak and vanishes outside the core.

A lower bound for the poloidal field at the CMB is $B_p = 5 \cdot 10^{-4}T$. This value is given by a downward continuation of the observed magnetic field strength at the Earth's surface. For a purely poloidal field at the top of the core it is

$$\frac{\text{Lorentz force}}{\text{Coriolis force}} = \frac{|\mathbf{J} \times \mathbf{B}_p|}{|2\rho(\boldsymbol{\Omega} \times \mathbf{u})|} \cong \frac{B_p^2}{2\rho\boldsymbol{\Omega}LU \cos \theta} \cong 10^{-3}/\cos \theta. \quad (4.30)$$

Then the flow in the top layers of the core is governed by this simplified equation of motion

$$-\frac{1}{\rho}\nabla p = 2(\boldsymbol{\Omega} \times \mathbf{u}), \quad (4.31)$$

$$\nabla \cdot \mathbf{u} = 0. \quad (4.32)$$

Equation 4.31 is known as the geostrophic flow equation and can be useful in approximating quasi-steady large-scale flow in the ocean, the atmosphere or even at the core–mantle boundary. An interesting result of the geostrophic flow equation is that the velocity field is found to be perpendicular to the pressure gradient.

The important result of the geostrophic flow approximation can be deduced by curling (4.31).

$$\nabla \times (2\boldsymbol{\Omega} \times \mathbf{u}) = -\frac{1}{\rho}\nabla \times (\nabla p) = 0. \quad (4.33)$$

Using the vector identity

$$\nabla \times (A \times B) = A\nabla \cdot B + (B \cdot \nabla)A - B\nabla \cdot A - (A \cdot \nabla)B$$

then the equation reads

$$\boldsymbol{\Omega}\nabla \cdot \mathbf{u} + (\mathbf{u} \cdot \nabla)\boldsymbol{\Omega} - \mathbf{u}(\nabla \cdot \boldsymbol{\Omega}) - (2\boldsymbol{\Omega} \cdot \nabla)\mathbf{u} = 0 \quad (4.34)$$

Ω is independent of the position, so it follows

$$\Omega \nabla \cdot \mathbf{u} - (\Omega \cdot \nabla) \mathbf{u} = 0. \quad (4.35)$$

Finally equation (4.32) gives

$$\Omega \cdot \nabla \cdot \mathbf{u} = 0. \quad (4.36)$$

By convention, the direction of Ω is parallel to z

$$2\Omega \nabla \cdot \mathbf{u} = 2\Omega \frac{\partial \mathbf{u}}{\partial z} = 0 \rightarrow \frac{\partial \mathbf{u}}{\partial z} = 0. \quad (4.37)$$

In words it means that in the absence of external forces the slow flow of a rotating, homogeneous, inviscid fluid is necessarily two–dimensional. The motion is confined to planes perpendicular to the axis of rotation. If the fluid is contained in a rigid spherical container, then the restriction on the motion is even more severe, the only slow motion possible are those in which cylindrical shells rotate like rigid bodies about the axis of rotation [Bullard & Gellman, 1954]. This result is known as Proudman–Taylor theorem [Proudman, 1916; Taylor, 1917], but was first derived by Hough [1897].

Now confining the flow in a horizontal plane to be geostrophic – no flow across the boundary

$$\mathbf{u}_r = 0 \Big|_{r=c}, \quad (4.38)$$

then (4.31) reads

$$-\frac{1}{\rho} \nabla_h p = 2(\Omega \times \mathbf{u})_h. \quad (4.39)$$

Multiplying (4.39) with r and taking the horizontal divergence yields the tangentially geostrophic constraint

$$\nabla_h(\mathbf{u} \cos \theta) = 0. \quad (4.40)$$

The validity of (4.39) and therefore (4.40) breaks down at the geographical equator, where the pressure gradient cannot be balanced by Coriolis force any longer. Hence, the flow motion cannot be resolved uniquely. Backus & Le Mouél [1986] called this the leaky belt, but as pointed out by Chulliat & Hulot [2001] the non–uniqueness extend even to larger region than a equatorial band. The geostrophic regions can be defined as a set of points, where $|B_r / \cos \theta| \leq \zeta^2$. The value of ζ essentially depends on the radial derivative of the toroidal field (which is unknown), Chulliat & Hulot [2000] put a lower bound on $\zeta = 10^{-3} T$. The bright patches in figure 4.1 correspond to areas where the geostrophic assumption is expected to fail.

To construct solutions for (4.11) stochastic inversion (see section 3.4.2) is applied. The solution has to minimize the norm

$$\mathbf{m}^T N_S \mathbf{m} = \oint \left[(\nabla_h^2 \mathbf{u}_\theta)^2 + (\nabla_h^2 \mathbf{u}_\phi)^2 \right] dS = \sum_l \frac{l^3 (l+1)^3}{2l+1} \sum_m [(t_l^m)^2 + (s_l^m)^2], \quad (4.41)$$

²Holme [priv. comm.] pointed out that flows perpendicular to the regions for which the geostrophic contours are closed are not resolved by tangential geostrophy.

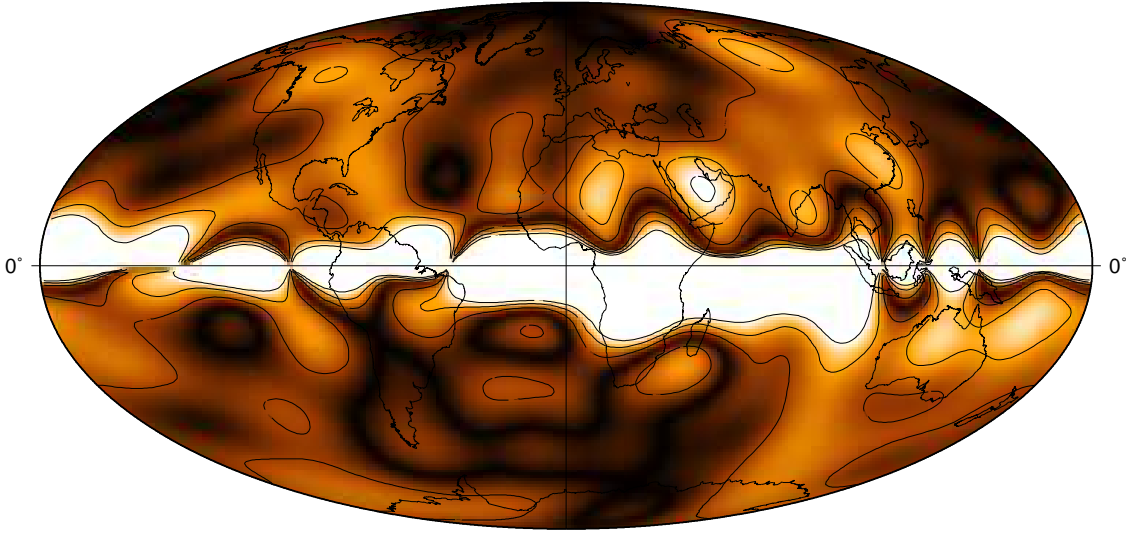


Figure 4.1: Sketch of the geostrophic degeneracy, the white region are the areas where the geostrophic assumption is expected to fail. ζ is chosen to be $10^{-3}T$.

i.e. the spatial roughness and the numerical convergence by the truncation degree of the velocity field at the CMB [Bloxham, 1988]. Further the solution should be smooth in time and minimizes

$$\mathbf{m}^T N_T \mathbf{m} = \oint \left(\frac{\partial \mathbf{u}}{\partial t} \right)^2 dS = \sum_l \frac{l(l+1)}{2l+1} \sum_m [t_l^m + s_l^m]^2. \quad (4.42)$$

The flow is also forced to be close to tangential geostrophic and therefore to minimize the quantity

$$\mathbf{m}^T N_G \mathbf{m} = \oint \left[\nabla_h \cdot (\mathbf{u} \cos(\theta)) \right]^2 dS. \quad (4.43)$$

All three norms can be expressed as quadratic form

$$\mathbf{m}^T \mathbf{C}_m^{-1} \mathbf{m} = \lambda_s N_S^{-1} + \lambda_t N_T^{-1} + \lambda_g N_G^{-1}, \quad (4.44)$$

which gives the formal solution

$$\mathbf{m} = (\mathbf{A}^T \mathbf{C}_e^{-1} \mathbf{A} + \mathbf{C}_m)^{-1} \mathbf{A}^T \mathbf{C}_e^{-1} \dot{\mathbf{b}} \quad (4.45)$$

that minimizes an objective function similar to (3.25). The results of the flow inversion are discussed in section (4.2).

4.1.5 Torsional oscillation

It has been suggested that an observed variation of the magnetic field with a period of ≈ 60 years may be related to torsional oscillations of rigid cylindrical surfaces aligned with the rotation axis [Braginskii, 1970, 1984].

The last section provided the dynamical description on cylindrical surfaces leading now to an analysis of these oscillations around an quasi–equilibrium state, the so–called Taylor state.

Taylor [1963] considered the steady ($\partial/\partial t = 0$), slow motion of an inviscid fluid ($\nu = 0$), then the force balance reads

$$2\boldsymbol{\Omega} \times \mathbf{u} = -\frac{1}{\rho}\nabla p + \frac{1}{\rho}(\mathbf{J} \times \mathbf{B}) + \frac{\rho'}{\rho}g_e. \quad (4.46)$$

When integrated azimuthally over a cylindrical surface (4.46) reduces to

$$2\boldsymbol{\Omega} \int_{\Sigma} (\mathbf{u})_{\phi} d\Sigma = \int_{\Sigma} (j \times \mathbf{B})_{\phi} d\Sigma \quad (4.47)$$

with $d\Sigma = sd\phi dz$ and (s, ϕ, z) the cylindrical coordinates. The buoyancy force $\frac{\rho'}{\rho}g_e$ is equal to zero, because it acts only in meridional planes and has therefore no azimuthal component. The azimuthally integrated component of the pressure gradient force is also zero. Because of the continuity equation

$$\nabla \cdot \mathbf{u} = 0 \quad (4.48)$$

the left hand side of (4.47) is equal to zero

$$\int_{\Sigma} \mathbf{u} d\Sigma + \int_{N(s)} \mathbf{u} dS + \int_{S(s)} \mathbf{u} dS = \int \nabla \cdot \mathbf{u} dV = 0, \quad (4.49)$$

where $N(s)$ and $S(s)$ are the spherical caps of the cylinder as shown in figure (4.2) [Gubbins & Roberts, 1987]. There is no net–flow out or into the cylinder. Finally it remains

$$\int_{\Sigma} (\mathbf{J} \times \mathbf{B})_{\phi} d\Sigma = 0, \quad (4.50)$$

In order to have a velocity \mathbf{u} compatible with (4.1), (4.46) and (4.48), then it is necessary for the magnetic field of a slow and inviscid rotating fluid in a rigid spherical geometry to satisfy (4.50). This is Taylor's constraint. A further implication of (4.50) is, that the coupling between the annular cylinders co–axial with the rotation axis must vanish. Recent studies suggest that the geodynamo is currently oscillating around its Taylor state [Zatman & Bloxham, 1997, 1998; Bloxham et al., 2002], where the azimuthal components of the Lorentz force integrated over the cylinder surface vanishes, except the part involved in torsional oscillation. In order to excite torsional oscillation the geodynamo must have departed from its Taylor state. Jault & Le Mouél [1989]; Jault et al. [1996] showed that topographic and gravitational coupling³ between the core and the mantle lead to this departure from the Taylor state and excite motions in cylindrical annuli of the type

$$\mathbf{u}_G = \mathbf{u}_{\phi}(s)\hat{\phi}. \quad (4.51)$$

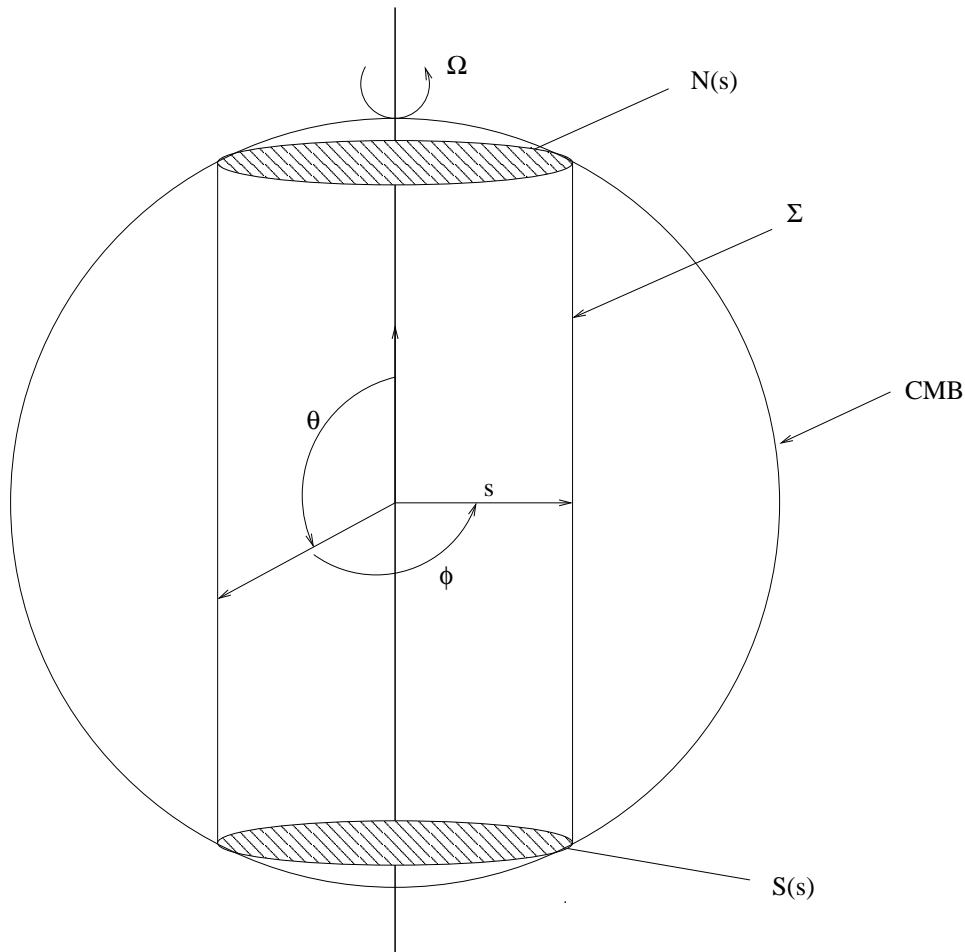


Figure 4.2: Sketch of the core geometry to illustrate the Taylor constraint

The fluid motion (4.51) will distort the magnetic field lines, causing a curvature to the field lines. The curvature generates a Lorentz force on the fluid which counteracts further curvature as predicted by Lenz's law and reverses the direction of the fluid flow. The field lines return to the undistorted configuration and beyond until the Lorentz force becomes strong enough again to stop fluid motion and to reverse it. Once the oscillations are initiated, they are unaffected by the toroidal field, and only the component perpendicular to the rotation axis, B_s , determines the restoring force and the period of torsional oscillation. A range of periods between 60 years [Braginskii, 1970] and 25 years [Gubbins & Roberts,

³Topographical coupling is due to dynamical pressure variation acting on an aspherical CMB [Hide, 1969], whereas gravitational coupling is due to the action of an aspherical geoid acting on density inhomogeneities in the core.

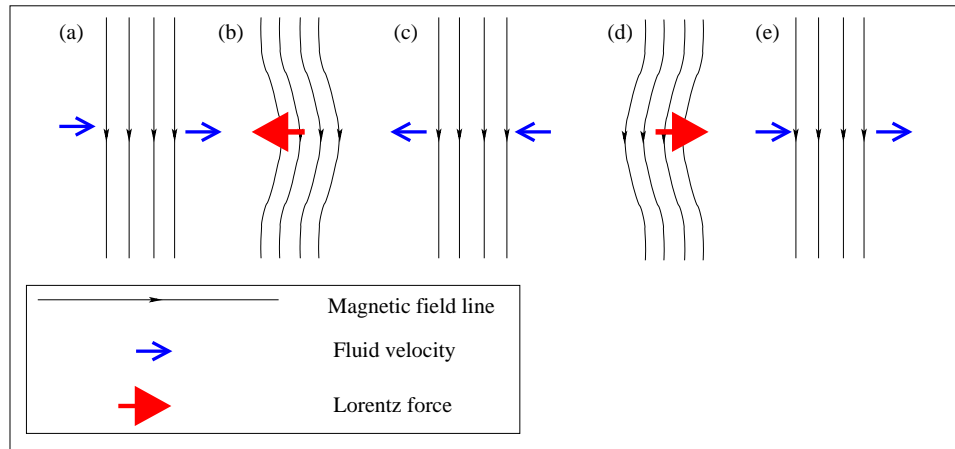


Figure 4.3: Figure shows the excitation mechanism of Alfvén like waves, such as torsional oscillation. Courtesy of C. Finlay

1987] has been suggested depending on the assumed strength of B_s in

$$T \simeq \frac{2\mu_0\rho\lambda}{B_s^2} \quad (4.52)$$

where λ is the wavelength, $B_s = 5\text{mT}$ [Gubbins & Roberts, 1987]. Without ohmic dissipation or viscosity these oscillations are undamped. Figure (4.3) depicts a complete cycle of the action due to the competing inertial force and Lorentz force [Finlay, 2004a].

The method of inversion for the flow motion is basically the same as outlined in section 4.1.4, the only distinction between these methods is the temporal damping of the toroidal components of the flow. Here the temporal damping of these components is relaxed and therefore the toroidal flow can more vary with time. Compared with Zatman & Bloxham [1997, 1998] and Bloxham et al. [2002] this approach is more general, but should recover the same behaviour of the fluid flow.

4.2 Maps of core–surface flows

In this section I compare the resulting flows derived using the different constraints outlined in the previous sections. First, I consider the maps based on the steady flow assumption and its extension in a azimuthally drifting reference frame, then the flows which based on tangential geostrophy are presented.

4.2.1 Steady flows

The steady flow for a single epoch was derived from triplets of the secular variation and the main field of the center epoch, i.e. 1990, and the adjacent epochs separated by five years, i.e 1985 and 1995. The figure 4.4 show the steady flows centering on the epochs 1985, 1990 and 1995. Similarities and differences are evident, all graphs show a pronounced westward drift. All figures show flows across the equator, most clearly around 1985 and 1995 near South America and 1985 near Indonesia. In at least two of the figures, namely for 1990 and 1995, a big circulation is apparent southeast of Africa. Also a strong circulation seems to have existed in 1985 underneath Indonesia. This gyre is less clearly defined in 1990 and has disappeared in 1995.

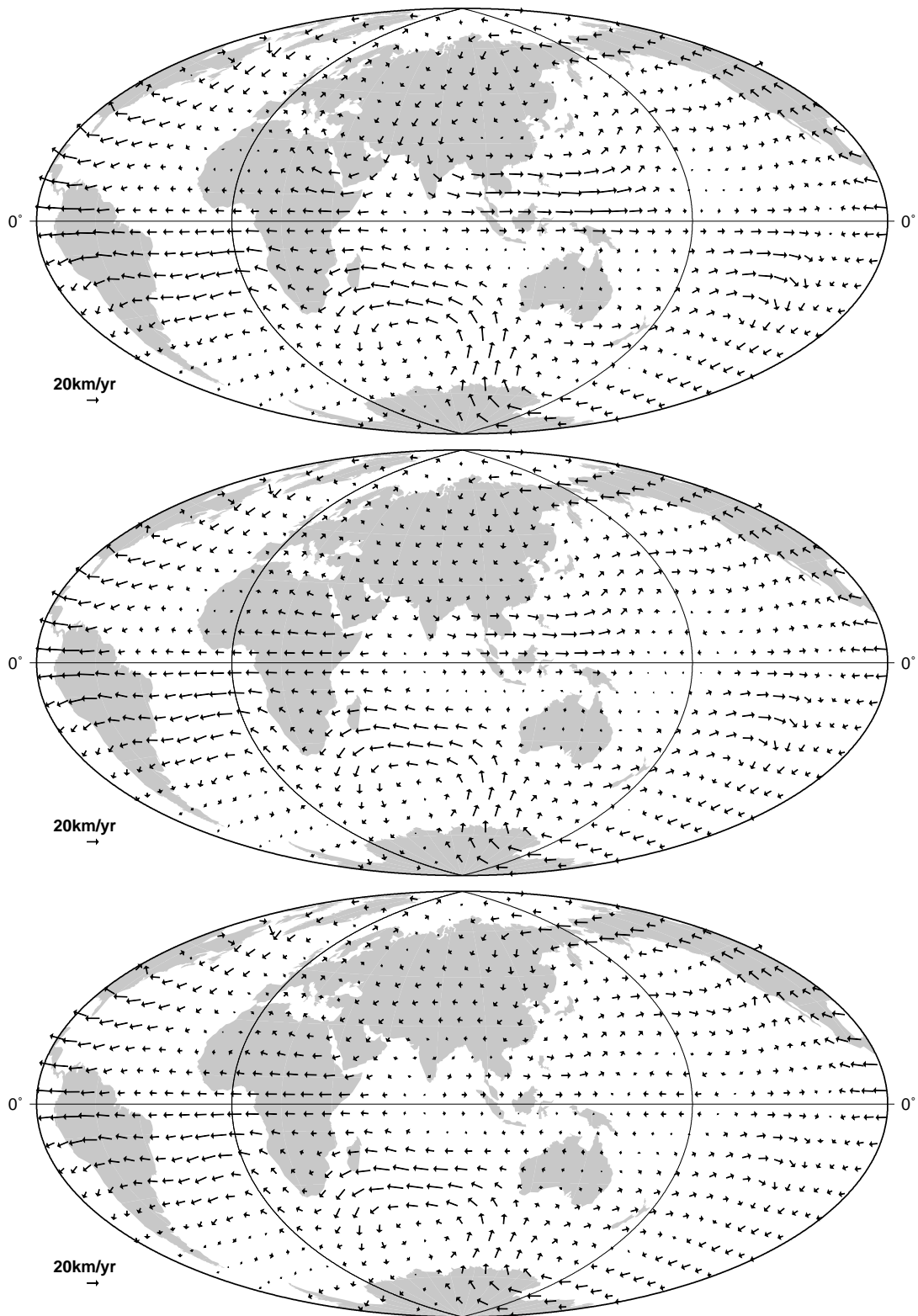


Figure 4.4: Steady flows centered on 1985, 1990 and 1995. The vectors show the velocity and direction of the fluid motion at the CMB.

4.2.2 Steady flows in an azimuthally drifting reference frame

The first finding of the examination of solutions for different damping parameters λ_v is shown in figure 4.5. The curves of the objective function differ for different λ_v . The minimum for strong damping coincide with a drift rate of approximately -10 km/yr, which is in a good agreement with the known value of the westward drift. Two further minima appear, when the damping is relaxed. One for -60 km/yr and an other for 49 km/yr, what would correspond to a westward drift and eastward drift, respectively. The appearance

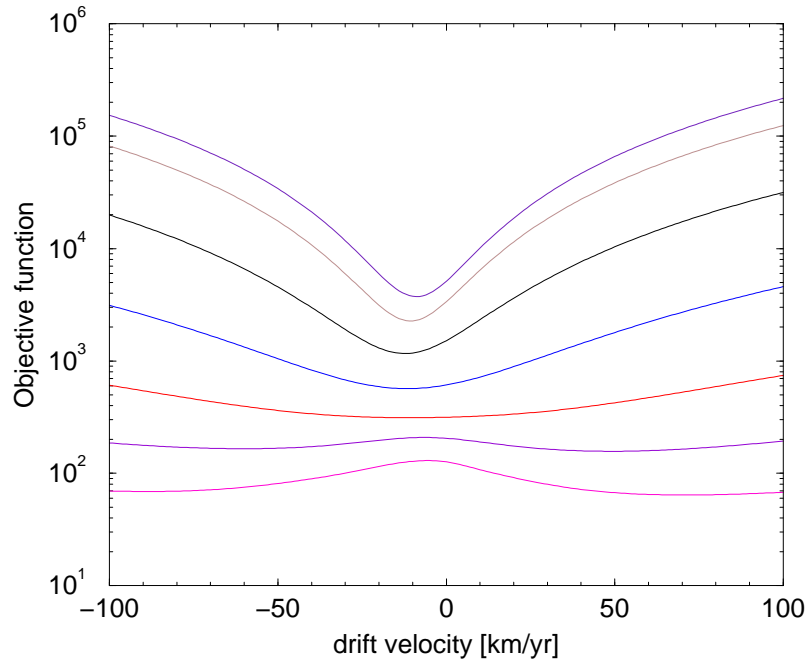


Figure 4.5: Objective function as a function of drift rate for different damping parameters λ_v .

of two solutions for the drift rate, when the damping is relaxed, is not comprehensible at once. In fact Holme & Whaler [2001] argued that the two solutions are caused by flows drifting with nearly equal and opposite angular velocity so that

$$\begin{aligned}\mathbf{u}_1(\theta, \phi, t) &= \mathbf{u}'(\theta, \phi - \psi(t)) + r_c \frac{d\psi}{dt} \cos \theta \hat{\phi} \\ \mathbf{u}_2(\theta, \phi, t) &= \mathbf{u}''(\theta, \phi + \psi(t)) - r_c \frac{d\psi}{dt} \cos \theta \hat{\phi}.\end{aligned}$$

Any linear combination of the two flows will explain the secular variation. Possible scenarios could be that both flows represent two traveling waves making up a standing wave. But also two convection rolls, as inferred from the maps of the radial magnetic field (figure 3.7) in opponent rotation would give a possible explanation.

Three solutions were constructed for three uniform drift rates: one eastward centered on 49.0 km/yr and two westward centered on -10.81 or -60.0 km/yr, respectively. These three drift velocities correspond to the three minima found for the objective function (see figure 4.5). The diagnostics for the three flow solutions are given in table 4.1. The flows with the higher drift velocities tend to be more energetic than the one with the drift speed centered on -10.81 km/yr, also the fit of the slow drifting flow to the secular variation is poorer than for the two fast drifting flows. Figure C.1 shows the comparison of the first 18 secular variation coefficients from the time–dependent model and predicted by the three flow solutions. All three solutions show a distinct temporal behaviour, but have in common that the recovering of the short term secular variation is rather poor. In figure 4.6 maps

	W Drift (W1)	W Drift (W2)	E Drift (E1)
drift velocity (km/yr)	-10.81	-60.0	49.0
rms secular variation misfit (nT/yr)	4.43	2.91	2.77

Table 4.1: Diagnostics of the drifting flow.

of the drifting flow solution for weak damping and eastward drift is shown. The three top graphics represent snapshots for three different times (1980, 1990 and 2000) as observed in the mantle frame. These flows do not significantly from those of the steady flow (cf figure 4.4). The bottom graphic shows the flow as seen in the drifting frame, here the flow is dominated by the strong eastward drift of about 49 km/yr.

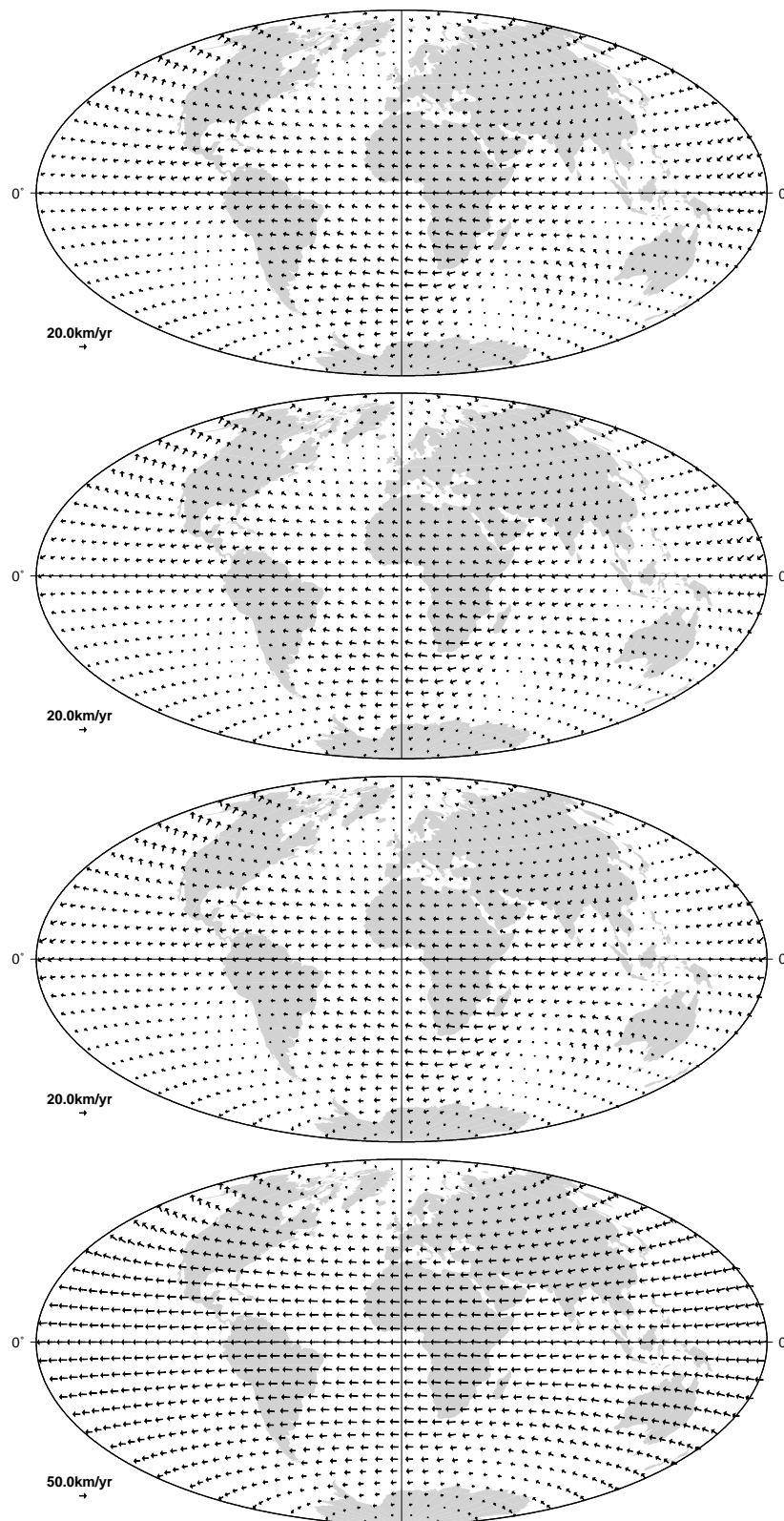


Figure 4.6: The three top maps show the drifting flows for 1980, 1990, and 2000 in the mantle frame. The bottom map shows the steady flow in the drifting reference frame.

4.2.3 Tangentially geostrophic flows and torsional oscillation

The solution is found as the knee point in the trade off curves between the averaged velocity of the flow and the secular variation misfit, as shown in figure 4.7. The trade off curves show very weak dependence of the temporal damping; therefore, the curves for strong $\lambda_t = 0.1\text{E}+03$, medium $\lambda_t = 0.1\text{E}-01$ and weak $\lambda_t = 0.1\text{E}-09$ temporal damping overlay. The preferred solution is obtained for strong temporal and geostrophic constrains

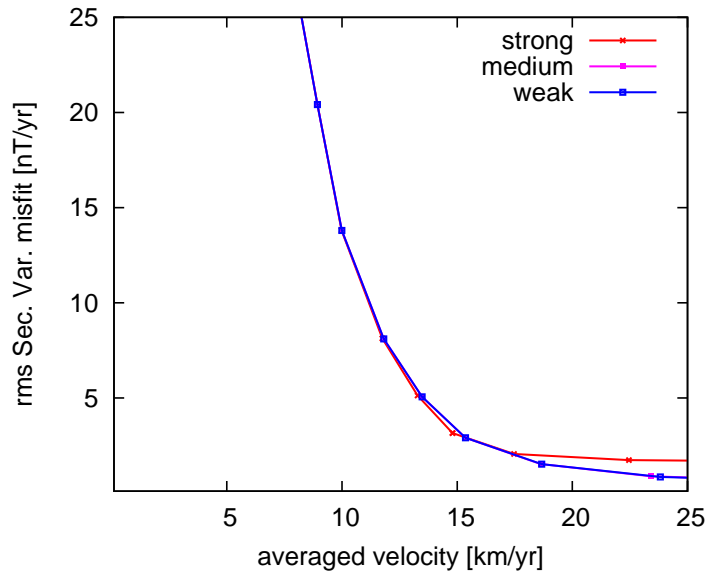


Figure 4.7: Trade off curves for three different temporal damping: strong $\lambda_t = 0.1\text{E}+03$, medium $\lambda_t = 0.1\text{E}-01$ and weak $\lambda_t = 0.1\text{E}-09$.

and referred to as flow 1 for the remainder of this study. Figure 4.8 shows the flow 1 for three different epochs.

The dominant features are a strong circulation southeast of Africa, a strong clockwise circulation centered underneath Labrador, strong westward directed flow in equatorial regions and weak flow in the Pacific region. The circulation centered southeast of Africa shows a rather complex structure and seems to be linked to a smaller gyre under the south Atlantic. Both gyres are parts of a much larger pattern in the southern hemisphere, which appears as a bending wave starting in east Antarctica and fades out across the south Pacific. All features are persistent during the 20 years interval. The ratio of the energy density of the equatorial symmetric and asymmetric flow components is 2.8; the flow is strongly equator symmetric.

The assumption of frozen flux and tangential geostrophy determine up and downwelling by

$$\nabla_h \cdot \mathbf{u}_h = \frac{\tan(\theta)}{c} u_\theta. \quad (4.53)$$

		Flow 1	Flow 2	Flow 3
Damping	spatial λ_s	2.0×10^{-4}	2.0×10^{-4}	2.0×10^{-4}
	temporal λ_t	1.0	1.0	1.0
	temporal λ_{tz} (for zonal terms)	-	-	$\times 10^{-3}$
Diagnostic	geostrophic norm	4.80×10^{-2}	220.09	4.80×10^{-2}
	spatial smoothness norm	15.57×10^6	1.01×10^6	15.57×10^6
	temporal smoothness norm	103.6	152.35	97.93
	time averaged velocity (km/yr)	15.33	11.44	15.33
	time averaged acceleration (km/yr ²)	2.87	3.48	2.90
	characteristic flow time (years)	5.34	3.28	5.28
	rms secular variation misfit (nT/yr)	0.80	1.49	2.91
	rms ang. mom. misfit	2.04	4.83	2.08

Table 4.2: Parameters and diagnostics of the inversions for two tangentially geostrophic flow and the flow invoking torsional oscillation.

Fluid up and downwelling is depicted in a color scale. This description seems to be insensitive for greater latitude and regions of fluid up and downwelling concentrate near the equator, where the geostrophic assumption is supposed to fail and therefore the magnitude of the upwelling cannot be given with high confidence. Nevertheless, it is worth noting that the strongest fluid up and down welling coincide with the regions, where the column rolls are expected from the analysis of the morphology of the radial field at the CMB (section 3.5.1).

Fluid upwelling is also to see in connection with magnetic diffusion, because the toroidal field is advected by fluid upwelling as sketched in figure 4.9. Upwelling results in a field concentration which is then twisted by a vertical velocity field. Finally, reconnection leads to magnetic diffusion of the field through the CMB.

As already mentioned, constraining the flow temporally does not have a significant effect on the solution itself, rather the tangentially geostrophic constraint controls the flow. Therefore a second solution, flow 2, is analysed, where the geostrophic constraint is relaxed by ten orders of magnitude. Relaxing the geostrophic constraint lets the ageostrophic part in the flow solution rise. Ageostrophy occurs, when the balance between pressure gradient and the Coriolis force is deranged. A perfect geostrophic balance would mean that the fluid motion is along lines of constant pressure, implicitly assuming that the tangential velocity with respect to the boundary is zero (4.38). This can only be achieved, when a thin viscous layer exists, the Ekman layer. The frictional drag F within this layer unbalances the geostrophic flow and generates an ageostrophic flow

$$2\boldsymbol{\Omega} \times \mathbf{u}_{ag} = F. \quad (4.54)$$

The imbalance deflects the flow towards lower pressure⁴. See figure 4.10. The maximum

⁴This phenomenon is also known from the Earth’s atmosphere, where the geostrophic wind feels the frictional drag of the rough underlying surface.

ageostrophic velocity never exceeds 3 km/yr, is strongest in the region of the geostrophic degeneracy (see figure 4.1) and crossing the equator. The direction of the friction, which can be deduced from this graph, is more or less symmetric to the equator and pointing either west or east.

A third flow solution (flow 3) is analysed, where only zonal components of the flow are allowed to vary with time. The maps of the torsional oscillation flow are shown in figure 4.12. The difference to flow 1 is insignificant. For comparison of the inversion parameters and characteristics of all three flows, see table 4.2. The results of an analysis of the time averaged velocity field is given in the table (4.3).

	Flow 1	Flow 2	Flow 3
total flow kinetic energy	210.90	145.97	210.96
toroidal component ¹	94.49	83.94	94.48
poloidal component ¹	5.51	16.06	5.52
symmetric component ¹	66.39	71.25	66.39
symmetric toroidal component ²	98.73	89.93	98.73
symmetric poloidal component ²	1.27	10.07	1.27
asymmetric component ¹	33.61	28.75	33.61
asymmetric toroidal component ³	86.13	69.08	86.10
asymmetric poloidal component ³	13.87	30.92	13.90
geostrophic component ¹	99.96	75.05	99.96
ageostrophic component ¹	0.03	24.94	0.03
zonal toroidal component ¹	16.12	38.22	16.13

Table 4.3: Characteristics of the two tangentially geostrophic flows and the flow invoking torsional oscillation. The total energy is given in arbitrary units and the components as percentage of the total flow (1) and the total symmetric component (2) and total asymmetric component (3), respectively.

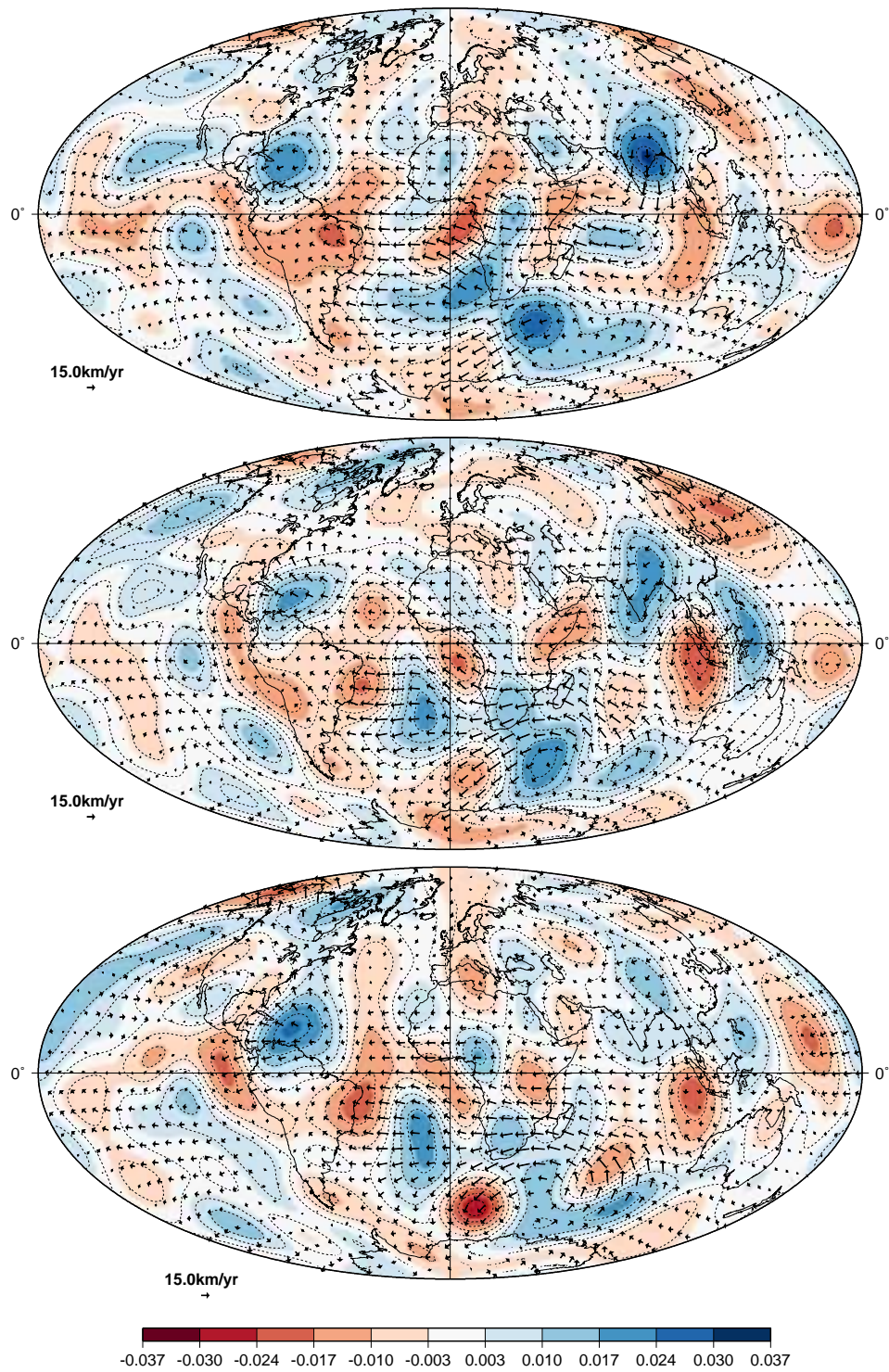


Figure 4.8: Tangentially geostrophic flows for 1980, 1990 and 2000. The vectors show the velocity and direction of the fluid motion at the CMB. The color scale shows the intensity of the horizontal divergence (upwelling and downwelling) of the flow.

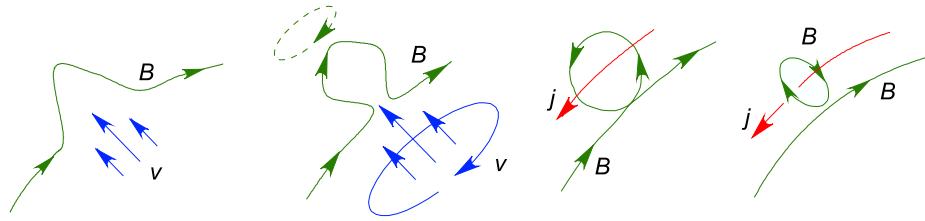


Figure 4.9: Sketch of the toroidal flux expulsion in an electrically conducting medium.

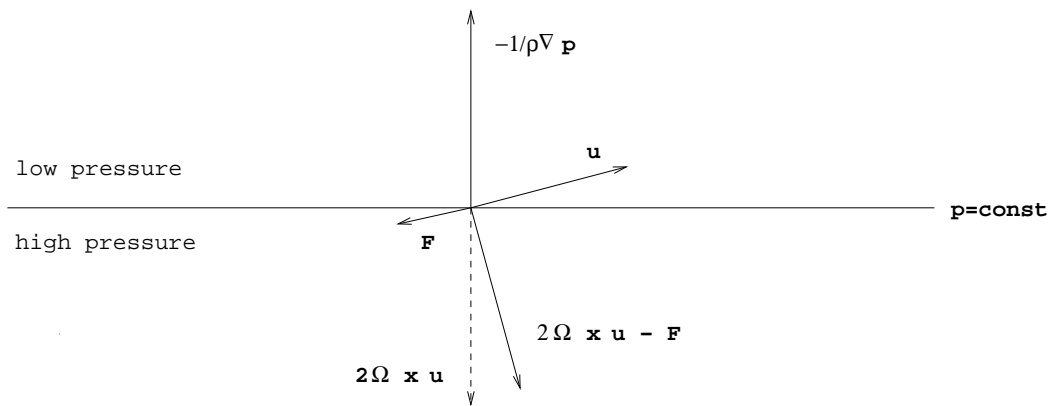


Figure 4.10: The ageostrophic force balance, where F is the frictional drag.

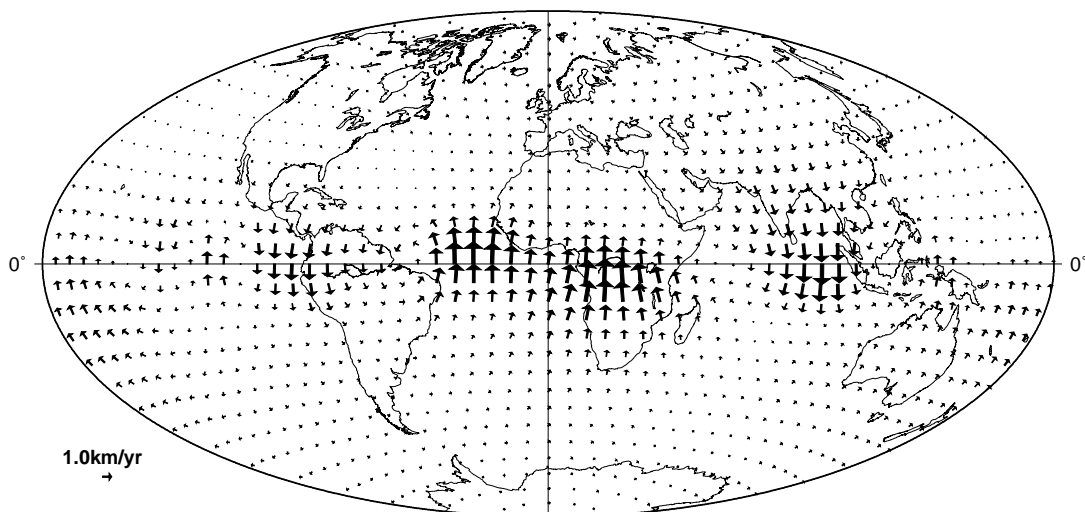


Figure 4.11: The ageostrophic part of the flow 2.

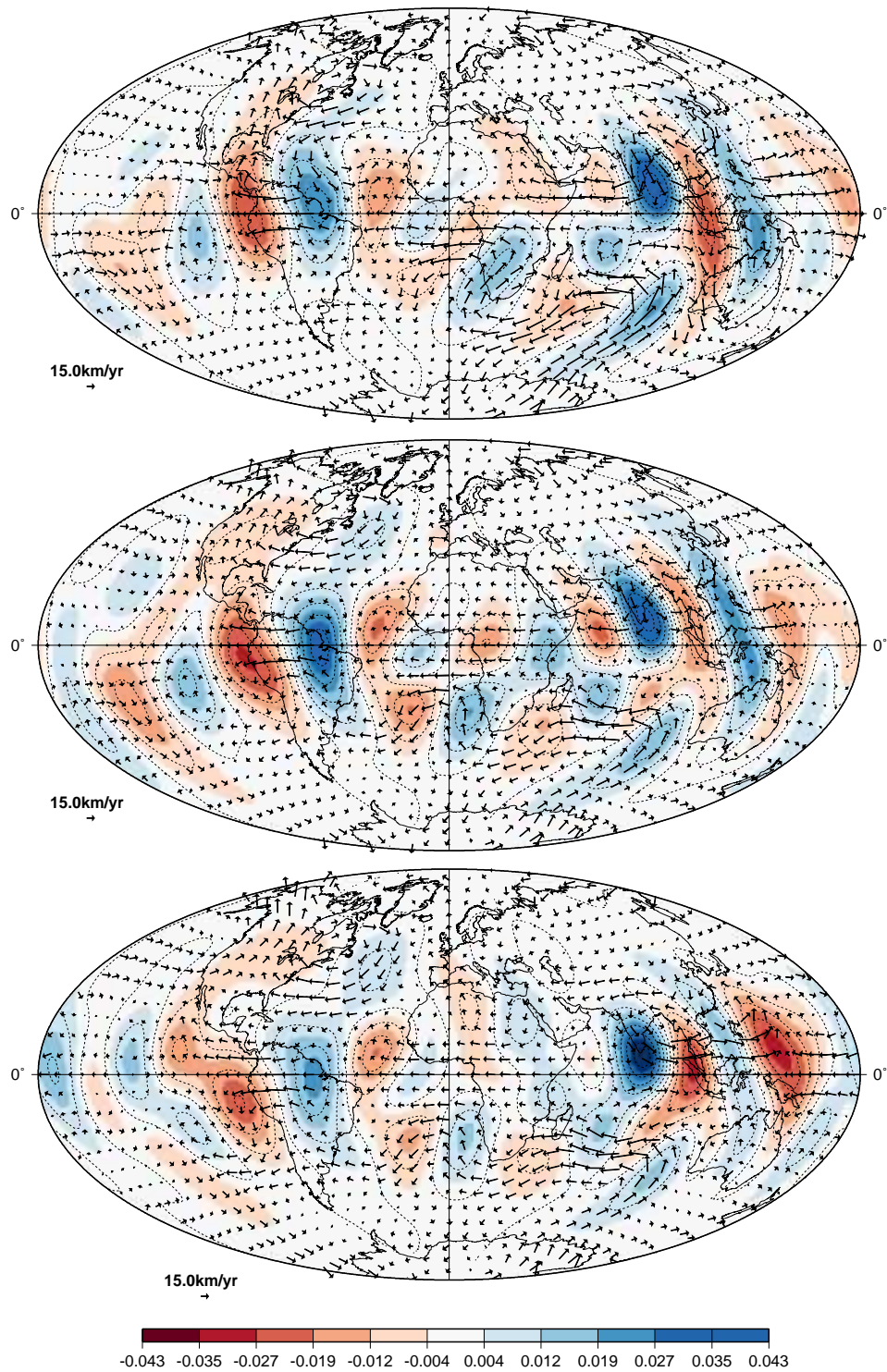


Figure 4.12: Torsional oscillation flows (flow 3) for 1980, 1990, and 2000. The vectors show the velocity and direction of the fluid motion at the CMB.

Like in chapter 3 a resolution analysis of the solutions is carried out. In figure 4.13 the resolution of the toroidal (left) and the poloidal velocity coefficients (right) are shown. The resolution is derived at the six times during 1980 and 2000. The resolution of the flow inversion is fairly time invariant, as the six curves overlay. Recalling, that low resolution means the model is controlled by the regularization or a priori beliefs, whereas high resolution states that the model is controlled by the data, i.e. the model for secular variation and the main field. The resolutions for toroidal and poloidal terms differ significantly, for the toroidal terms it is higher than for the poloidal ones. This appears to be expected from point of view, that the poloidal flow is more constrained by applying the tangentially geostrophic constraint. It becomes immediately clear, when considering the resolution of less tangential geostrophic constrained solution (figure 4.14). Here the resolution of the poloidal terms (right panel) is of the order of the resolution of the toroidal terms (left panel).

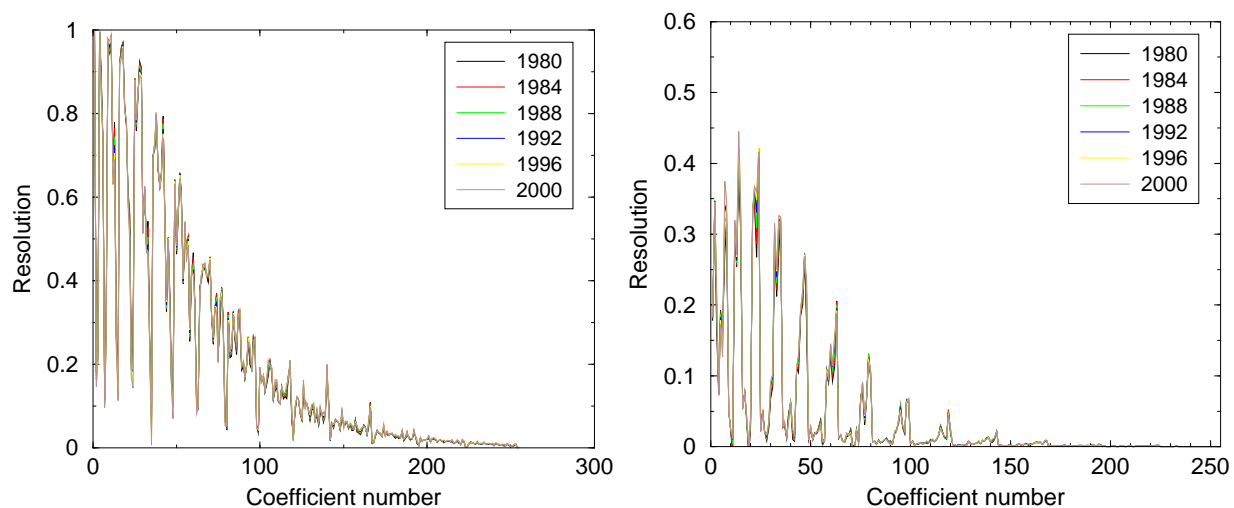


Figure 4.13: The resolution of the toroidal (left) and poloidal velocity coefficients (right) for flow 1.

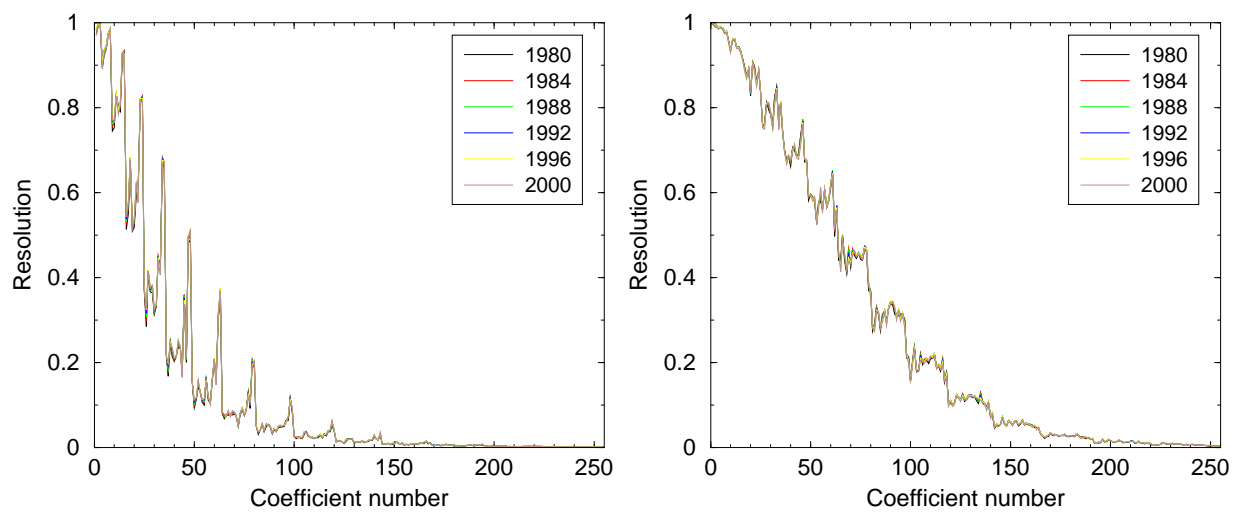


Figure 4.14: The resolution of the toroidal (left) and poloidal velocity coefficients (right) for flow 2.

4.2.4 Prediction of secular variation from flows

Figure 4.15 provides the fit of the secular variation predicted by different flow assumptions to that of the time–dependent model derived in the previous chapter. The overall impression is that flow 1, 2 and 3 recover the secular variation at all chosen stations fairly good. Table 4.2

The predictions by the drifting flow is rather poor. It captures only the gross features of the secular variation, but cannot account for the short term variation, i.e. jerks. However, this fact may help to evaluate possible explanation for geomagnetic jerks. The incapacity of the drifting flow to fit short term secular variation allows to different scenarios for the generation of short term secular variation: either jerks are related to flux expulsion or caused by non–equator symmetric flows.

I also tested the hypothesis if the secular variation can be attributed to a flow which is purely toroidal. This means that equation 4.7

$$\partial_t \mathbf{B}_r + \mathbf{B}_r \nabla_h \cdot \mathbf{u} + \mathbf{u} \cdot \nabla_h \mathbf{B}_r = 0$$

reduces to

$$\partial_t \mathbf{B}_r + \mathbf{u} \cdot \nabla_h \mathbf{B}_r = 0. \quad (4.55)$$

Toroidal flows are divergence free and confined to a spherical surface, i.e. there is no advection of toroidal field or upwelling of fluid flow.

Figure 4.15 allows a direct comparison of the secular variation prediction of the flows with the time–dependent model. All flows based on the tangential geostrophic assumption, flow 1 – 3, and the purely toroidal flow recover the secular variation and the jerks almost. Whereas, the drifting flow captures the secular variation roughly, without explaining short term variations. Figure C.1 in the appendix shows a comparison of the first 15 coefficients of the secular variation derived from different drifting flows.

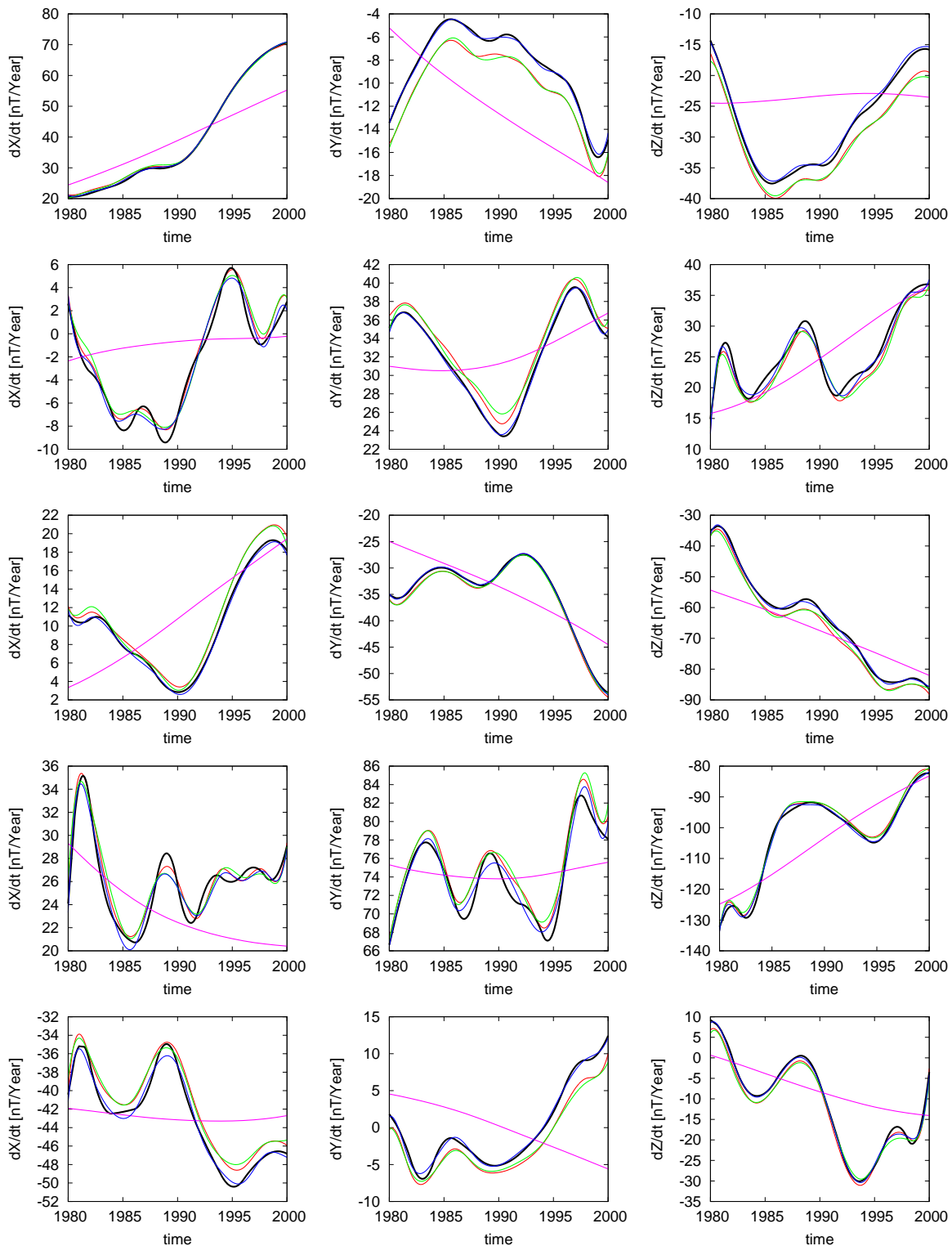


Figure 4.15: Comparison of modeled secular variation (solid black line) to the secular variation estimates at selected permanent observatories. Red curves are the prediction of flow 1, of flow 3 (green curves) and of the purely toroidal flow (blue curves). The pink curves are the prediction by the drifting flow (E1). From left to right: dX/dt , dY/dt , dZ/dt . From top to bottom: Resolute Bay (Canada), Niemegk (Germany), Newport (USA), MBour (Senegal), Pamatai (French Polynesian).

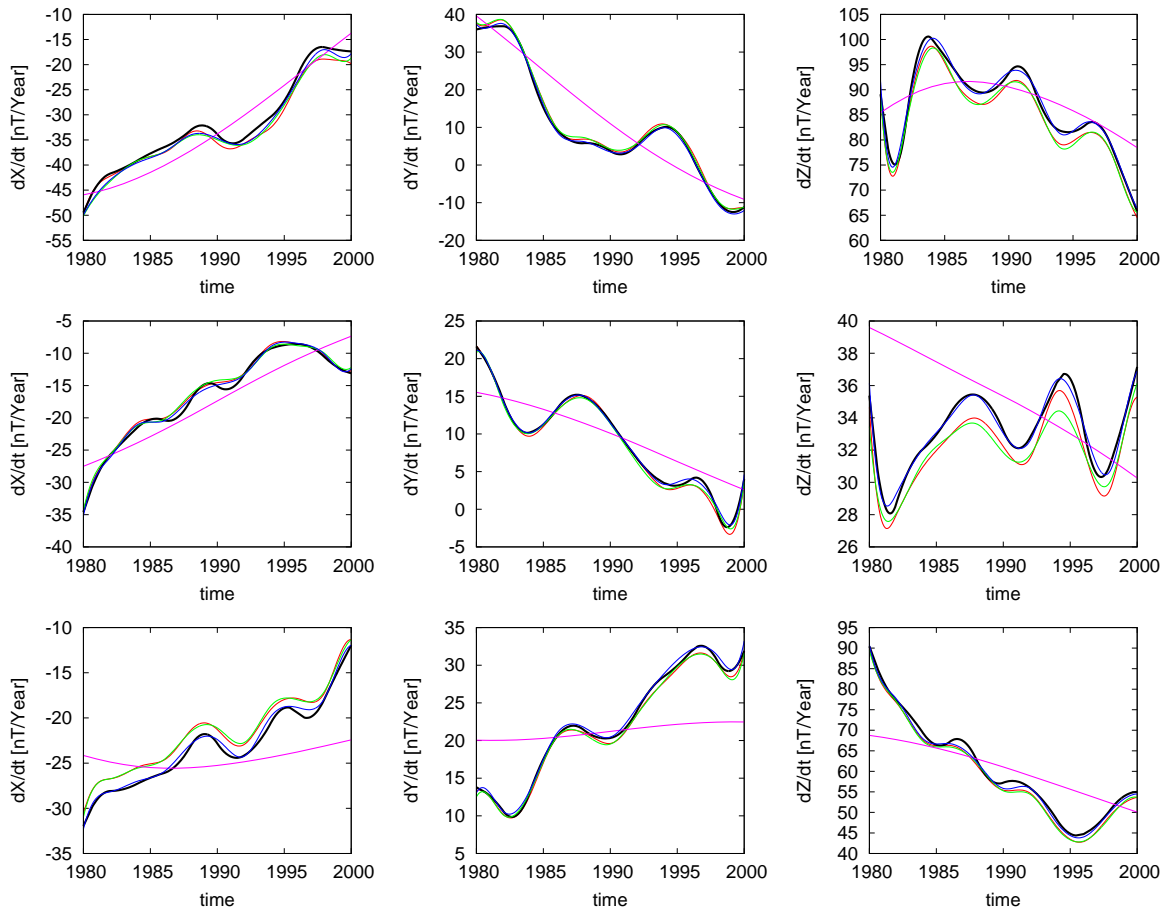


Figure 4.15: (*continued from previous page*) From top to bottom: Hermanus (South Africa), Eyrewell (New Zealand) and Scott Base (Antarctica).

4.2.5 Prediction of the decadal change of length of day

The Earth’s rotation rate varies with periods ranging from a few days to at least a few thousand years. Several geophysical processes affecting the Earth’s rotation rate: exchanges of angular momentum between solid Earth and either the atmosphere or oceans, tidal friction in the gravitational Earth–Moon–Sun system, seasonal exchange of angular momentum due to foliation and glaciation, or changes in the moment of inertia of the mantle due to post-glacial rebound. It is widely accepted that between core and mantle angular momentum is exchanged via a coupling mechanism [Hide & Dickey, 1991]. Because angular momentum is conserved an increase in the mantle rotation rate is associated with a slowing down of the core and vice versa.

Small differences between universal time (UT) and ephemeris time (ET) can be measured through astronomical observations, e. g., the time of lunar occultation of a star can be predicted to a high accuracy. Small changes in the Earth rotation rate cause discrepancies between the predicted time and the actual time, this time lag can directly be translated into a sidereal displacement angle ψ . ψ defines the relative position of the Earth to the stars. The first time derivative is the variation in the length of day (LOD)

$$\Lambda = \frac{d\psi}{dt}, \quad (4.56)$$

what is equivalent to the angular momentum

$$L = I \times \Lambda, \quad (4.57)$$

where I_M is the moment of inertia. The second time derivative is the observed torque on the mantle

$$\Gamma = I \frac{d^2\psi}{dt^2}, \quad (4.58)$$

Now the intention is to show how core surface motion can account for a small portion of Λ , when all other known contributions were removed. The basic idea is that the magnetic, inviscid, rotating fluid of the outer core interacts with solid lower most mantle via coupling. After rejecting viscous coupling as too weak [Rochester, 1984], three possible coupling mechanism remain. Mass anomalies and an aspherical shape of the core–mantle boundary region cause a non-radial component of gravity which might exchange angular momentum and generate a torque from the core to the mantle [Jault & Le Mouél, 1989]. These mass anomalies which directly translate into density heterogeneities are below seismic resolution, so this hypothesis cannot be tested directly. A further mechanism, which was explored in detail by Stix & Roberts [1984] and Holme [1998a,b, 2000], relies on the interaction of the induced currents in the lower most mantle with the magnetic field of the core to produce Lorentz torques. Another coupling mechanism was proposed by Hide [1969], which bases on assumptions about torques exerted by topographic coupling between core and mantle. Because of the high non–uniqueness of the torque calculation the form of coupling is still controversial.

The estimation of the core angular momentum is much simpler, it requires only that the surface flow matches the bulk flow on cylinders. The estimations follow directly from tangentially geostrophy of the flow.

$$\begin{aligned}\mathbf{u}_G &= \mathbf{u}_\phi(s)\hat{\phi} \\ &= -\mathbf{r} \times \nabla \left(\sum_{l=1}^{\infty} \sum_{m=0}^l t_l^m P_l^m \cos(\theta) \right)\end{aligned}$$

It can be shown [Jault et al., 1988; Jackson et al., 1993] that the angular momentum as measured in the mantle rest frame is given by

$$L = \frac{8\pi}{15} c^4 \rho \left(t_1^0 + \frac{12}{7} t_3^0 \right) \quad (4.59)$$

and the change in the length of day can be predicted by

$$\Lambda = 1.138 \left(t_1^0 + \frac{12}{7} t_3^0 \right) [\text{ms}]. \quad (4.60)$$

The calculations by Jault et al. [1988] were made on the assumptions that all of the toroidal zonal flow was in the mode \mathbf{u}_G by imposing symmetry about the equator on the calculations; requiring all terms $t_{2n}^0 = 0$ for $n \geq 1$. Jackson et al. [1993] relaxed this requirement, by postulate that angular momentum changes associated with the background convection and therefore the even toroidal zonal modes are small.

Figure 4.16 shows the change in the length of day deduced from astronomical measurement taken from Holme & de Viron [2005]. It also shows the predictions from the tangentially geostrophic flow without or with invoking torsional oscillation following from (4.60). The vertical offset is varied arbitrary to enable a clear distinction of the results for each flow type. The prediction from the drifting flow varies as the descending straight line and is not shown. Generally, the slope of Λ of the flow prediction is much steeper than the actual Λ , this agree well with [Holme & Olsen, 2005]. The green line shows the prediction of a flow, when the geostrophic constraint is relaxed.

Figure (4.17) depicts the averaged zonal velocities of the tangential geostrophic flow 1 and 2 at three dates. It is clearly visible that flow 2 shows significant variation in the zonal velocity and a equator-asymmetric state, which may explain the poor fit to the observed Λ (c.f. figure 4.17). The averaged zonal velocities of flow 1 are nearly symmetric to the equator.

4.3 Discussion and Conclusion

In this chapter the time–dependent model of the main field and its secular variation (developed in chapter 3) are treated as data, to invert the radial induction equation for different types of flows. Therefore, I have adopted the frozen flux hypothesis which ascribes the observed secular variation entirely to the effects of advection.

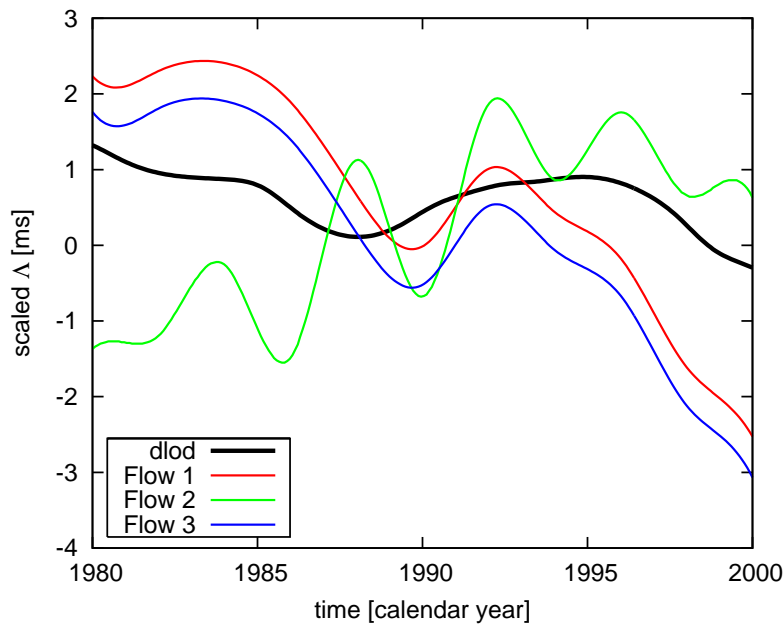


Figure 4.16: Comparison of Λ prediction. The black represent the Λ taken from Holme & de Viron [2005]. The colored curves are the predictions from the flows accordingly to the legend in the lower left corner.

The maps of steady flows and the drifting flow show less features than the maps of the flows 1 and 2, but all maps of all flows show a gyre south east of Africa and a feature underneath Labrador during the 20 years period.

It had been demonstrated that flows based on the tangential geostrophic assumption can explain almost of the observed secular variation and the change of the length of day. But, also a purely toroidal flow confined to a spherical surface, with no fluid upwelling and advection of toroidal field explains the secular variation equally well. The resolution analysis suggests that the poloidal component of flow 1 is mostly determined by the tangential geostrophic assumption. A relaxation of the tangential geostrophic constraint leads to a better fitting of the secular variation on one side, but on the other side the fit to Λ worsens (see table 4.2). This allow the conclusion that the poloidal component of the flow is less important for the generation of secular variation.

A second class of flow assumption as outlined in the first part of this chapter. Unlike the geostrophic flows, which are based on the dynamic description of the secular variation generation (i.e. Navier–Stokes equation), the steady flow assumption is a kinematic analysis of this. The steady flow assumption provides formal uniqueness for the inversion of the diffusion-less radial induction equation, but by definition a time–dependency of the solution is impossible. To introduce time–dependency to steady flow is therefore highly motivated. In fact, a steady flow in an azimuthally drifting reference frame improves the fit to the secular variation compared with single epoch steady flow. But it is still unable to explain

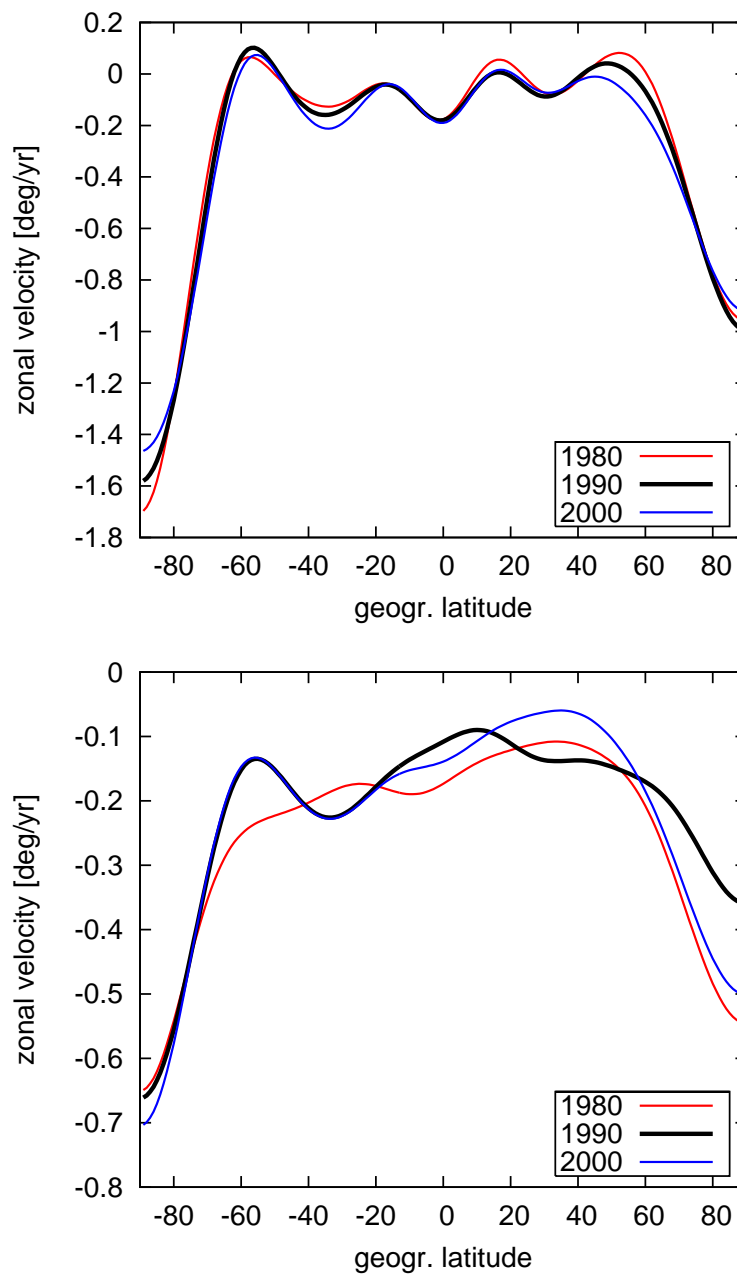


Figure 4.17: The zonal velocity profile for the epochs 1980, 1990, and 2000, derived from flow 1 (top) and flow 2 (bottom).

geomagnetic jerks in terms of generation by flows. Nevertheless, the drifting flow allows that the remaining signal might be explained by diffusion, whereas tangential geostrophic flows suggest that diffusion is unimportant.

The author is inclined to assume that geomagnetic jerks could be explained in terms of sudden flux expulsion, resulting in magnetic diffusion and a current in the lower most

mantle (see figure 4.9). The sudden appearance of currents may causes sudden acceleration or deceleration of the core, because a current system in the lower most mantle between regions of flux expulsion leads to an exchange of angular momentum form the core to the mantle. At the minute this is a speculation and needs to be proven and quantified.

Chapter 5

Conclusion and Prospects

The research outlined in this thesis has focused on one major topic, a description of the secular variation of the Earth's magnetic field during 1980 and 2000. Of particular interests were the geomagnetic jerks occurred in this time interval. The endpoints of the time interval were chosen, because of the availability of high quality satellite field models for this epochs. In 1980 a model from MAGSAT and in 2000 from CHAMP and ØRSTED facilitated a spatially high resolved sampling of the Earth's magnetic field. The models derived from these satellite data were used to constrain the time-dependent model of the main field and its secular variation at these epochs. The time-dependent model, which is now named as P-UFM1, was set up by using secular variation estimates of geomagnetic observatories monthly means and repeat station data. The clear advantage of secular variation estimates lies in the fact that these data are unbiased by the crustal field. The figure depicts the

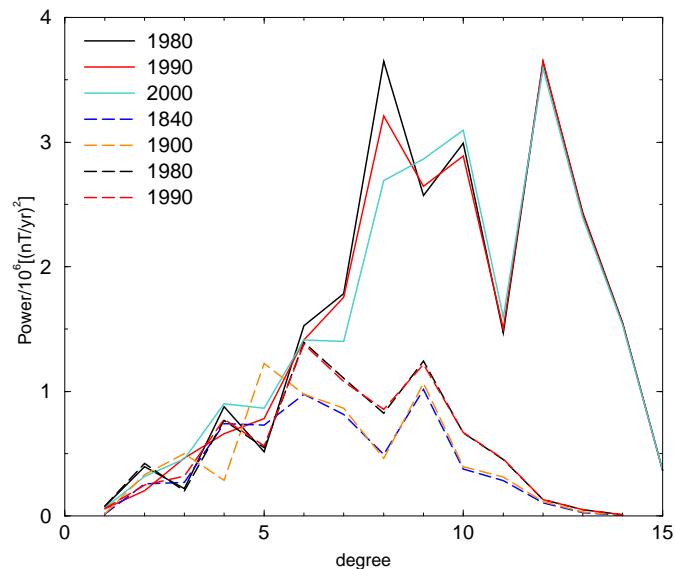


Figure 5.1: Mauersberger–Lowes spectra of the secular variation at the CMB of the *GUFM* (dashed lines) and of the P-UFM1 (solid lines).

Mauersberger–Lowes spectra (as given in (5.1)) of the P-UFM1 and *GUFM*. It clearly shows that the spatial power (and therefore the resolution) of the P-UFM1 is about a factor 2 higher than for the *GUFM*. This figure is crucial it clarifies the additional model content that the method brings.

$$\langle \mathbf{B}^2 \rangle = \sum_{l=1}^{\infty} \left(\frac{a}{c}\right)^{2l+4} (l+1) \sum_{m=0}^l (\dot{g}_l^{m2} + \dot{h}_l^{m2}) \quad (5.1)$$

The individual spectra of P-UFM1 overlap from degree 10 onward and are equivalent with a linear interpolation of the two endpoint models. The degree 9 and greater of the *GUFM* are obviously affected by the damping, and the spectral peak at degree 12, which is present in the spectra of the P-UFM1, is not resolved anymore.

The main results of this study are:

1. A valuable extension of the hitherto existing time–dependent description of the secular variation, where the new model, the P-UFM1 shows a higher spatial and temporal resolution.
2. The model of the morphology of the radial field at the core–mantle boundary suggests the existence of two columnar rolls, which are linked to the geodynamo.
3. Further, the model provides a useful test of the frozen flux hypothesis.
4. This new model admit a inversion for core–surface flows and a hypothesis testing for the secular variation generation.
5. The flow models predict the secular variation and the length of the day predictions shows the correct sign for the trend, but two large an amplitude.
6. The causing of geomagnetic jerks is still not understood, but I tried to explain these features to be tightly linked to flux expulsion, which definitively occurred in the last 20 years.

The last point is certainly the one most capable of development, and in fact several lines of deployment are possible. One may be the invocation of diffusion in the inversion for core–surface flows as proposed by Gubbins [1996]. If jerks and diffusion are connected to each other, than this approach should certainly improve the drifting flow or a somehow time–dependent steady flow. This work was done in the hope to provide some new aspects about the processes at the core–mantle boundary.

Bibliography

- Alexandrescu, M., Gibert, D., Hulot, G., Le Mouél, J., & Saracco, G., 1996. Worldwide wavelet analysis of geomagnetic jerks, *J. geophys. Res.*, **101**, 21975–21994.
- Alfvén, H., 1942. On the existence of electromagnetic-hydromagnetic waves, *Arkiv. Mat. Astron. Fys.*, **29(B)2**, 1–7.
- Allredge, L. R., 1977. Geomagnetic variations with periods from 13 to 30 years, *J. Geomag. Geoelectr.*, **29**, 123–135.
- Allredge, L. R., 1984. A discussion of impulses and jerks in the geomagnetic field, *J. geophys. Res.*, **89**, 4403–4412.
- Backus, G., Parker, R., & Constable, C., 1996. *Foundations of Geomagnetism*, Cambridge University Press.
- Backus, G. E., 1968. Kinematics of geomagnetic secular variation in a perfectly conducting core, *Philos. Trans. R. Soc. London A*, **263**, 239–266.
- Backus, G. E., 1970. Non-uniqueness of the external geomagnetic field determined by surface intensity measurements, *J. geophys. Res.*, **75**, 6337–6341.
- Backus, G. E., 1988. Bayesian inference in geomagnetism, *Geophys. J.*, **92**, 125–142.
- Backus, G. E. & Gilbert, F., 1967. Numerical applications of a formalism for geophysical inverse problems, *Geophys. J. R. astr. Soc.*, **13**, 247–276.
- Backus, G. E. & Gilbert, F., 1968. The resolving power of gross Earth data, *Geophys. J. R. astr. Soc.*, **16**, 169–205.
- Backus, G. E. & Le Mouél, J.-L., 1986. The region on the core-mantle boundary where a geostrophic velocity field can be determined from frozen flux magnetic data, *Geophys. J. R. astr. Soc.*, **85**, 617–628.
- Backus, G. E., Estes, R. H., Chinn, D., & Langel, R. A., 1987. Comparing the jerk with other global models of the geomagnetic field from 1960 to 1978, *J. geophys. Res.*, **92**, 3615–3622.

- Banks, R. J., 1969. Geomagnetic variations and the conductivity of the upper mantle, *Geophys. J. R. astr. Soc.*, **17**, 457–487.
- Bloxham, J., 1986. The expulsion of magnetic flux from the Earth's core, *Geophys. J. R. astr. Soc.*, **87**, 669–678.
- Bloxham, J., 1987. Simultaneous stochastic inversion for geomagnetic main field and secular variation. I. a large-scale inverse problem, *J. geophys. Res.*, **92**, 11,597–11,608.
- Bloxham, J., 1988. The determination of fluid flow at the core surface from geomagnetic observations, in *Mathematical Geophysics, A Survey of Recent Developments in Seismology and Geodynamics*, edited by N. J. Vlaar, G. Nolet, M. J. R. Wortel, & S. A. P. L. Cloetingh, Reidel, Dordrecht.
- Bloxham, J. & Gubbins, D., 1986. Geomagnetic field analysis. IV - Testing the frozen-flux hypothesis, *Geophys. J.*, **84**, 139–152.
- Bloxham, J. & Jackson, A., 1989. Simultaneous stochastic inversion for geomagnetic main field and secular variation II: 1820–1980, *J. geophys. Res.*, **94**, 15,753–15,769.
- Bloxham, J. & Jackson, A., 1992. Time-dependent mapping of the magnetic field at the core-mantle boundary, *J. geophys. Res.*, **97**, 19,537–19,563.
- Bloxham, J., Gubbins, D., & Jackson, A., 1989. Geomagnetic secular variation, *Philos. Trans. R. Soc. London A*, **329**, 415–502.
- Bloxham, J., Dumberry, M., & Zatman, S., 2002. The origin of geomagnetic jerks, *Nature*, **420**, 65–68.
- Box, G. E. P. & Jenkins, G. M., 1976. *Time Series Analysis, Forecasting and Control*, Holden Day, San Fransisco.
- Braginskii, S. I., 1970. Torsional magnetohydrodynamic vibrations in the Earth's core and variations in day length, *Geomag. and Aeronomy (English translation)*, **10**, 1–8.
- Braginskii, S. I., 1984. Short-period geomagnetic secular variation, *Geophys. Astrophys. Fluid Dyn.*, **30**, 1–78.
- Brillinger, D. R., 1981. *Time series: Data analysis and Theory*, Holden Day, San Fransisco.
- Brunhes, B., 1906. Recherches sur la direction d'aimentation des roches volcaniques, *J. Physique*, **5**, 705–724.
- Bullard, E. C. & Gellman, H., 1954. Homogeneous dynamos and terrestrial magnetism, *Philos. Trans. R. Soc. London A*, **247**, 213–278.
- Busse, F. H., 1970. Thermal instabilities in rapidly rotating systems, *J. Fluid Mech.*, **44**, 441–460.

- Cain, J. C., Daniels, W. E., Hendricks, S. J., & Jensen, D. C., 1965. An evaluation of the main geomagnetic field, 1940-1962, *J. geophys. Res.*, **70**, 3647–3674.
- Cain, J. C., Wang, Z., Kluth, C., & Schmitz, D. R., 1989. Derivation of a geomagnetic model to $n = 63$, *Geophys. J.*, **97**, 431–441.
- Carrigan, C. R. & Busse, F. H., 1983. An experimental and theoretical investigation of the onset of convection in rotating spherical shells, *J. Fluid Mech.*, **126**, 287–305.
- Chapman, S. & Bartels, J., 1940. *Geomagnetism*, Oxford University Press.
- Chulliat, A. & Hulot, G., 2000. Local computation of the geostrophic pressure at the top of the core, *Phys. Earth Planet. Inter.*, **117**, 309–328.
- Chulliat, A. & Hulot, G., 2001. Geomagnetic secular variation generated by a tangentially geostrophic flow under the frozen-flux assumption-I. Necessary conditions, *Geophys. J. Int.*, **147**, 237–246.
- Conradsen, K. & Spliid, H., 1981. A seasonal adjustment filter for use in Box Jenkins analyses of seasonal time series, *Applied Statistics*, **30**, 172–177.
- Courtillot, V., Ducruix, J., & Le Mouél, J.-L., 1978. Sur une accélération récente de la variation séculaire du champ magnétique terrestre, *C. R. Acad. Sci. Paris. Ser. D*, **287**, 1095–1098.
- Currie, R. G., 1966. The geomagnetic spectrum – 40 days to 5.5 years, *J. geophys. Res.*, **71**, 4579–4598.
- Currie, R. G., 1973. Fine structure in the sunspot spectrum - 2 to 70 years, *Astrophysics and Space Science*, **20**, 509–+.
- Currie, R. G., 1976. Long period magnetic activity - 2 to 100 years, *Astrophysics and Space Science*, **39**, 251–254.
- Davis, R. G. & Whaler, K. A., 1996. Determination of a steady velocity in a rotating frame of reference at the surface of the Earth's core, *Geophys. J. Int.*, **126**, 92–100.
- Davis, R. G. & Whaler, K. A., 1997. The 1969 geomagnetic impulse and spin-up of the earth's liquid core, *Phys. Earth Planet. Int.*, **103**, 181–194.
- Delouis, H. & Mayaud, P. N., 1975. Spectral analysis of the geomagnetic activity index AA over a 103-year interval, *J. geophys. Res.*, **80**, 4681–4688.
- Dowson, M. J., Buckingham, J. P., & Simmons, D. A., 1987. Notes on geomagnetic repeat measurements at Grytviken, April 1987, *Br. Antarc. S. Bull.*, **71**, 49–52.
- Fearn, D. R., 1998. Hydromagnetic flow in planetary cores, *Reports of Progress in Physics*, **61**, 175–235.

- Finlay, C. C., 2004. Alfvén waves, in *Encyclopaedia of Geomagnetism and Paleomagnetism*, edited by D. Gubbins & E. Herrero-Bervera, Earth Science Series, Kluwer Academic Publishers, In preparation.
- Finlay, C. C., 2004. MAC waves, in *Encyclopaedia of Geomagnetism and Paleomagnetism*, edited by D. Gubbins & E. Herrero-Bervera, Earth Science Series, Kluwer Academic Publishers, In preparation.
- Finlay, C. C. & Jackson, A., 2003. Equatorially dominated magnetic field change at the surface of Earth's core, *Science*, **300**, 2084–2086.
- Franklin, J. N., 1970. Well-posed stochastic extension of ill-posed problems, *Geophys. J. R. astr. Soc.*, **23**, 125–128.
- Fraser-Smith, A. C., 1972. Spectrum of the geomagnetic activity index Ap, *J. geophys. Res.*, **77**, 4209–4220.
- Gauss, C. F., 1839. Allgemeine theorie des erdmagnetismus, in *Resultate aus den Beobachtungen des magnetischen Vereins im Jahre 1838*, edited by C. F. Gauss & W. Weber, pp. 1–57, Leipzig.
- Gavoret, J., Gibert, D., Menvielle, M., & Le Mouél, J.-L., 1986. Long-term variations of the external and internal components of the Earth's magnetic field, *J. geophys. Res.*, **91**, 4787–4796.
- Ghil, M., Allen, M. R., Dettinger, M. D., Ide, K., Kondrashov, D., Mann, M. E., Robertson, A. W., Saunders, A., Tian, Y., Varadi, F., & Yiou, P., 2002. Advanced spectral methods for climatic time series, *Rev. Geophys.*, **40**, 1–41.
- Gilbert, W., 1600. *De magnete, magneticisque corpori bus, et de magno magnete teilure*, Dover Publications, translated by P. F. Mottelay, 1958.
- Golub, G. H. & van Loan, C. F., 1989. *Matrix Computations*, John Hopkins University Press, Baltimore.
- Gonzalez, A. L. C. & Gonzalez, W. D., 1987. Periodicities in the interplanetary magnetic field polarity, *J. geophys. Res.*, **92**, 4357–4375.
- Gubbins, D., 1975. Can the Earth's magnetic field be sustained by core oscillations?, *Geophys. Res. Lett.*, **2**, 409–412.
- Gubbins, D., 1982. Finding core motions from magnetic observations, *Philos. Trans. R. Soc. Lond. A*, **306**, 247–254.
- Gubbins, D., 1983. Geomagnetic field analysis – I. Stochastic inversion, *Geophys. J. R. astr. Soc.*, **73**, 641–652.

- Gubbins, D., 1996. A formalism for the inversion of geomagnetic data for core motions with diffusion, *Phys. Earth Planet. Inter.*, **98**, 193–206.
- Gubbins, D. & Bloxham, J., 1987. Morphology of the geomagnetic field and implications for the geodynamo, *Nature*, **325**, 509–511.
- Gubbins, D. & Roberts, P. H., 1987. Magnetohydrodynamics of the Earth's core, in *Geomagnetism*, edited by J. A. Jacobs, vol. 2, chap. 1, Academic, San Diego, Calif.
- Halley, E., 1683. A theory of the variation of the magnetical compass, *Philos. Trans. R. Soc. London Series I*, **13**, 208–221.
- Halley, E., 1692. An account of the cause of the change of the magnetical needle, with an hypothesis of the structure of the internal parts of the Earth, *Philos. Trans. R. Soc. London Series I*, **16**, 563–578.
- Hide, R., 1969. Interaction between the Earth's liquid core and solid mantle, *Nature*, **222**, 1055–1056.
- Hide, R. & Dickey, J. O., 1991. Earth's variable rotation, *Science*, **253**, 629–637.
- Hills, R. G., 1979. *Convection in the Earth's mantle due to viscous shear at the core-mantle interface and due to large-scale buoyancy*, Ph.D. thesis, New Mexico State University, Las Cruces.
- Holme, R., 1998. Electromagnetic core-mantle coupling I: Explaining decadal variations in the Earth's length of day, *Geophys. J. Int.*, **132**, 167–180.
- Holme, R., 1998. Electromagnetic core-mantle coupling II: probing deep mantle conductance, in *The Core-Mantle Boundary Region*, edited by M. Gurnis, M. E. Wysession, E. Knittle, & B. A. Buffett, pp. 139–151, AGU, Washington DC.
- Holme, R., 2000. Electromagnetic core-mantle coupling III: Laterally varying mantle conductance, *Phys. Earth Planet. Int.*, **117**, 329–344.
- Holme, R. & Bloxham, J., 1996. The magnetic fields of Uranus and Neptune: Methods and models, *J. geophys. Res.*, **101**, 2177–2200.
- Holme, R. & de Viron, O., 2005. Geomagnetic jerks and a high-resolution length-of-day profile for core studies, *Geophys. J. Int.*, **160**, 435–440.
- Holme, R. & Olsen, N., 2005. Core–surface flow modelling from high resolution secular variation, submitted to GJI.
- Holme, R. & Whaler, K. A., 2001. Steady core flow in an azimuthally drifting reference frame, *Geophys. J. Int.*, **145**, 560–569.

- Hough, S. S., 1897. On the application of harmonic analysis to the dynamical theory of tides, *Philos. Trans. R. Soc. London Ser. A*, **89**, 201.
- Jackson, A., Bloxham, J., & Gubbins, D., 1993. Time-dependent flow at the core surface and conservation of angular momentum in the coupled core-mantle system, in *Dynamics of the Earth's deep interior and Earth rotation*, edited by J.-L. Le Mouél, D. E. Smylie, & T. Herring, pp. 97–107, AGU/IUGG.
- Jackson, A., Jonkers, A. R. T., & Walker, M. R., 2000. Four centuries of geomagnetic secular variation from historical records, *Phil. Trans. R. Soc. Lond. A*, **358**, 957–990.
- Jackson, D. D., 1979. The use of a priori data to resolve nonuniqueness in linear inversion, *Geophys. J. R. astr. Soc.*, **57**, 137–157.
- Jault, D. & Le Mouél, J. L., 1989. The topographic torque associated with a tangentially geostrophic motion at the core surface and inferences on flow inside the core, *Geophys. Astrophys. Fluid Dyn.*, **48**, 273–296.
- Jault, D., Gire, C., & Le Mouél, J. L., 1988. Westward drift, core motions and exchanges of angular momentum between core and mantle, *Nature*, **333**, 353–356.
- Jault, D., Hulot, G., & Le Mouel, J. L., 1996. Mechanical core-mantle coupling and dynamo modelling, *Phys. Earth Planet. Inter.*, **98**, 187–191.
- Kahle, A. B., Ball, R. H., & Cain, J. C., 1969. Prediction of geomagnetic secular change confirmed, *Nature*, **223**.
- Korte, M., 1999. Kombination regionaler magnetischer Vermessungen Europas zwischen 1955 und 1995, Scientific Technical Report STR99/11, GeoforschungsZentrum Potsdam.
- Kotzé, P. B., 2003. The time-varying geomagnetic field of Southern Africa, *Earth Planets Space*, **55**, 111–116.
- Krivova, N. A. & Solanki, S. K., 2002. The 1.3-year and 156-day periodicities in sunspot data: Wavelet analysis suggests a common origin, *Astron. and Astrophys.*, pp. 701–706.
- Labrosse, S., 2002. Hotspots, mantle plumes and core heat loss, *Earth Planet. Sci. Lett.*, **199**, 147–156.
- Langel, R. A., 1987. The main field, in *Geomagnetism*, edited by J. A. Jacobs, vol. 1, chap. 4, Academic, San Diego, Calif.
- Larmor, J., 1919. Possible rotational origin of magnetic fields of sun and earth, *Elect. Rev.*, **85**, 512.
- Lawson, C. L. & Hanson, R. J., 1974. *Solving least squares problems*, Prentice-Hall.

- Le Mouél, J.-L., 1984. Outer core geostrophic flow and secular variation of Earth's magnetic field, *Nature*, **311**, 734–735.
- Macmillan, S., 1996. A geomagnetic jerk for the early 1990's, *Earth Planet. Sci. Lett.*, **137**, 189–192.
- Malin, S. R. C. & Hodder, B. M., 1982. Was the 1970 geomagnetic jerk of internal or external origin, *Nature*, **296**, 726–728.
- Mandea, M., Bellanger, E., & Le-Mouél, J.-L., 2000. A geomagnetic jerk for the end of the 20th century?, *Earth Planet. Sci. Lett.*, **183**, 369–373.
- Mann, M. E. & Lees, J. M., 1996. Robust estimation of background noise and signal detection in climatic time series, *Climate Change*, **33**, 409–445.
- Matuyama, M., 1929. On the direction of magnetisation of basalt in Japan, Tyosen and Manchuria, *Japan Academy Proceedings*, **5**, 203–205.
- McLeod, M. G., 1985. On the geomagnetic jerk of 1969, *J. geophys. Res.*, **90**, 4597–4610.
- Mursula, K. & Zieger, B., 1996. The 13.5-day periodicity in the Sun, solar wind, and geomagnetic activity: The last three solar cycles, *J. geophys. Res.*, **101**, 27077–27090.
- Newitt, L. R., Barton, C. E., & Bitterly, J., 1996. *Guide for Magnetic Repeat Station Surveys*, International Association of Geomagnetism and Aeronomy.
- Olsen, N., 2002. A model of the geomagnetic field and its secular variation for epoch 2000 estimated from Ørsted data, *Geophys. J. Int.*, **149**, 455–463.
- Park, J., Lindberg, C. R., & Vernon, F. L., 1987. Multitaper spectral analysis of high-frequency seismograms, *J. geophys. Res.*, **92**, 12675–12684.
- Park, J., Vernon, F. L., & Lindberg, C. R., 1987. Frequency dependent polarization analysis of high-frequency seismograms, *J. geophys. Res.*, **92**, 12664–12674.
- Parker, R. L., 1994. *Geophysical Inverse Theory*, Princeton University Press, Princeton, NJ.
- Paularena, K. I., Szabo, A., & Richardson, J. D., 1995. Coincident 1.3-year periodicities in the ap geomagnetic index and the solar wind, *Geophys. Res. Lett.*, **22**, 3001–3004.
- Percival, D. B. & Walden, A. T., 1993. *Spectral analysis for physical applications. Multitaper and conventional univariate techniques*, Cambridge University Press, Cambridge, UK.
- Press, W. H., Teukolsky, S. A., Vetterling, W. T., & Flannery, B. P., 1993. *Numerical Recipes in C*, Cambridge, 2nd edn.

- Priestley, M. B., 1981. *Spectral Analysis and Time Series*, Academic Press and Harcourt Brace Jovanovich, 1st edn.
- Proudman, J., 1916. On the motions of solids in a liquid possessing vorticity, *Philos. Trans. R. Soc. London Ser. A*, **92**, 408–424.
- Roberts, P. H. & Scott, S., 1965. On the analysis of secular variation, 1, A hydromagnetic constraint: Theory, *J. Geomag. Geoelectr.*, **17**, 137–151.
- Rochester, M. G., 1984. Causes of fluctuations in the rotation of the Earth, *Philos. Trans. R. Soc. London A*, **313**, 95–105.
- Silverman, S. M. & Shapiro, R., 1983. Power spectral analysis of auroral occurrence frequency, *J. geophys. Res.*, **88**, 6310–6316.
- Slaucitajis, L. & Winch, D. E., 1965. Some morphological aspects of geomagnetic secular variation, *Planetary and Space Science*, **13**, 1097–1110.
- Slepian, S., 1978. Prolate spheroidal wave functions, fourier analysis and uncertainty, V, the discrete case, *Bell. Syst. Tech. J.*, **57**, 1371–1430.
- Stewart, D. N. & Whaler, K. A., 1992. Geomagnetic disturbance fields: An analysis of observatory monthly means, *Geophys. J. Int.*, **108**, 215–223.
- Stix, M. & Roberts, P. H., 1984. Time-dependent electromagnetic core-mantle coupling, *Phys. Earth Plan. Int.*, **36**, 49–60.
- Sugiura, M., 1964. Hourly values of equatorial Dst for the International Geophysical Year, *Annals International Geophysical Year*, **35**, 9.
- Sugiura, M. & Poros, D. J., 1977. Solar-generated quasi-biennial geomagnetic variation, *J. geophys. Res.*, **82**, 5621–5628.
- Taylor, G. I., 1917. Motion of solids in fluids when the flow is not irrotational, *Philos. Trans. R. Soc. London Ser. A*, **93**, 99–113.
- Taylor, J. B., 1963. The magneto-hydrodynamics of a rotating fluid and the Earth's dynamo problem, *Philos. Trans. R. Soc. London Ser. A*, **274**, 274–283.
- Thomson, D. J., 1982. Spectrum estimation and harmonic analysis, *IEEE Proc.*, **70**, 1055–1096.
- Vestine, E. H., 1953. Variations of the geomagnetic field, fluid motions, and the rate of the Earth's rotation, *J. geophys. Res.*, **58**, 127–145.
- Vestine, E. H. & Kahle, A. B., 1968. The westward drift and geomagnetic secular change, *Geophys. J. R. astr. Soc.*, **15**, 29–37.

- Voorhies, C. V., 2000. The radius of Earth's core from Oersted, Magsat, or SV, *Eos Trans. AGU (Fall Meeting Suppl.)*, **81**(48), GP61A–08.
- Voorhies, C. V. & Backus, G. E., 1985. Steady flows at the top of the core from geomagnetic field models: The steady motion theorem, *Geophys. Astrophys. Fluid Dyn.*, **32**, 163–173.
- Wiener, N., 1949. *Extrapolation, interpolation and smoothing of statistical time series*, MIT Press, Boston, Mass.
- Yukutake, T., 1965. The solar cycle contribution to the secular change in the geomagnetic field, *J. Geomag. Geoelectr.*, **17**, 287–309.
- Zatman, S. & Bloxham, J., 1997. Torsional oscillations and the magnetic field within the Earth's core, *Nature*, **388**, 760–763.
- Zatman, S. & Bloxham, J., 1998. A one-dimensional map of B_S from torsional oscillations of the Earth's core, in *The Core-Mantle Boundary Region*, edited by M. Gurnis, M. E. Wysession, E. Knittle, & B. A. Buffett, pp. 183–196, AGU.
- Zieger, B. & Mursula, K., 1998. Annual variation in near-Earth solar wind speed: Evidence for persistent north-south asymmetry related to solar magnetic polarity, *Geophys. Res. Lett.*, **25**, 841–844.

Appendix A

List of the used observatories and repeat stations

Table A.1: Magnetic observatories and repeat stations

Code	latitude	longitude	elev.	N_x	σ_x [nT]	N_y	σ_y [nT]	N_z	σ_z [nT]
<i>Geomagnetic Observatories</i>									
ALE	82.497	297.647	60	149	17.0	150	17.0	150	33.0
HIS	80.617	58.050	20	15	10.0	15	13.0	15	18.0
NAL	78.917	11.933	11	21	12.0	21	17.0	21	11.0
CCS	77.717	104.283	10	75	11.0	75	4.0	75	27.0
THL	77.467	290.767	57	224	10.0	224	7.0	224	23.0
HRN	77.000	15.550	15	224	10.0	224	8.0	224	16.0
MBC	76.315	240.638	40	184	17.0	186	14.0	186	16.0
RES	74.690	265.105	30	232	15.0	234	8.0	234	20.0
BJN2	74.500	19.200	80	82	8.0	82	5.0	82	9.0
DIK	73.543	80.562	15	74	21.0	74	14.0	74	14.0
TIK	71.583	129.000	40	92	14.0	92	8.0	47	23.0
BRW	71.323	203.380	12	224	11.0	224	9.0	224	14.0
TRO	69.663	18.948	112	115	6.0	115	4.0	115	10.0
GDH2	69.252	306.467	24	228	10.0	228	4.0	228	13.0
CBB	69.123	254.969	20	234	15.0	233	12.0	234	14.0
ABK	68.358	18.823	380	220	6.0	218	3.0	224	9.0
MMK	68.250	33.083	200	9	14.0	9	29.0	9	11.0
KIR	67.833	20.417	390	20	5.0	20	4.0	20	10.0
SOD3	67.368	26.630	178	224	5.0	224	3.0	224	8.0
CWE	66.163	190.165	10	93	8.0	93	10.0	93	11.0
CMO2	64.867	212.167	90	217	8.0	217	5.0	217	9.0
ARK	64.583	40.500	0	35	13.0	35	5.0	41	9.0
<i>continued on next page</i>									

<i>continued from previous page</i>										
Code	latitude	longitude	elev.	N_x	σ_x [nT]	N_y	σ_y [nT]	N_z	σ_z [nT]	
OUL	64.520	27.230	130	7	5.0	7	2.0	7	4.0	
BLC	64.333	263.967	30	224	12.0	224	9.0	224	14.0	
LRV	64.183	338.300	5	224	6.0	224	4.0	224	8.0	
IQA	63.753	291.482	67	54	6.0	54	14.0	54	13.0	
YKC2	62.482	245.518	198	212	13.0	212	10.0	212	12.0	
DOB2	62.073	9.117	660	26	5.0	26	3.0	26	5.0	
YAK	62.017	129.717	100	171	8.0	171	13.0	171	9.0	
POD	61.600	90.000	0	128	10.0	128	12.0	127	7.0	
NAQ	61.100	314.800	4	227	7.0	227	4.0	228	9.0	
NUR	60.508	24.655	110	224	5.0	224	3.0	224	8.0	
LER	60.133	358.817	85	233	5.0	233	3.0	233	8.0	
MGD	60.117	151.017	0	128	13.0	128	23.0	128	39.0	
LNN	59.950	30.705	70	104	6.0	104	3.0	106	7.0	
LOV	59.345	17.827	25	213	6.0	213	3.0	224	8.0	
FCC	58.759	265.912	15	234	10.0	234	6.0	234	11.0	
BOX	58.030	38.970	0	223	8.0	223	5.0	223	8.0	
SIT2	57.067	224.683	24	232	10.0	232	5.0	232	7.0	
ARS	56.433	58.568	290	126	8.0	126	3.0	125	6.0	
KZN	55.833	48.850	80	100	7.0	100	3.0	100	7.0	
BFE	55.625	11.672	80	212	6.0	212	3.0	212	7.0	
MOS	55.467	37.312	200	119	18.0	119	7.0	119	11.0	
ESK	55.317	356.800	242	233	6.0	233	5.0	233	7.0	
PBQ	55.277	282.255	40	156	11.0	156	5.0	156	10.0	
GWC	55.267	282.217	23	43	38.0	43	24.0	43	22.0	
NVS	55.033	82.900	120	218	9.0	218	5.0	218	7.0	
KLD	54.700	20.617	0	0	1.0	0	1.0	3	9.0	
MEA	54.616	246.653	700	234	10.0	234	5.0	234	9.0	
HLP	54.608	18.815	3	139	7.0	139	5.0	139	7.0	
MNK	54.500	27.883	200	174	8.0	174	7.0	174	10.0	
WNG	53.743	9.073	50	224	6.0	224	3.0	224	7.0	
PET2	53.100	158.633	110	152	9.0	152	4.0	152	6.0	
WIT	52.813	6.668	20	51	7.0	51	3.0	51	6.0	
IRK	52.167	104.450	540	169	11.0	169	5.0	169	8.0	
NGK	52.072	12.675	78	234	7.0	234	3.0	234	7.0	
VAL	51.933	349.750	8	198	7.0	198	3.0	188	7.0	
BEL	51.837	20.792	180	224	7.0	224	3.0	224	7.0	
HAD	50.995	355.517	91	234	7.0	234	3.0	234	6.0	
KIV2	50.717	30.300	100	126	8.0	126	4.0	126	8.0	
MAB	50.298	5.682	440	56	6.0	56	2.0	56	5.0	

continued on next page

<i>continued from previous page</i>									
Code	latitude	longitude	elev.	N_x	σ_x [nT]	N_y	σ_y [nT]	N_z	σ_z [nT]
DOU	50.097	4.595	208	137	6.0	137	7.0	137	5.0
LVV	49.900	23.750	400	21	8.0	21	6.0	21	8.0
KGD	49.817	73.083	0	42	23.0	42	35.0	46	35.0
GLN	49.645	262.880	229	65	10.0	65	8.0	64	8.0
MZL	49.600	117.400	682	55	8.0	55	5.0	55	5.0
BDV	49.080	14.015	496	79	6.0	79	3.0	79	6.0
VIC	48.517	236.583	197	212	7.0	212	4.0	212	6.0
WIK	48.265	16.318	400	70	6.0	70	3.0	70	5.0
NEW	48.263	242.880	780	234	7.0	234	4.0	236	7.0
FUR	48.165	11.277	570	224	8.0	224	3.0	224	6.0
CLF	48.023	2.260	145	224	7.0	224	3.0	224	6.0
HRB	47.873	18.190	120	147	25.0	147	4.0	135	9.0
NCK	47.633	16.717	160	71	7.0	71	5.0	71	6.0
STJ	47.595	307.323	100	202	11.0	202	6.0	202	7.0
YSS	46.950	142.717	70	11	6.0	11	8.0	11	7.0
THY	46.900	17.893	190	114	9.0	114	12.0	114	10.0
ODE	46.783	30.883	140	141	10.0	141	52.0	141	6.0
CTS	46.047	11.650	1200	16	6.0	16	6.0	16	4.0
NKK	45.800	62.100	0	14	10.0	14	9.0	14	6.0
OTT	45.400	284.450	75	212	8.0	212	4.0	212	7.0
SUA	44.680	26.253	84	70	8.0	70	5.0	70	5.0
GCK	44.633	20.767	231	21	7.0	21	2.0	21	5.0
MMB	43.907	144.193	39	224	10.0	224	5.0	224	7.0
CNH2	43.827	125.299	234	20	10.0	20	8.0	20	6.0
WMQ	43.817	87.697	970	21	10.0	21	3.0	19	5.0
VLA	43.683	132.167	300	105	73.0	105	337.0	108	6.0
AAA	43.250	76.917	1300	96	11.0	96	27.0	98	8.0
PAG	42.515	24.177	556	162	9.0	162	3.0	162	5.0
AQU	42.383	13.317	630	219	9.0	219	4.0	219	6.0
TFS	42.092	44.705	980	228	12.0	228	5.0	228	11.0
TKT	41.333	69.617	810	75	13.0	75	7.0	81	19.0
ISK	41.063	29.062	130	150	121.0	150	9.0	150	8.0
EBR	40.820	0.493	50	4	6.0	4	3.0	4	3.0
BMT	40.300	116.200	183	33	15.0	33	5.0	33	28.0
COI	40.222	351.578	100	27	11.0	27	54.0	27	12.0
BOU	40.138	254.762	1650	224	8.0	224	5.0	224	7.0
BJI	40.040	116.175	69	20	11.0	20	4.0	20	9.0
ANK	39.891	32.764	905	7	22.0	7	83.0	7	16.0
TOL	39.883	355.953	501	2	9.0	2	4.0	2	4.0

continued on next page

<i>continued from previous page</i>										
Code	latitude	longitude	elev.	N_x	σ_x [nT]	N_y	σ_y [nT]	N_z	σ_z [nT]	
SPT	39.547	355.650	922	46	7.0	46	3.0	46	5.0	
KSH	39.500	76.000	1320	40	9.0	40	3.0	40	6.0	
ESA	39.234	141.358	396	7	7.0	7	3.0	7	2.0	
DLN	39.100	121.500	131	2	14.0	2	1.0	2	8.0	
MIZ	39.010	141.080	120	42	10.0	42	4.0	42	5.0	
FRD	38.205	282.627	69	191	8.0	191	5.0	191	6.0	
PEG2	38.080	23.933	495	4	8.0	4	8.0	4	7.0	
PEG1	38.047	23.866	495	7	8.0	7	6.0	7	17.0	
ASH	37.950	58.108	570	74	13.0	74	13.0	75	12.0	
FRN	37.090	240.280	331	186	9.0	186	4.0	192	6.0	
ALM	36.850	357.533	65	12	12.0	12	5.0	12	18.0	
SFS2	36.500	353.883	65	9	9.0	9	15.0	9	3.0	
GLM	36.400	94.900	2802	6	9.0	6	2.0	6	5.0	
KAK	36.230	140.190	26	224	11.0	224	6.0	224	5.0	
LZH	36.087	103.845	1560	54	12.0	54	5.0	54	8.0	
TUL	35.912	264.212	328	5	75.0	5	156.0	5	163.0	
KNZ	35.253	139.960	342	21	8.0	21	6.0	21	4.0	
QIX	34.600	108.200	893	16	9.0	16	4.0	16	6.0	
AVE	33.300	352.583	230	6	8.0	6	9.0	6	9.0	
HTY	33.122	139.802	220	157	11.0	157	7.0	157	5.0	
TUC1	32.247	249.167	770	177	10.0	177	6.0	177	6.0	
TUC2	32.180	249.270	924	42	7.0	42	6.0	42	5.0	
BGY	31.730	35.210	750	73	14.0	73	7.0	73	14.0	
AMT1	31.550	34.917	350	55	10.0	55	5.0	55	9.0	
KNY	31.420	130.882	106	224	11.0	224	7.0	224	4.0	
SSH	31.097	121.187	100	97	20.0	97	183.0	97	6.0	
CHD	31.000	103.700	653	57	9.0	57	8.0	57	4.0	
WHN	30.528	114.559	42	60	10.0	60	3.0	60	24.0	
SAB	30.363	77.798	498	21	10.0	21	9.0	21	38.0	
BSL	30.350	270.360	8	148	11.0	148	22.0	149	38.0	
QUE	30.187	66.950	1750	20	20.0	20	24.0	20	35.0	
LSA	29.700	91.150	3658	15	12.0	15	10.0	15	10.0	
ELT	29.670	34.950	250	17	12.0	17	6.0	17	6.0	
MLT	29.515	30.892	120	14	126.0	14	377.0	14	184.0	
DLR	29.487	259.085	355	192	12.0	192	5.0	189	6.0	
TEN	28.483	343.733	310	13	9.0	13	5.0	13	3.0	
GUI	28.320	343.570	848	30	9.0	30	3.0	30	5.0	
CBI	27.083	142.167	154	84	11.0	84	10.0	87	5.0	
JAI	26.917	75.800	438	84	18.0	84	7.0	85	7.0	

continued on next page

<i>continued from previous page</i>									
Code	latitude	longitude	elev.	N_x	σ_x [nT]	N_y	σ_y [nT]	N_z	σ_z [nT]
SHL	25.567	91.883	130	68	16.0	68	12.0	92	10.0
LNP	25.000	121.167	100	174	13.0	170	9.0	166	8.0
KRC	24.950	67.140	0	41	37.0	41	36.0	41	32.0
QZH	24.900	118.600	10	16	7.0	16	5.0	16	3.0
THJ	24.000	102.700	1820	128	8.0	128	3.0	128	4.0
UJJ	23.183	75.783	499	122	19.0	122	16.0	128	13.0
GZH	23.093	113.343	11	18	9.0	18	7.0	18	8.0
HVN3	22.983	277.683	0	10	61.0	10	17.0	11	61.0
TAM	22.792	5.527	1373	88	13.0	88	25.0	88	8.0
CPA	22.350	103.833	0	4	61.0	4	40.0	2	185.0
HON3	21.320	201.998	3	189	10.0	189	6.0	189	5.0
NGR	21.150	79.083	312	12	8.0	12	13.0	12	11.0
PHU	21.033	105.967	5	22	7.0	22	3.0	27	25.0
TEO	19.747	260.818	2280	20	18.0	20	35.0	20	16.0
QGZ	19.000	109.800	227	28	10.0	28	5.0	28	5.0
ABG	18.638	72.872	7	212	13.0	212	7.0	212	10.0
SJG2	18.117	293.850	400	226	40.0	226	97.0	225	217.0
VSK	17.670	83.320	3	12	4.0	12	27.0	12	27.0
HYB	17.413	78.555	500	25	8.0	25	13.0	25	6.0
MBO	14.392	343.042	5	235	12.0	235	5.0	235	5.0
MUT	14.375	121.015	62	9	24.0	9	13.0	9	28.0
GUA	13.583	144.870	150	201	12.0	201	4.0	197	6.0
PND	11.920	79.920	6	17	9.0	17	17.0	17	16.0
DLT	11.917	108.417	0	8	9.0	8	44.0	12	112.0
ANN	11.367	79.683	0	119	13.0	119	17.0	123	18.0
CRP	10.440	275.089	1030	8	15.0	8	16.0	8	17.0
KOD	10.230	77.463	2323	17	17.0	17	15.0	17	143.0
BCL	9.283	105.733	0	1	2.0	1	39.0	2	88.0
AAE1	9.030	38.767	2441	149	19.0	149	16.0	149	23.0
ETT	9.000	78.000	47	32	8.0	32	9.0	32	9.0
TRD2	8.483	76.950	300	84	38.0	84	23.0	84	14.0
FUQ	5.470	286.263	2543	21	15.0	21	11.0	21	16.0
BNG	4.437	18.565	390	224	15.0	224	6.0	224	17.0
TUN	3.510	98.560	0	6	78.0	6	16.0	6	201.0
KOU	2.210	307.269	10	36	10.0	36	5.0	36	8.0
TTB2	-1.205	311.483	10	51	14.0	51	14.0	52	23.0
TNG	-6.167	106.633	14	20	29.0	20	29.0	20	43.0
ASC	-7.949	345.617	177	56	10.0	56	4.0	56	3.0
LUA3	-8.917	13.167	53	13	23.0	13	26.0	13	15.0

continued on next page

<i>continued from previous page</i>									
Code	latitude	longitude	elev.	N_x	σ_x [nT]	N_y	σ_y [nT]	N_z	σ_z [nT]
PMG	-9.408	147.152	80	134	12.0	134	3.0	134	4.0
ANC	-11.690	282.852	49	4	55.0	4	11.0	4	13.0
HUA	-12.045	284.660	3313	85	15.0	85	8.0	86	7.0
THJ	24.000	102.700	1820	35	12.0	35	2.0	35	5.0
API	-13.807	188.225	2	165	12.0	165	6.0	169	11.0
NMP	-15.087	39.253	376	17	22.0	17	7.0	18	8.0
PTY	-17.250	292.050	3789	3	377.0	3	156.0	3	56.0
PPT	-17.568	210.425	90	227	12.0	227	5.0	227	4.0
TAN	-18.917	47.550	1375	134	10.0	134	7.0	107	6.0
TSU	-19.217	17.700	83	195	14.0	195	10.0	193	7.0
CTA	-20.100	146.300	370	109	12.0	109	3.0	109	4.0
LQA	-22.103	294.395	3450	21	10.0	21	5.0	3	70.0
LRM	-22.220	114.100	4	106	12.0	106	7.0	105	8.0
VSS	-22.400	316.350	457	43	18.0	43	41.0	43	32.0
ASP	-23.762	133.883	557	64	11.0	64	2.0	64	4.0
HBK	-25.882	27.707	1522	225	13.0	225	5.0	215	8.0
LMM	-25.917	32.583	50	53	15.0	53	4.0	53	7.0
PIL	-31.667	296.117	336	68	11.0	68	4.0	68	7.0
GNA	-31.783	115.950	60	202	9.0	202	4.0	202	6.0
HER	-34.425	19.225	26	235	10.0	235	4.0	235	7.0
LAS	-35.007	302.310	20	17	17.0	17	14.0	17	9.0
CNB	-35.315	149.363	850	214	9.0	214	3.0	214	5.0
AMS	-37.833	77.567	50	209	8.0	209	2.0	209	8.0
TRW	-43.268	294.618	30	51	9.0	51	7.0	51	4.0
EYR	-43.417	172.350	390	224	8.0	224	3.0	224	6.0
CZT	-46.433	51.867	160	234	7.0	234	3.0	234	7.0
PAF	-49.350	70.200	50	233	9.0	233	5.0	233	8.0
PST	-51.703	302.110	135	55	11.0	55	25.0	55	6.0
GTV	-54.283	323.516	580	15	9.0	15	5.0	15	5.0
MCQ	-54.500	158.950	4	72	6.0	72	4.0	72	8.0
ARC	-62.160	301.522	6	180	10.0	180	13.0	176	10.0
LIV	-62.662	299.605	19	31	6.0	31	2.0	31	5.0
AIA	-65.245	295.742	10	129	8.0	129	4.0	129	15.0
CSY	-66.283	110.533	40	125	53.0	125	21.0	123	57.0
MIR	-66.550	93.017	20	81	23.0	81	27.0	81	39.0
DRV	-66.665	140.007	40	233	22.0	233	9.0	233	14.0
MAW	-67.605	62.882	12	125	9.0	125	9.0	125	16.0
MOL	-67.667	45.850	0	17	28.0	17	13.0	17	32.0
DVS	-68.583	77.967	29	131	44.0	131	22.0	132	27.0

continued on next page

<i>continued from previous page</i>									
Code	latitude	longitude	elev.	N_x	σ_x [nT]	N_y	σ_y [nT]	N_z	σ_z [nT]
SYO	-69.007	39.590	0	10	11.0	10	17.0	10	5.0
SNA3	-70.316	354.416	50	96	26.0	96	82.0	96	12.0
GVN2	-70.650	351.250	42	6	11.0	6	46.0	6	5.0
NVL	-70.760	11.816	460	8	14.0	8	15.0	8	41.0
TNB	-74.683	164.117	28	9	11.0	9	18.0	9	15.0
SBA	-77.850	166.783	15	223	13.0	223	20.0	223	18.0
VOS	-78.450	106.867	3500	78	17.0	78	18.0	78	29.0
<i>Repeat Station (multiple visits)</i>									
Huse	65.643	345.723	0	2	1.0	2	1.0	2	4.0
Patr	65.557	336.018	68	3	5.0	3	6.0	3	6.0
Gudn	63.578	339.840	6	7	2.0	7	2.0	7	6.0
1001	46.150	19.567	0	4	1.0	4	1.0	4	3.0
Yagi	44.440	141.427	0	3	4.0	3	5.0	3	2.0
1160	44.400	22.583	4	4	2.0	4	2.0	4	2.0
1126	43.300	21.833	7	4	2.0	4	2.0	4	2.0
3001	42.600	19.933	10	4	3.0	4	2.0	4	2.0
1143	42.500	22.417	2	4	3.0	4	4.0	4	3.0
Hiro	42.267	143.300	2	3	3.0	3	5.0	3	3.0
MELG	42.120	351.772	6	2	2.0	2	18.0	2	10.0
BRAG	41.857	353.293	0	2	6.0	2	4.0	2	2.0
CHAV	41.727	352.535	34	4	10.0	4	7.0	4	21.0
VIAN	41.723	351.173	0	4	7.0	4	5.0	4	3.0
BRAG	41.590	351.562	0	2	2.0	2	2.0	2	6.0
MIRA	41.515	353.728	74	3	4.0	3	12.0	3	1.0
MIRA	41.472	352.772	37	2	6.0	2	8.0	2	6.0
ALIJ	41.328	352.542	0	2	7.0	2	5.0	2	3.0
VILA	41.277	352.280	0	2	2.0	2	3.0	2	2.0
PORT	41.235	351.327	0	5	9.0	5	9.0	5	8.0
LAME	41.083	352.197	143	2	14.0	2	5.0	2	5.0
ESPI	40.973	351.355	0	2	2.0	2	7.0	2	2.0
FIGU	40.943	353.072	0	3	6.0	3	6.0	3	10.0
AVEI	40.653	351.262	0	2	2.0	2	8.0	2	1.0
COVI	40.280	352.522	0	4	3.0	4	9.0	4	6.0
LOUS	40.143	351.762	0	2	9.0	2	4.0	2	7.0
MONF	39.973	353.097	0	2	3.0	2	1.0	2	4.0
LEIR	39.782	351.182	0	2	2.0	2	3.0	2	8.0
CAST	39.467	352.548	0	6	9.0	6	15.0	6	13.0
CALD	39.413	350.803	16	6	22.0	6	12.0	6	27.0
CHAM	39.343	351.540	0	4	11.0	4	16.0	4	12.0
<i>continued on next page</i>									

<i>continued from previous page</i>									
Code	latitude	longitude	elev.	N_x	σ_x [nT]	N_y	σ_y [nT]	N_z	σ_z [nT]
Sizu	38.630	141.530	26	2	5.0	2	7.0	2	3.0
PALM	38.547	351.032	25	4	12.0	4	17.0	4	12.0
EVOR	38.528	352.110	0	3	10.0	3	25.0	3	15.0
HORT	38.518	331.292	17	2	27.0	2	5.0	2	10.0
BEJA	38.135	352.077	30	3	3.0	3	10.0	3	10.0
BEJA	38.060	352.127	0	2	5.0	2	14.0	2	4.0
Aika	38.019	138.227	10	2	7.0	2	8.0	2	1.0
BEJA	37.882	352.137	0	6	3.0	6	5.0	6	22.0
PONT	37.743	334.297	0	2	20.0	2	4.0	2	18.0
PRAI	37.193	352.533	0	2	27.0	2	2.0	2	20.0
PORT	37.150	351.420	5	2	10.0	2	11.0	2	12.0
PORT	37.127	351.433	35	3	7.0	3	14.0	3	18.0
FARO	37.015	352.040	0	3	29.0	3	10.0	3	20.0
SANT	36.972	334.825	0	2	16.0	2	1.0	2	22.0
Taiz	33.579	135.877	32	2	3.0	2	5.0	2	2.0
Bare	32.033	34.950	0	3	4.0	3	6.0	3	8.0
Shde	30.417	34.950	0	3	6.0	3	6.0	3	8.0
534V	10.433	286.757	0	2	8.0	2	9.0	2	12.0
161A	10.061	286.755	0	2	5.0	2	3.0	2	22.0
96A_	6.397	286.722	0	2	13.0	2	3.0	2	497.0
102A	5.532	286.664	0	2	25.0	2	5.0	2	11.0
105A	5.260	287.549	0	2	13.0	2	11.0	2	115.0
34AB	3.824	282.998	0	2	5.0	2	4.0	2	57.0
31A_	2.450	283.384	0	2	13.0	2	1.0	2	29.0
27A_	1.813	281.241	0	2	6.0	2	76.0	2	23.0
121A	0.511	283.491	0	2	1.0	2	1.0	2	1.0
FORT	-3.870	321.590	0	2	7.0	2	3.0	2	2.0
_MPA	-17.633	24.183	0	1	1.0	1	2.0	2	5.0
_Ora	-21.267	25.317	100	2	2.0	2	3.0	2	1.0
ITAP	-23.967	311.137	0	2	2.0	2	35.0	2	92.0
Bird	-25.901	139.349	0	2	1.0	2	1.0	2	1.0
RIO_	-32.090	307.838	2	3	29.0	3	11.0	3	29.0
Hami	-37.861	175.327	1	2	2.0	2	2.0	2	1.0
New_	-39.006	174.179	20	2	2.0	2	1.0	2	1.0
Ohak	-40.211	175.387	0	2	1.0	2	1.0	2	2.0
Wood	-41.522	173.874	1	2	1.0	2	1.0	2	5.0
Moun	-43.773	170.123	4	2	1.0	2	1.0	2	1.0
Oama	-44.974	171.093	37	2	1.0	2	1.0	2	1.0
Laud	-45.037	169.682	21	2	1.0	2	6.0	2	4.0

continued on next page

<i>continued from previous page</i>										
Code	latitude	longitude	elev.	N_x	σ_x [nT]	N_y	σ_y [nT]	N_z	σ_z [nT]	
Mana	-45.533	167.646	17	2	3.0	2	6.0	2	1.0	
AMER	-46.387	51.809	4	4	4.0	4	5.0	4	4.0	
Inve	-46.413	168.323	0	2	1.0	2	3.0	2	1.0	
Port	-48.678	69.025	0	2	2.0	2	11.0	2	2.0	
KGL_	-49.352	70.215	2	2	1.0	2	3.0	2	2.0	
Obse	-49.420	69.889	2	3	6.0	3	6.0	3	4.0	
PORT	-49.552	69.818	0	4	55.0	4	38.0	4	7.0	
_VAN	-52.547	169.148	1	2	27.0	2	1.0	2	21.0	
_GAR	-52.558	169.145	1	2	4.0	2	10.0	2	9.0	
_VEN	-52.564	169.148	0	3	34.0	3	17.0	3	12.0	
<i>Repeat Station (two visits)</i>										
Fort	47.223	291.346	0	1	3.0	1	1.0	1	2.0	
Marq	46.538	272.577	0	1	3.0	1	1.0	1	7.0	
Huro	44.398	261.782	39	1	1.0	1	1.0	1	1.0	
Huro	44.378	261.772	0	1	1.0	1	1.0	1	1.0	
_RUM	43.840	141.592	16	1	6.0	1	1.0	1	3.0	
_NEM	43.203	145.075	44	1	5.0	1	4.0	1	2.0	
_IWA	43.077	141.850	10	1	5.0	1	50.0	1	6.0	
_2	28.503	47.867	0	1	12.0	1	8.0	1	12.0	
Loga	41.763	248.343	36	1	4.0	1	3.0	1	3.0	
King	41.488	288.455	1	1	6.0	1	14.0	1	1.0	
_SHI	41.332	141.372	78	1	5.0	1	5.0	1	3.0	
Duns	41.227	237.687	0	1	2.0	1	2.0	1	1.0	
WISE	40.725	352.107	0	1	2.0	1	6.0	1	2.0	
CERN	40.162	351.527	0	1	1.0	1	9.0	1	10.0	
LAGE	38.780	332.905	0	1	4.0	1	3.0	1	10.0	
_ISH	38.462	141.248	44	1	1.0	1	3.0	1	6.0	
AMAR	38.180	352.797	0	1	13.0	1	20.0	1	23.0	
SINE	37.938	351.187	0	1	11.0	1	1.0	1	5.0	
SAO_	37.547	351.272	2	1	7.0	1	3.0	1	3.0	
LAGO	37.123	351.325	0	1	7.0	1	11.0	1	20.0	
_ASA	36.432	138.602	0	1	1.0	1	4.0	1	2.0	
Ama_	36.093	133.104	20	1	1.0	1	10.0	1	3.0	
_TOT	35.413	134.312	16	1	2.0	1	2.0	1	5.0	
_KUR	35.410	133.997	0	1	4.0	1	1.0	1	6.0	
_OKA	34.778	133.790	0	1	1.0	1	1.0	1	8.0	
_MIK	34.665	137.223	4	1	27.0	1	281.0	1	6.0	
Toyo	34.376	129.314	0	1	3.0	1	7.0	1	1.0	
Fort	34.018	279.090	15	1	9.0	1	1.0	1	2.0	
<i>continued on next page</i>										

<i>continued from previous page</i>									
Code	latitude	longitude	elev.	N_x	σ_x [nT]	N_y	σ_y [nT]	N_z	σ_z [nT]
Fort	34.017	279.085	16	1	7.0	1	1.0	1	4.0
_KOU	33.642	133.813	0	1	6.0	1	11.0	1	6.0
_NAK	33.525	131.062	38	1	1.0	1	1.0	1	2.0
_Isr	33.050	35.450	49	1	7.0	1	1.0	1	1.0
SanD	32.887	242.928	0	1	1.0	1	4.0	1	2.0
_Isr	32.883	35.367	25	1	27.0	1	8.0	1	81.0
_Isr	32.733	35.033	0	1	4.0	1	13.0	1	9.0
_Isr	32.500	35.433	0	1	10.0	1	9.0	1	13.0
_Isr	32.250	35.017	0	1	44.0	1	13.0	1	1.0
_Isr	32.167	35.533	0	1	2.0	1	13.0	1	1.0
_Isr	31.683	35.450	0	1	10.0	1	8.0	1	1.0
_Isr	31.433	34.767	0	1	21.0	1	1.0	1	7.0
Wayc	31.255	277.600	0	1	1.0	1	4.0	1	11.0
_Isr	31.217	34.317	0	1	3.0	1	8.0	1	1.0
_Isr	31.183	35.317	0	1	5.0	1	8.0	1	3.0
Broo	31.030	270.830	11	1	8.0	1	1.0	1	1.0
Lama	30.925	270.613	11	1	4.0	1	1.0	1	1.0
_Isr	30.867	34.433	0	1	8.0	1	9.0	1	4.0
_Isr	30.850	34.783	0	1	10.0	1	5.0	1	2.0
_Isr	30.817	35.283	0	1	4.0	1	16.0	1	6.0
_TAN	30.733	131.067	0	1	5.0	1	5.0	1	2.0
_Isr	30.500	34.617	0	1	7.0	1	5.0	1	9.0
_Isr	30.117	34.717	0	1	4.0	1	2.0	1	17.0
_Isr	30.083	35.133	0	1	3.0	1	2.0	1	9.0
_Isr	29.533	34.917	0	1	1.0	1	15.0	1	8.0
_29	28.932	47.402	0	1	18.0	1	2.0	1	3.0
_4	28.686	45.208	0	1	19.0	1	3.0	1	5.0
_2	28.503	47.867	0	0	1.0	0	1.0	2	1.0
_B	28.475	45.693	0	1	20.0	1	1.0	1	4.0
_4	28.467	47.017	0	1	19.0	1	3.0	1	4.0
_B	28.247	46.341	0	1	19.0	1	2.0	1	4.0
_	27.548	46.379	0	0	1.0	0	1.0	1	6.0
_43	27.475	43.332	0	0	1.0	0	1.0	1	6.0
_4	27.268	44.510	0	1	15.0	1	22.0	1	2.0
_	27.190	47.360	0	0	1.0	0	1.0	1	6.0
_3	27.163	45.705	0	1	20.0	1	2.0	1	7.0
_43	27.015	43.713	0	0	1.0	0	1.0	1	8.0
_4	26.883	45.282	0	1	27.0	1	15.0	1	8.0
_3	26.862	46.495	0	0	1.0	0	1.0	1	7.0

continued on next page

<i>continued from previous page</i>									
Code	latitude	longitude	elev.	N_x	σ_x [nT]	N_y	σ_y [nT]	N_z	σ_z [nT]
---	26.720	45.337	0	1	20.0	1	1.0	1	8.0
Isig	24.351	124.224	0	1	3.0	1	3.0	1	6.0
Mina	24.295	153.983	0	1	9.0	1	6.0	1	2.0
_1Ca	22.677	106.231	0	1	1.0	1	4.0	1	3.0
_2Ph	22.397	103.530	157	0	1.0	0	1.0	1	2.0
_3Sa	22.333	103.833	0	1	1.0	1	1.0	1	1.0
_4Th	22.297	106.455	0	0	1.0	0	1.0	1	3.0
_5Ph	22.197	104.560	0	0	1.0	0	1.0	1	1.0
_6Ba	22.114	105.854	0	0	1.0	0	1.0	1	1.0
_7Mu	21.948	103.142	0	1	3.0	1	1.0	1	4.0
_8La	21.813	106.713	0	1	1.0	1	1.0	1	2.0
_9Ye	21.713	104.921	1	1	1.0	1	1.0	1	2.0
12Mo	21.609	107.944	65	1	2.0	1	1.0	1	5.0
10Tu	21.581	103.424	3	0	1.0	0	1.0	1	2.0
11Th	21.546	105.864	0	0	1.0	0	1.0	1	1.0
13Di	21.390	103.017	2	1	1.0	1	40.0	1	15.0
14Ph	21.383	105.356	1	0	1.0	0	1.0	1	2.0
15Ti	21.338	107.375	65	1	1.0	1	5.0	1	2.0
16So	21.330	103.942	1	1	4.0	1	5.0	1	1.0
17Ba	21.271	106.128	1	0	1.0	0	1.0	1	3.0
18No	21.222	105.804	0	1	1.0	1	1.0	1	4.0
19Ba	21.125	104.210	0	0	1.0	0	1.0	1	1.0
20Ph	21.030	105.950	2	1	1.0	1	3.0	1	3.0
21Ca	20.962	107.148	0	1	5.0	1	24.0	1	9.0
22Ha	20.919	106.674	76	1	1.0	1	1.0	1	3.0
23Mo	20.844	104.670	0	0	1.0	0	1.0	1	7.0
24Ho	20.732	105.326	0	1	19.0	1	16.0	1	11.0
25Na	20.450	106.083	0	0	1.0	0	1.0	1	1.0
26Gi	20.345	105.928	0	1	1.0	1	11.0	1	2.0
27Sa	19.725	105.889	0	0	1.0	0	1.0	1	8.0
28Ho	19.268	105.725	0	0	1.0	0	1.0	1	2.0
29Vi	18.676	105.691	0	1	9.0	1	7.0	1	2.0
30Ky	18.051	106.324	0	0	1.0	0	1.0	1	1.0
31Do	17.495	106.625	0	1	3.0	1	6.0	1	2.0
32Gi	16.937	107.072	0	1	30.0	1	33.0	1	6.0
Podo	16.680	345.037	0	1	3.0	1	3.0	1	1.0
Rich	16.437	344.343	0	1	1.0	1	24.0	1	1.0
33Hu	16.422	107.578	0	1	1.0	1	19.0	1	2.0
34Da	16.060	108.197	0	1	9.0	1	1.0	1	3.0

continued on next page

<i>continued from previous page</i>									
Code	latitude	longitude	elev.	N_x	σ_x [nT]	N_y	σ_y [nT]	N_z	σ_z [nT]
Mata	15.600	346.672	0	0	1.0	0	1.0	1	2.0
Ling	15.398	344.898	0	1	4.0	1	2.0	1	2.0
35Bi	15.276	108.771	0	1	1.0	1	21.0	1	3.0
36Sa	14.656	109.065	0	1	1.0	1	5.0	1	1.0
Mopt	14.512	355.910	0	1	1.0	1	11.0	1	3.0
37Pl	13.977	108.028	19	1	5.0	1	2.0	1	5.0
38An	13.974	108.732	0	1	2.0	1	5.0	1	1.0
39Qu	13.734	109.209	0	1	3.0	1	4.0	1	2.0
Kita	13.070	350.507	14	1	11.0	1	3.0	1	2.0
40De	12.943	109.505	0	1	2.0	1	23.0	1	6.0
42M'	12.752	108.748	53	1	9.0	1	9.0	1	9.0
41Bu	12.699	108.148	0	1	2.0	1	14.0	1	9.0
Bama	12.657	352.068	0	1	1.0	1	8.0	1	3.0
Kedo	12.565	347.783	0	1	9.0	1	1.0	1	6.0
43Nh	12.232	109.183	0	1	14.0	1	15.0	1	1.0
487A	12.184	287.859	0	1	2.0	1	1.0	1	42.0
44Da	11.945	108.483	0	1	5.0	1	13.0	1	2.0
61PU	11.923	288.726	30	1	5.0	1	5.0	1	37.0
45Ph	11.532	108.934	0	1	6.0	1	7.0	1	10.0
184A	11.469	287.406	30	1	8.0	1	1.0	1	4.0
46Ba	11.411	107.616	40	1	18.0	1	5.0	1	49.0
47Ta	11.291	106.099	0	1	24.0	1	4.0	1	3.0
48Ba	11.200	108.334	0	1	9.0	1	7.0	1	5.0
49Xu	10.912	107.428	70	1	2.0	1	10.0	1	3.0
50Sa	10.813	106.641	20	1	11.0	1	7.0	1	8.0
51Ta	10.546	106.399	0	1	4.0	1	1.0	1	11.0
6A_C	10.453	284.486	0	1	40.0	1	5.0	1	42.0
52Vu	10.390	107.119	0	1	31.0	1	6.0	1	4.0
53Ca	9.971	105.740	0	1	12.0	1	9.0	1	1.0
20A_	9.317	284.586	0	1	3.0	1	32.0	1	11.0
54Ba	9.300	105.711	0	1	1.0	1	7.0	1	1.0
55Ca	9.177	105.176	0	0	1.0	0	1.0	1	3.0
43AE	9.054	286.012	0	1	3.0	1	5.0	1	15.0
56Ra	8.605	105.007	0	1	170.0	1	11.0	1	5.0
195A	7.983	284.804	0	1	34.0	1	13.0	1	30.0
8A_C	7.928	287.496	0	1	47.0	1	6.0	1	830.0
48BA	7.068	289.270	0	1	45.0	1	17.0	1	125.0
Pohn	6.984	158.202	0	1	3.0	1	1.0	1	9.0
282_	6.961	284.574	0	1	20.0	1	7.0	1	25.0

continued on next page

<i>continued from previous page</i>									
Code	latitude	longitude	elev.	N_x	σ_x [nT]	N_y	σ_y [nT]	N_z	σ_z [nT]
4C_G	6.289	284.562	0	1	8.0	1	9.0	1	167.0
287_	5.738	284.397	0	1	3.0	1	50.0	1	15.0
101_	5.537	286.660	0	1	41.0	1	43.0	1	35.0
Adio	5.325	355.867	0	1	18.0	1	13.0	1	4.0
507_	5.300	287.613	0	1	23.0	1	13.0	1	77.0
258A	5.075	285.387	0	1	5.0	1	6.0	1	29.0
502_	5.026	286.549	0	1	19.0	1	13.0	1	24.0
274_	4.604	284.364	0	1	1.0	1	4.0	1	26.0
100_	4.422	284.806	0	1	10.0	1	1.0	1	76.0
506_	4.200	285.566	0	1	12.0	1	12.0	1	14.0
392_	3.881	292.082	0	1	1.0	1	13.0	1	12.0
_16A	2.978	284.691	0	1	1.0	1	19.0	1	91.0
82_E	2.140	283.038	0	1	19.0	1	2.0	0	1.0
111S	1.881	283.750	0	1	7.0	1	1.0	1	68.0
28B_	1.800	281.213	0	1	14.0	1	174.0	1	25.0
493_	1.592	284.426	0	1	5.0	1	9.0	1	62.0
494A	1.340	288.049	0	1	52.0	1	4.0	1	117.0
122A	0.518	283.469	0	1	9.0	1	4.0	1	19.0
58B_	-0.194	285.228	0	1	35.0	1	114.0	1	58.0
NAI	-1.333	36.817	1670	1	3.0	1	27.0	1	18.0
431L	-1.346	290.404	0	1	15.0	1	2.0	1	51.0
Momo	-2.067	147.407	0	1	4.0	1	22.0	1	40.0
SAO_	-2.505	315.775	0	1	32.0	1	6.0	1	9.0
Kavi	-2.580	150.805	0	1	2.0	1	2.0	1	11.0
113B	-2.886	290.254	0	1	24.0	1	8.0	1	2.0
59AL	-4.192	290.075	0	1	30.0	1	14.0	1	1.0
60CL	-4.217	290.048	0	1	27.0	1	3.0	1	5.0
NATA	-5.768	324.807	0	1	6.0	1	6.0	1	1.0
NATA	-5.770	324.810	0	1	19.0	1	1.0	1	10.0
Arop	-6.305	155.725	0	1	6.0	1	16.0	1	87.0
_Rec	-8.080	325.100	0	1	15.0	1	1.0	1	4.0
PORT	-8.700	296.098	0	1	1.0	1	4.0	1	3.0
Honi	-9.424	160.047	3	1	14.0	1	9.0	1	2.0
Cook	-15.446	145.188	0	1	1.0	1	3.0	1	1.0
CHIR	-15.997	28.897	0	1	1.0	1	6.0	1	1.0
MUSE	-16.250	31.250	384	1	5.0	1	4.0	1	3.0
KOTW	-17.017	32.633	379	1	1.0	1	1.0	1	1.0
RUAC	-17.417	14.375	0	1	2.0	1	6.0	1	2.0
BING	-17.643	27.322	36	1	1.0	1	5.0	1	1.0

continued on next page

<i>continued from previous page</i>									
Code	latitude	longitude	elev.	N_x	σ_x [nT]	N_y	σ_y [nT]	N_z	σ_z [nT]
HARA	-17.833	31.033	0	1	3.0	1	4.0	1	1.0
GOKW	-18.250	29.008	0	1	7.0	1	2.0	1	26.0
MUTA	-18.950	32.633	0	1	3.0	1	1.0	1	3.0
OKAU	-19.150	15.908	400	1	1.0	1	5.0	1	1.0
TSUM	-19.600	20.517	38	1	2.0	1	1.0	1	5.0
MASV	-20.043	30.812	0	1	1.0	1	4.0	1	1.0
BULA	-20.140	28.517	0	1	2.0	1	3.0	1	1.0
Moun	-20.667	139.490	0	1	1.0	1	4.0	1	3.0
KALK	-20.902	16.180	0	1	3.0	1	6.0	1	3.0
CHIS	-20.983	32.167	0	1	1.0	1	2.0	1	1.0
WEST	-21.067	29.383	93	1	1.0	1	3.0	1	1.0
UGAB	-21.117	13.583	0	1	3.0	1	3.0	1	1.0
FRAN	-21.167	27.500	1	1	4.0	1	1.0	1	1.0
GHAN	-21.693	21.658	0	1	2.0	1	1.0	1	5.0
MESS	-22.370	30.047	135	1	1.0	1	5.0	1	2.0
GOBA	-22.455	18.987	0	1	2.0	1	1.0	1	3.0
WIND	-22.567	17.102	0	1	1.0	1	1.0	1	4.0
SWAK	-22.670	14.567	16	1	1.0	1	4.0	1	3.0
TOMB	-23.070	28.000	0	1	2.0	1	1.0	1	1.0
KHUT	-23.325	24.495	0	1	4.0	1	1.0	1	2.0
TSHA	-24.020	21.872	60	1	15.0	1	42.0	1	1.0
MICA	-24.163	30.837	0	1	1.0	1	1.0	1	1.0
POTG	-24.183	29.000	0	1	1.0	1	1.0	1	1.0
MARI	-24.605	17.972	105	1	1.0	1	1.0	1	2.0
UNIO	-24.713	19.890	0	1	1.0	1	3.0	1	3.0
SOSS	-24.733	15.350	0	1	2.0	1	3.0	1	1.0
BARB	-25.778	31.033	45	1	2.0	1	1.0	1	1.0
MMAB	-25.850	25.650	6	1	2.0	1	1.0	1	8.0
SEVE	-26.592	22.858	0	1	1.0	1	3.0	1	7.0
Quil	-26.615	144.257	0	1	1.0	1	7.0	1	1.0
KEET	-26.617	18.162	0	1	1.0	1	3.0	1	2.0
RIET	-26.733	20.040	0	1	1.0	1	1.0	1	1.0
PARY	-26.930	27.408	0	1	1.0	1	1.0	1	9.0
_PIE	-27.017	30.817	130	1	26.0	1	3.0	1	5.0
PIET	-27.075	30.887	135	1	2.0	1	1.0	1	2.0
REIT	-27.720	28.525	0	1	1.0	1	3.0	1	7.0
DUND	-28.123	30.298	130	1	4.0	1	5.0	1	1.0
ST_L	-28.348	32.425	0	1	4.0	1	8.0	1	3.0
UPIN	-28.423	21.298	88	1	2.0	1	3.0	1	7.0

continued on next page

<i>continued from previous page</i>									
Code	latitude	longitude	elev.	N_x	σ_x [nT]	N_y	σ_y [nT]	N_z	σ_z [nT]
WARM	-28.480	18.602	0	1	1.0	1	1.0	1	9.0
ALEX	-28.568	16.525	46	1	1.0	1	1.0	1	2.0
DOUG	-29.100	23.738	0	1	1.0	1	2.0	1	8.0
LADY	-29.217	27.463	4	1	3.0	1	2.0	1	3.0
More	-29.497	149.846	0	1	1.0	1	1.0	1	2.0
UNDE	-29.785	29.490	0	1	1.0	1	1.0	1	1.0
PORT	-30.000	308.817	0	1	21.0	1	8.0	1	5.0
PORT	-30.030	308.825	0	1	22.0	1	8.0	1	1.0
BLOU	-30.047	19.472	12	1	1.0	1	1.0	1	1.0
Bour	-30.052	145.952	0	1	1.0	1	1.0	1	2.0
HOND	-30.318	17.290	150	1	1.0	1	2.0	1	5.0
PHIL	-30.387	25.252	0	1	1.0	1	1.0	1	7.0
SANT	-30.875	304.478	0	1	1.0	1	6.0	1	1.0
FONT	-30.952	23.153	27	1	1.0	1	4.0	1	7.0
WILL	-31.348	20.937	0	1	3.0	1	2.0	1	4.0
ELLI	-31.353	27.828	9	1	10.0	1	10.0	1	4.0
VANR	-31.623	18.727	0	1	1.0	1	1.0	1	5.0
CRAD	-32.162	25.633	0	1	2.0	1	3.0	1	5.0
KARE	-32.790	20.538	0	1	1.0	1	2.0	1	6.0
RIET	-32.892	23.153	0	1	1.0	1	3.0	1	6.0
GONU	-32.937	28.030	3	1	1.0	1	1.0	1	5.0
LANG	-33.063	18.080	0	1	1.0	1	1.0	1	3.0
Espe	-33.686	121.821	0	1	1.0	1	1.0	1	6.0
HUMA	-34.040	24.782	0	1	4.0	1	2.0	1	6.0
BUFF	-34.313	18.452	0	1	1.0	1	1.0	1	4.0
Augu	-34.331	115.156	2	1	1.0	1	1.0	1	7.0
AGUL	-34.832	20.005	0	1	1.0	1	1.0	1	2.0
Kait	-35.086	173.248	12	1	1.0	1	1.0	1	3.0
When	-36.787	174.628	46	1	1.0	1	3.0	1	1.0
TE	-37.739	177.675	6	1	1.0	1	1.0	1	1.0
Whak	-37.922	176.909	9	1	2.0	1	4.0	1	1.0
_TOL	-38.369	178.313	15	1	11.0	1	1.0	1	10.0
Gisb	-38.661	177.971	5	1	51.0	1	18.0	1	28.0
ST_P	-38.714	77.536	41	1	1.0	1	1.0	1	8.0
_HUI	-39.248	174.472	48	1	3.0	1	5.0	1	1.0
_KUR	-39.394	176.329	1	1	5.0	1	2.0	1	12.0
Flin	-40.091	147.991	5	1	1.0	1	1.0	1	1.0
West	-41.742	171.574	34	1	1.0	1	3.0	1	6.0
Hoki	-42.720	170.990	1	1	1.0	1	1.0	1	9.0

continued on next page

<i>continued from previous page</i>									
Code	latitude	longitude	elev.	N_x	σ_x [nT]	N_y	σ_y [nT]	N_z	σ_z [nT]
Hoba	-42.817	147.500	1	1	1.0	1	2.0	1	2.0
Chat	-43.810	183.538	5	1	1.0	1	4.0	1	2.0
Te_R	-43.816	183.420	1	1	1.0	1	5.0	1	2.0
_BOG	-44.573	170.139	29	1	12.0	1	8.0	1	1.0
_MOE	-45.348	170.812	21	1	1.0	1	4.0	1	4.0
Amer	-46.388	51.799	1	1	14.0	1	3.0	1	7.0
MRN	-46.867	37.850	0	1	8.0	1	1.0	1	33.0
_TER	-50.539	166.216	1	1	3.0	1	1.0	1	1.0
_CAM	-52.548	169.154	1	1	9.0	1	1.0	1	3.0
PORT	-66.817	141.400	0	1	1.0	0	1.0	0	1.0

Appendix B

List of base line jumps

Table B.1: List of base line jumps, site changes and new instrumentation at permanent observatories during 1980 – 2000. The observatories are ordered by descending latitude, from north to south.

Obs.	Time	X [nT]	Y [nT]	Z [nT]	Note
ALE	1996.0	13	10	82	-
MBC	1996.0	-8	0	44	position reassessed
RES	1996.0	0	0	-7	new absolute pavilion
GDH2	1990.0	4	-4	15	new absolute pier
CBB	1996.0	0	-12	30	position reassessed
CMO2	1988.0	4	2	-33	Adjustment to calibration data from 01/01/1988
YKC2	1996.0	449	-165	311	-
DOB2	1999.0	11	15	9	position reassessed
NAQ	1989.0	2	10	30	new absolute pier
NAQ	1994.0	-1	0	-2	-
LER	1990.0	-5	1	8	site difference
LER	1996.0	0	0	-8	site difference
FCC	1996.0	0	0	10	position reassessed
SIT2	1988.0	2	1	5	Adjustment to calibration data
ESK	1990.0	-11	1	-22	Site difference 1 Jan 1990
ESK	1994.0	8	-1	23	Adjustment to account for incorrect estimate of site difference 1989/1990
PBQ	1996.0	-16	-6	-91	-
MEA	1996.0	0	0	17	-
NGK	1996.0	-4	0	0	-

continued on next page

<i>continued from previous page</i>					
Obs.	Time	X [nT]	Y [nT]	Z [nT]	Note
VAL	1997.0	21	-5	32	Jump caused by move to new absolute hut
HAD	1980.0	0	0	6	Change of absolute pier
HAD	1990.0	6	-1	-23	Site difference 1 Jan 1990
MAB	1991.0	0	0	0	3 pillars to 1 & change in gyro-magnetic ratio-jump values unknown
GLN	1996.0	-11	0	-43	-
BDV	1998.0	-4	-3	2	-
VIC	1996.0	11	10	-35	-
NEW	1988.0	7	2	0	Adjustment to calibration data from 1988 Jan 1 onwards
OTT	1996.0	2	0	8	-
TFS	1988.0	27	2	-32	-
MIZ	1990.0	-12	2	35	Site change of Absolute Hut for H & Z on Jan. 1 1990
FRD	1988.0	1	6	2	Adjustment to calibration data from 1988 Jan 1 onwards
FRD	1997.0	1	0	0	Change of absolute pier
HTY	1981.0	-118	-365	-78	Site change
CNH2	1980.0	0	0	0	jump values unknown, assumed to be zero
TUC	1988.0	8	2	-65	Observatory moved
JAI	1980.0	53	-1	90	Baseline corrections applied to H & Z
UJJ	1980.0	83	-1	25	Baseline corrections applied to H & Z
HON3	1988.0	-1	4	0	Adjustment to calibration data from 1988 Jan 1 onwards
ABG	1991.0	-128	0	-113	Site differences caused by change of location of H & Z observation
SJG2	1988.0	1	1	7	Adjustment to calibration from 1/1/88, sign changed
HYB	1983.0	0	0	-22	-
GUA	1988.0	26	1	7	Adjustment to calibration data from 1988 Jan 1 onwards
LUA3	1981.0	58	-9	93	Corrections applied to H & Z

continued on next page

<i>continued from previous page</i>					
Obs.	Time	X [nT]	Y [nT]	Z [nT]	Note
PPT	1996.0	61	253	-173	Obs moved some 100s of metres & new equipment installed during 1995
TSU	2000.0	-1	-10	1	New pillar references
HBK	2000.0	-34	11	-18	New pillar references
GNA	1994.0	7	-11	27	-
HER	2000.0	4	2	-16	New pillar references
PAF	1988.0	0	0	0	Observatory moved to new site
MIR	1989.0	0	0	0	-
DRV	1982.0	-8	-6	-11	DI-Flux replace QHM and absolute measurement moved
DRV	1995.0	0	0	-13	New absolute pier
NVL	1983.0	125	179	-40	Observatory moved to new site, March 1983
SBA	1988.0	-50	0	0	Instrumentation change 50 nT discontinuity in X

Appendix C

Flow Coefficients of the drifting flow

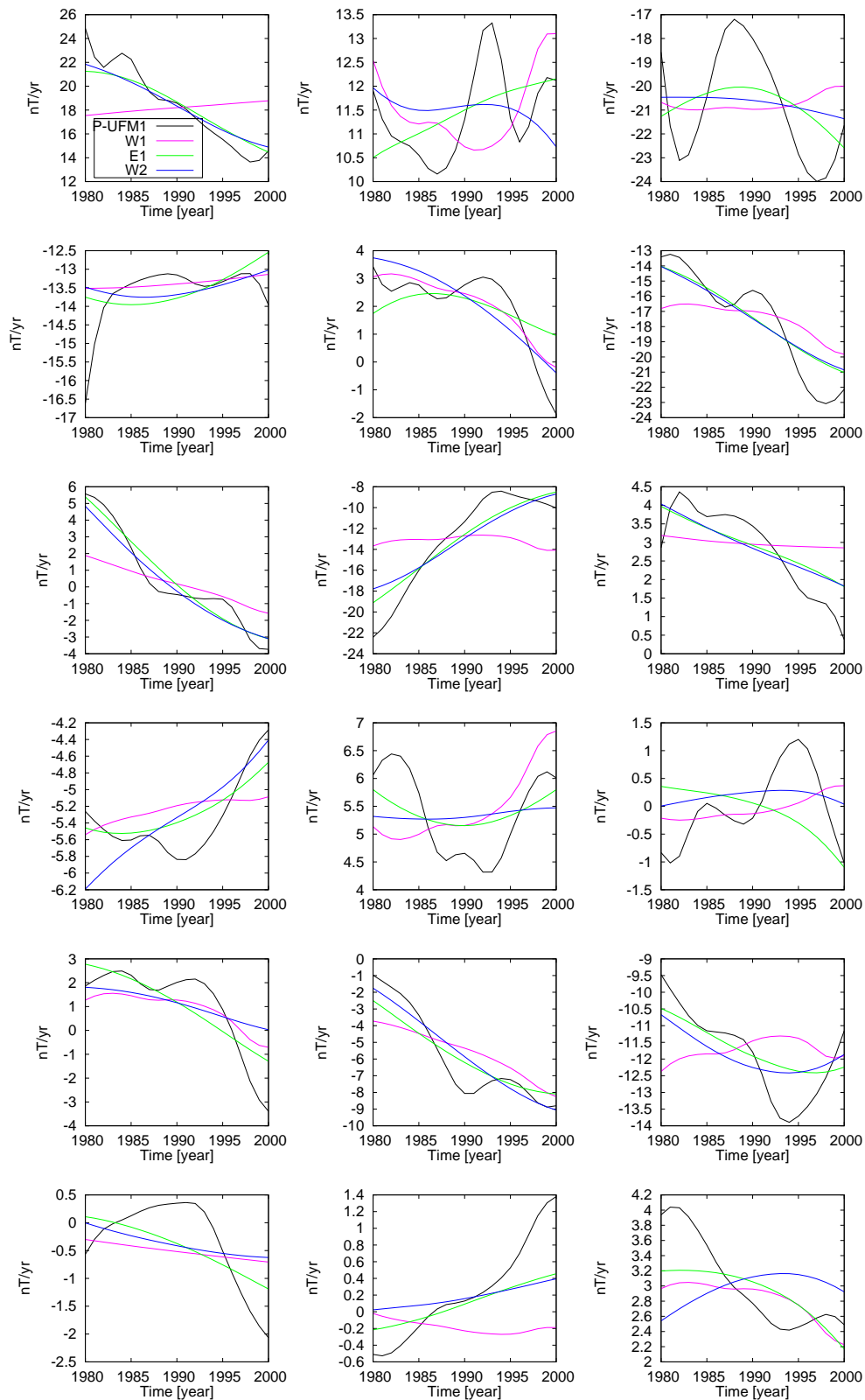


Figure C.1: Comparison of coefficients of the different drifting solutions. The black curves are the time-dependent model of the secular variation P-UFM1, pink line is the prediction of the westward solution W1, the green line the eastward solution E1 and the blue line the westward solution W2.

Lebenslauf

Name Ingo Wardinski
geboren am 4. Juni 1969 Potsdam

Schulausbildung

1976 – 1986 Polytechnische Oberschule *N. K. Krupskaja* Potsdam
1988 – 1991 Volkshochschule *A. Einstein* Potsdam

Universität

1991 – 1994 Studium der Physik Universität Greifswald
1993 Physik Vordiplom (B.Sc.)
1994 – 1999 Studium der Physik Universität Potsdam
1999 Physik Diplom (M.Sc.)

Beruflicher Werdegang

1986 – 1988 Ausbildung als Feinmechaniker am ZIPE Potsdam
1988 – 1989 Ausbildung als Gesteinspräparator am ZIPE Potsdam
1989 – 1991 Tätigkeit als Feinmechaniker und Gesteinspräparator am ZIPE
Potsdam
2000 wiss. Mitarbeiter (Planetary Science) an der Universität Potsdam
seit 02/2001 Doktorand GeoForschungsZentrum Potsdam Thema der Arbeit:
'Decadal and Subdecadal Secular Variation of the Main Geomag-
netic Field' im DFG special research program SPP 1097 'Geomag-
netic Variation'

Erklärung

Hiermit erkläre ich an Eides statt, dass die vorliegende Arbeit von mir selbständig erstellt wurde. Es wurden keine anderen als die angegebenen Quellen und Hilfsmittel benutzt und Zitate als solche kenntlich gemacht.